TECHNISCHE UNIVERSITÄT MÜNCHEN
LEHRSTUHL FÜR AERODYNAMIK UND
STRÖMUNGSMECHANIK

# Uncertainty Analysis of Shock-Bubble Interaction

Kwok Kai So

Vollständiger Abdruck der von der Fakultät für Maschinenwesen der Technischen Universität München zur Erlangung des akademischen Grades eines

Doktor-Ingenieurs

genehmigten Dissertation.

Vorsitzender: Univ.-Prof. Dr.-Ing. Oskar J. Haidn

Prüfer der Dissertation:

1. Univ.-Prof. Dr.-Ing. habil. Nikolaus A. Adams
2. Prof. Gianluca Iaccarino, Ph.D.
   Stanford University / USA

Die Dissertation wurde am 31.05.2013 bei der Technischen Universität München eingereicht und durch die Fakultät für Maschinenwesen am 20.02.2014 angenommen.

# Abstract

In this work, uncertainties in shock-bubble interaction experiments are analyzed and quantified by simulations.

As the first part of the work, a novel numerical method for two-phase flow simulations is developed. An interface-sharpening technique by means of solving an anti-diffusion equation for two-phase incompressible-flow simulations based on volume-of-fluid methods is presented. The numerical stability and volume-fraction boundedness in the anti-diffusion correction step are ensured by a specified discretization scheme and a stopping criterion. Validation computations demonstrate that sharp interfaces can be recovered reliably and a good agreement with experimental results including rising drop and bubble is observed. The interface-sharpening technique is then extended to two-phase compressible-flow simulations. The consistent update and exact conservation of the flow variables are maintained in the interface-sharpening step. Numerical results show an improved interface resolution in shock-bubble interaction simulations, where interface roll-up phenomena due to the Richtmyer-Meshkov instability and the Kelvin-Helmholtz instability are recovered reliably as compared with reference high grid-resolution numerical results based on adaptive-mesh-refinement algorithms.

As the second part of the work, a physical shock-bubble interaction experiment and its associated uncertainties are studied by simulations. Based on an experimental case of air-helium shock-bubble interaction, the amount of gas contamination inside the bubble and the deformation of the initial bubble shape are selected as the uncertainty parameters. The interface evolution and the total vorticity are considered as the quantities of interest. The stochastic collocation method is employed to propagate the input uncertainty to the output quantities of interest. The uncertainty analysis shows that the jet formed inside the bubble is most affected by the presence of the uncertainties, and the baroclinic vorticity generation during the vorticity deposition phase is found to be largely dependent on the bubble gas content as well as the bubble shape.

# Acknowledgements

I would like to express my sincere gratitude to my supervisors Prof. Dr.-Ing. Nikolaus A. Adams, Prof. Gianluca Iaccarino, PD Dr.-Ing. habil. Christian Stemmer and Dr.-Ing. Xiangyu Hu for their guidance and advice. I am also grateful to have the opportunity to undertake the research work at the Institute of Aerodynamics and Fluid Mechanics, TUM (Technische Universität München), as well as the Center of Turbulence Research, Stanford University during the summer 2010. The support by the TUM IGSSE (International Graduate School of Science and Engineering) for this work within the Project 3.01 is gratefully acknowledged.

I also wish to thank my family for her support.

# Contents

# List of Figures

# List of Tables

# Chapter 1

# Introduction

## 1.1 Background and objectives

The impact of a shock wave on two-phase compressible flows is an important topic in science and engineering. In particular, the interaction of a shock wave with a density inhomogeneity is a fundamental subject in compressible turbulence [80]. To better understand the instability phenomena that are present in the evolution of such flows, the shock-bubble interaction [72] is a basic configuration for studying the shock-accelerated inhomogeneous flows [122]. The investigation of the shock-bubble interaction leads to the understanding of the Richtmyer-Meshkov Instability (RMI) [13], the Kelvin-Helmholtz Instability and the mixing mechanisms in shock-accelerated flows [105]. Flows of this type are present in many engineering applications and have a wide application in various fields including supersonic mixing and combustion systems [121], supernova explosion in astrophysics, shock-flame-front interaction, and extra-corporeal shock-wave lithotripsy [72].

Analytical models, shock-tube experiments, and computational fluid dynamics (CFD) simulations are the major methods for studying shock-bubble interactions. While analytical models and experiments are the conventional means for studying the physical phenomena, in the wake of the advancement of computer technology and numerical methods, simulations have proven their usefulness in the investigation of fluid mechanics problems. Configurations that cannot be analytically studied, and quantities, such as vorticity, which cannot be easily measured experimentally, are assessable by simulations, where in particular detailed numerical simulations help to elucidate the essential phenomena and interaction mechanisms [67, 80, 121, 82, 59].

As the simulation of shock-bubble interactions is being increasingly relied upon, a full analysis and prediction of the shock-bubble interaction is however not possible without a reliable numerical and physical modeling. While governing flow equations

are well defined for describing the fluid dynamics, the prediction accuracy of numerical simulations of shock-interface-interactions strongly depends on the numerical methods which are employed to solve the flow governing equations, and on the physical modeling which requires the precise definition of the physical problem. The accuracy of the two-phase-flow numerical method on the one hand, and the uncertainties implied by the input data on the other hand, must be addressed for a correct prediction of the shock-bubble-interaction phenomena. This refers to the two fundamental aspects of CFD - the verification and the validation of simulations. First, numerical methods for solving the flow governing equations have to be verified to ensure the consistency of the numerical solution and the exact solution. Second, even a simulation code that is verified for a certain case, it must be validated against the physical observation, essentially the experiment data, to establish the validity of the results generated. The two aspects have to be examined in order to establish the accountability of the simulation results.

The foresaid situation poses a challenge in the field of shock-bubble interaction simulations and lays down the scope of the present work:

- the study of numerical methods for shock-bubble interaction simulations, and where possible, for two-phase-flow simulations in a broader sense;
- the study of a shock-bubble interaction experimental reference, and the quantification and analysis of the associated experimental uncertainties by simulations.

In the following sections, the previous and related works relevant to the topic are described. The accomplishments achieved in this work are then presented, and the thesis outline is given at the end of this chapter.

## 1.2 Previous and related works

### Shock-bubble interactions

Shock-bubble interactions are concerned with the fluid dynamic phenomena of a shock wave propagating through a medium of non-uniform thermodynamic properties, where a geometrically well-defined density inhomogeneity such as a cylinder or a sphere is the simplest configuration that can be studied in detail [72]. Shock-bubble interactions have been studied analytically, experimentally and numerically in the last decades. Analytically, different analytical estimations of the circulation generated in shock-bubble interactions are proposed in [67, 80, 121, 82, 59]. The analytical studies are based on certain flow regimes of planar density-stratified interfaces or curved

density-stratified interfaces where the basic estimations are further extended to the scenarios of shock-bubble interactions. Experimentally, Haas and Sturtevant recorded a clear set of experimental images and discussed quantitatively the bubble evolution [26]. To refrain from the membrane for bubble formation, Jacobs [35] and Tomkins et al. [105] performed membraneless shock-bubble experiments. Simulations using the interface-tracking and the interface-capturing method have been performed to investigate the experimental findings. Quirk and Karni [69] conducted among others a detailed numerical study of shock-bubble interaction based on the experiments of Haas & Sturtevant [26].

## Numerical methods for two-phase flow and shock-bubble interaction simulations

Shock-bubble interactions can be categorized as two-phase compressible flows. The two phases are treated as immiscible and a distinct interface exists between the two phases. For simulating this kind of two-phase flows, various approaches have been proposed which can be categorized into two main classes, namely interface-tracking methods and interface-capturing methods. With the aim to develop a numerical method suitable for two-phase-flow, the two classes of interface methods for both incompressible and compressible two-phase flows are studied and described below.

With interface-tracking methods, the location of the interface is explicitly represented, e.g. front tracking methods [111, 108, 104] and marker methods [107, 84]. Marker methods can efficiently locate the interface position by interface markers. However, they encounter difficulties for large interface deformations and topology changes, and require a special treatment of the interface marker distribution when the interface is stretched or compressed. On the other hand, interface-capturing methods do not explicitly track but capture the location of the interface implicitly. Examples of interface-capturing methods include the level-set method [22, 66, 85] and the volume-of-fluid (VOF) method [30, 25]. With the level-set method, the interface is defined as the zero contour of a signed-distance function - the level-set function. The interface is sharp by definition, and the interface sharpness is maintained by recovering the signed distance property of the level-set function through a reinitialization. From the level-set function the curvature of the interface and the surface tension can be calculated with high accuracy. However, a main drawback of the level-set method is lack of discrete conservation. With VOF methods [84, 75], two different phases are defined by the volume fraction of one phase within the other. The interface is represented by the transition region where the volume fraction ramps up from 0 to 1. The main

advantage of VOF methods is the exact conservation of mass. One main drawback of VOF methods is the smearing of the interface by the numerical diffusion, which is due to the use of total-variation-diminishing (TVD) schemes [27] to preserve the volume-fraction boundedness (for the step-profile of volume fraction at the interface). Furthermore, the interface cannot be located precisely, which leads to inaccuracies in calculating the interface curvature and thus the surface tension.

For VOF methods, a sharp-interface representation can be obtained from the volume fraction by two approaches in general. With the first approach the interface is reconstructed before each advection step, and subsequently the flow is updated by propagating the reconstructed interface. Different interface-reconstruction schemes have been developed, such as simple line interface calculation (SLIC) [60], SOLA-VOF [30], and piecewise-linear interface construction (PLIC) as described by [84, 75] and references therein. Drawbacks of these VOF volume-tracking methods are that the curvature of the reconstructed interface is not smooth, which leads to inaccuracies in the interface propagation step, and that the interface propagation can become unstable for very complex interfaces. Non-physical flows, commonly denoted as "flotsam" and "jetsam", can be created due to the errors induced by the particular volume-tracking algorithm [75]. With the second approach, the interface position is captured by a diffused-interface representation and the volume fraction is advected with a special treatment to reduce the numerical diffusion. Examples of such VOF volume-capturing methods include a blending of a compressive scheme with a higher order scheme attempting to satisfy a convection-boundedness criterion for the advection step [110], the introduction of an artificial-compression term in the volume-fraction transport equation [78], the use of a limited downwind anti-diffusive flux correction [117] and the use of artificial compression as an intermediate step for solving the volume-fraction transport equation [62]. It should be noted that the compressive discretization scheme requires special considerations to be applicable to unstructured meshes [110]. A recent overview of interface sharpening schemes based on compressive flux formulations built into the volume-fraction transport is given by [14]. Other interface capturing methods, among others, include those making use of a phase-field function [99] or a hyperbolic tangent function [114] to represent the interface profile and to compute the numerical flux for the fluid fraction function, as well as those employing a semi-Lagrangian conservative scheme [113] or a multi-integrated moment method [115].

In particular for shock-bubble interaction simulations, different numerical methods were developed for different interface representation methods: among others the front-tracking/ghost-fluid method [104] for front-tracking representations; discontinu-

ous Galerkin methods [118] or weighted essentially non-oscillatory (WENO) schemes [22, 39, 33] for level-set representations; volume tracking by means of an interface reconstruction [90], an interface-compression method [88], and the anti-diffusive scheme [44] for VOF representations. Methods also worth noting for two-phase compressible flow simulations include the localized artificial diffusivity method for mass-fraction representations [86, 43], the stratified flow model and AUSM$^+$-up scheme [16], the $\gamma$-model [1, 38, 58], and the arbitrary Lagrangian-Eulerian scheme which involves a grid evolution [53]. The VOF volume-capturing method possesses the advantage of exact conservation properties, but suffers from numerical diffusion which causes the two-fluid interface to smear. Specific numerical schemes to suppress or counteract the numerical diffusion, and to maintain the interface sharpness in the course of simulations are thus desirable and essential for VOF methods. Previous works on maintaining a sharp interface without an interface reconstruction include the interface compression technique by [88] which originates from the interface compression technique for two-phase incompressible flows by [62], and the anti-diffusive numerical scheme based on a limited downwind strategy where stability and consistency criteria are proposed to make use of the downwind contribution [44].

## Studies of the uncertainties in shock-bubble interaction simulations

The experimental investigations of shock-bubble interactions are inevitably subject to errors and uncertainties, due to limited measurement technique and experimental reproducibility, etc. The initial conditions of shock-bubble interaction experiments, such as the real bubble shape and the test gas property (its purity and homogeneity) are the main sources of uncertainty. The identification of the exact experimental conditions and the treatment of the associated uncertainties, in simulations, are thus of paramount importance. The investigation of shock-bubble interaction experiments with uncertain initial conditions by simulations have been previously conducted by some researchers, each according to their own methodology [125, 119].

In the work of Zhang et al. [125], the authors conducted a validation process by adjusting and optimizing the initial condition through iterations to produce optimal agreement with the experiment. First, they assume different initial profiles of bubble gas distribution, and defined the uncertain parameters associated with the gas distribution profiles. Second, they proceed to run the corresponding simulations under different initial conditions, and select an initial profile and associated uncertain parameters that fit best to experimental data in terms of the optimal agreement

in early-intermediate-time large- and intermediate-scale with experimental images. Then, based on this chosen initial profile they carry on to describe and discuss the late-time phenomenon involving small-scale structures by their simulations. By such way, they obtain the maximum agreement of the early-intermediate-time large- and intermediate-scale structures between their simulation and the experimental results, and they claim an excellent agreement between experiments and their numerical simulations for many large-, intermediate-, and some small- scale flow features in late-intermediate time provided by their dynamic-initial-condition-validation-process.

Alternatively, Weirs et al. try to obtain a more realistic initial condition of the gas distribution for simulations to account for the lateral diffusion between the test gases and the gravitational effect on the formation of the gas cylinder occurring in experiments [119]. They first perform a radial fix to the experimental image of initial gas distribution taken at one cross-section of the gas cylinder for formulating a representative radial-gas-distribution function. Second, they perform an axisymmetric simulation based on the function to generate a steady flow which aims to represent the real initial condition of the gas cylinder. Then, they recompare the experiment image and the results from the axisymmetric simulations, and select the most representative initial condition for simulations. As the authors concluded, the significance of their work laid on the fact that their initial flowfield in simulation is based on experimental initial flowfield itself, rather than a choice from different initial conditions which is to match the early-intermediate-time experimental results as proposed by Zhang et al. [125]. Similarly in another work on RMI by Balakumar et al. [3], the variation of the initial conditions of the gas curtain is recorded experimentally and a synthetic initial condition for numerical simulations is created based on the best-fit to the experimental data.

On the other hand, certain researchers performed simulations to collect data on the effect of different initial conditions with the aim of characterizing shock-bubble interactions. Yang et al. studied numerically the effect of different initial conditions on the stretching rate in an application of shock-induced mixing to supersonic combustion [120]. Essentially they performed a sensitivity analysis and studied a wide range of parameters, including sinusoidal perturbation to bubble surface, elliptical bubble shape, etc. Niederhaus et al. performed a computational parameter study to investigate the morphology and integral properties of shock-bubble interaction under a wide range of scenarios, including gas pairs of different Atwood number and different shock strengths [59].

### Uncertainty quantification and analysis for CFD simulations

Assessing and quantifying uncertainties is a fundamental subject in CFD [77] and the uncertainty quantification has received an intense interest in recent years for the code validation exercise in simulation science [42]. Examples include the analysis of the uncertain initial condition in steady-state flows in a dual throat nozzle, by generalized polynomial chaos method, where the statistics of shock location is computed [17]. As opposed to the classical local sensitivity analysis which is suitable for small uncertainty [57], the uncertainty quantification is a rigorous method to account for experimental uncertainties and varying initial conditions. The effect of the uncertainty in the initial condition can be quantified in a way that the moments (mean, variance, etc.) and the evolution of the PDF can be studied in detail over time. This process accounts for the non-linear evolution of the uncertainty through the initial problem and provides quantitative estimates of the output variability given the input uncertainty, and thus is more objective than a classical parametric study.

The uncertainty quantification exercise can be categorized into 3 stages: i) data assimilation, ii) uncertainty propagation, and iii) output quantification. While the focus of the current work is on the uncertainty propagation, the uncertainty in the problem definition can be propagated and the statistic of the quantities of interest can be calculated by assuming a probability density function (PDF) of the uncertainty parameter [15]. The variance of the uncertainty variables is expressed by a polynomial chaos expansion (PCE), where the propagation of uncertainties can be evaluated by intrusive or non-intrusive methods [57]. Intrusive methods include the stochastic Galerkin methods which reformulates the governing equations to account for the polynomial chaos (PC) mode strength - the method is also termed the non-sampling method. On the other hand, non-intrusive methods are to perform sampling based on the original deterministic model to obtain the numerical evaluation of the PC modes. Monte Carlo (MC) method is a basic sampling method which is straight-forward but the convergence rate is low. High-order collocation method as proposed in [116] offers a sampling method of higher convergence rate.

## 1.3 Accomplishments

In accordance with the objectives of this work, the following accomplishments are achieved:

1. An interface sharpening technique applicable for two-phase flow simulations based on VOF methods is proposed. In this regard, for the first time, an anti-

diffusion equation is employed as an interface-sharpening technique to two-phase incompressible flow simulations. The corresponding limiter and stopping criterion essential for solving the anti-diffusion equation are developed. Numerical results show an improved accuracy of the two-phase interface. The work is published in [91, 93].

2. The anti-diffusion interface-sharpening technique is extended to two-phase compressible flow simulations. The consistent update and exact conservation of the flow variables are maintained. The complexity in shock-bubble interactions including the interface instabilities are reliably simulated. The work is published in [95, 96, 98]

3. For the first time, the stochastic collocation approach is employed for analyzing uncertainties in shock-bubble interaction experiments by simulations. The influence of the uncertain initial conditions on the output quantities of interest is quantified and studied. The work is published in [92, 94, 97].

## 1.4 Thesis outline

The thesis is organized following the accomplishments achieved in this work:

In chapter 2, the governing flow equations for two-phase incompressible flow simulation are introduced. The concept of solving an anti-diffusion equation for sharpening the interface is presented, where the essential techniques are illustrated first in an 1-dimensional formulation, followed by a generalization to 3 dimensions. Extensive numerical cases including pure advection cases, 2-dimensional and 3-dimensional flow problems, as well as simulations of experimental cases of rising bubble and drop are presented and discussed.

In chapter 3, the governing flow equations for two-phase compressible flow simulation are introduced. The essential extension of the anti-diffusion interface-sharpening technique to the compressible formulation is presented. Numerical cases including shock-tube problems, shock-bubble interactions and a shock-contact problem are discussed. In particular, the strength of the interface-sharpening technique for simulating shock-bubble interactions are demonstrated.

In chapter 4, a widely studied experimental case of shock-bubble interaction is presented, and corresponding uncertainty parameters and quantities of interest are defined. An overview of the numerical methods for flow simulations and uncertainty quantification is presented. The effect of the uncertain initial conditions on the time evolution of the statistics and the PDF of the output quantities of interest is discussed.

In chapter 5, an overall conclusion of the entire work is presented, with an outlook of potential extensions of the present work.

# Chapter 2

# Interface-sharpening technique for two-phase incompressible flow simulation

## 2.1 Introduction

In this chapter, an interface-sharpening technique is proposed for improving the interface resolution in two-phase incompressible flow simulations based on VOF methods. A regularized anti-diffusion correction technique which can be used in a straightforward fashion with any underlying VOF discretization scheme on structured or unstructured meshes is presented. The interface sharpness lost during the VOF advection step is restored by solving an anti-diffusion equation explicitly in pseudo-time. No interface reconstruction is required to track the interface position. The interface-sharpening technique is modular and can be applied to general underlying VOF discretizations. A stopping criterion for defining the desired interface thickness while maintaining stability of the overall scheme is proposed for the post-processing interface-sharpening mechanism. In other approaches such as the interface compression technique in [62, 63], a parameter is introduced relating the desired interface thickness to the grid. Here, the stopping criterion is based on a discrete measure of the interface sharpness, and the advantage of this criterion is that it does not explicitly contain the grid-size as parameter, which would be cumbersome for unstructured meshes.

This chapter is organized as follows: First, the governing equations for two-phase incompressible flow simulation and an overview of the solution procedure are presented. The main focus of the chapter, which is the formulation of the anti-diffusion

equation and the solution algorithm, is then illustrated in detail. Numerical cases and results are presented and discussed. Finally, the main points of the interface-sharpening technique are summarized in concluding remarks.

## 2.2 Governing flow equations

The governing equations for unsteady, incompressible, viscous, immiscible two-phase flow are given by the continuity equation

$$\nabla \cdot \mathbf{u} = 0 \ , \tag{2.1}$$

and the Navier-Stokes equations

$$\frac{\partial \rho \mathbf{u}}{\partial t} + \nabla \cdot \rho \mathbf{u}\mathbf{u} = -\nabla p + \nabla \cdot \boldsymbol{\tau} + \rho \mathbf{g} + \mathbf{f}_\sigma \quad , \tag{2.2}$$

where $\mathbf{u}$ is the velocity, $\rho$ is the density, $t$ is time, $p$ is the pressure, $\boldsymbol{\tau}$ is the stress tensor, $\mathbf{g}$ is the gravitational acceleration, and $\mathbf{f}_\sigma$ is the force due to surface tension. Two different fluids are represented by the volume fraction $\alpha$ with $0 \leq \alpha \leq 1$, where $\alpha = 0$ refers to the first fluid, $\alpha = 1$ refers to the second fluid. $0 < \alpha < 1$ is the transitional region, i.e. the smeared discrete representation of the interface between the two fluids. The volume fraction is advected by the flow, resulting in the volume-fraction-transport equation

$$\frac{\partial \alpha}{\partial t} + \nabla \cdot \alpha \mathbf{u} = 0 \quad . \tag{2.3}$$

Density, $\rho$, and viscosity, $\mu$, can be recovered from $\alpha$ by

$$\rho = \alpha \rho_1 + (1 - \alpha)\rho_2 \tag{2.4}$$

and

$$\mu = \alpha \mu_1 + (1 - \alpha)\mu_2 \quad , \tag{2.5}$$

where the subscripts 1 and 2 denote the respective fluids of the two-phase flow. The Newtonian stress tensor is given by

$$\boldsymbol{\tau} = \mu(\nabla \mathbf{u} + \nabla \mathbf{u}^T) \quad . \tag{2.6}$$

The surface curvature of the interface, $\kappa$, is given by

$$\kappa = \nabla \cdot \left( \frac{\nabla \alpha}{|\nabla \alpha|} \right) \quad , \tag{2.7}$$

resulting in the force due to surface tension

$$\mathbf{f}_\sigma = -\sigma\kappa\nabla\alpha \quad , \tag{2.8}$$

using the Continuum-Surface-Force (CSF) formulation of Brackbill et al. [10]. $\sigma$ is the surface tension.

As the objective is to develop a simple and modular correction technique for recovering a (sufficiently) sharp interface that also works efficiently with discretization schemes typical for industrial practice, a rather straight-forward low-order finite-volume unstructured-mesh scheme is used for the above flow equations. A convenient environment is given by the open source CFD package OpenFOAM [64], providing an underlying framework of the VOF volume-capturing method [78]. It should be noted that the correction procedure can be incorporated in a straight-forward fashion into any underlying time-marching VOF discretization scheme. The algorithm for solving the discretized VOF equations can be summarized as follows: First, the advection equation (2.3) is evaluated for one time step based on the limiter by Jasak et al. [37, 64]. Second, density and viscosity fields are updated from the new volume-fraction field. Third, the momentum and continuity equations are solved by the PISO algorithm [34].

## 2.3 Anti-diffusion correction

The advection step of the volume-fraction-transport equation introduces additional interface smearing by numerical diffusion. To counter-act the numerical diffusion, the main idea is to provide a correction algorithm which can be applied as post-processing to the volume-fraction field, independent of the underlying VOF discretization scheme. For this purpose, the following anti-diffusion equation after each time step of the advection equation (2.3) is solved:

$$\frac{\partial\alpha}{\partial\tau} = -\nabla\cdot(D\nabla\alpha) \quad , \tag{2.9}$$

where $D > 0$ is an anti-diffusion coefficient and $\tau$ is a pseudo time.

### Formulation of the 1-dimensional anti-diffusion equation

Before formulating the anti-diffusion correction for 3-dimensional flow simulations, the essential properties of the anti-diffusion correction are illustrated for one spatial

dimension:

$$\frac{\partial \alpha}{\partial \tau} = -\frac{\partial}{\partial x}\left(D\frac{\partial \alpha}{\partial x}\right) \quad , \tag{2.10}$$

where the diffusion operator is written as sequence of two first-order derivatives on purpose. The anti-diffusion equation is ill-posed and thus an approximate numerical solution requires regularization. A regularized solution to an anti-diffusion equation was first proposed by Boris and Book [8] for a compressive correction within the flux-corrected-transport (FCT) algorithm. Other methods formulating a non-linear diffusion coefficient have been reported and applied to the field of image processing, such as the stabilized inverse diffusion equations [68] and the forward-and-backward adaptive diffusion process [23]. Alternatively, a *minmod* limiter for discrete inverse diffusion was proposed by Osher and Rudin [65]. Other regularization methods suitable for the anti-diffusion equation are monotonicity preserving constraints [4, 76], or maximum and minimum bounds on unstructured meshes [110]. An analysis of inverse-diffusion regularization based on a *minmod* function was carried out by Breuß et al. [11, 12].

**Regularized discrete approximation of the anti-diffusion equation**

Considering a 1-dimensional equidistant grid, the anti-diffusion equation can be discretized as

$$\alpha_i^{n+1} = \alpha_i^n + D\frac{\Delta \tau}{\Delta x}\left(F_{i-1/2}^n - F_{i+1/2}^n\right) \ , \tag{2.11}$$

where $F_{i+1/2}^n$ is defined by a *minmod* limiter [11, 12] as

$$F_{i+1/2}^n = \text{minmod}\left(\frac{\Delta_{i+3/2}\alpha^n}{\Delta x}, \frac{\Delta_{i+1/2}\alpha^n}{\Delta x}, \frac{\Delta_{i-1/2}\alpha^n}{\Delta x}\right) \quad , \tag{2.12}$$

using $\Delta_{i+1/2}\alpha^n = \alpha_{i+1}^n - \alpha_i^n$. The index $i$ indicates the considered cell and $n$ the time step. The *minmod* limiter is defined as

$$\text{minmod}\,(a,b,c) = \text{sgn}\,(b)\max\left(0, \min\left(\text{sgn}\,(b)\,a, |b|, \text{sgn}\,(b)\,c\right)\right) \quad . \tag{2.13}$$

The calculation of $F_{i+1/2}^n$ requires the stencil $\left\{\alpha_{i+2}^n, \ldots, \alpha_{i-1}^n\right\}$ which is not well defined in more dimensions with respect to the cell face between cell $i$ and cell $i+1$. For this reason, a compact reformulation of eq. (2.12) is introduced. First, it is observed that $F_{i+1/2}^n$ defined by eq. (2.12) is equivalent to

$$F_{i+1/2}^n = \begin{cases} (\nabla\alpha)_{i+1}^n & \text{if } \left|(\nabla\alpha)_{i+1}^n\right| \leq \left|(\nabla\alpha)_i^n\right| \\ (\nabla\alpha)_i^n & \text{if } \left|(\nabla\alpha)_i^n\right| < \left|(\nabla\alpha)_{i+1}^n\right| \end{cases} \quad , \tag{2.14}$$

where $(\nabla\alpha)_i^n$, taken at each cell center, is calculated from

$$(\nabla\alpha)_i^n = \text{minmod}\left(\frac{\alpha_{i+1}^n - \alpha_i^n}{\Delta x}, \frac{\alpha_i^n - \alpha_{i-1}^n}{\Delta x}\right) \quad . \tag{2.15}$$

The two-variable *minmod* function is defined as

$$\text{minmod}\,(a,b) = \begin{cases} a & \text{if } a\cdot b > 0 \text{ and } |a| \le |b| \\ b & \text{if } a\cdot b > 0 \text{ and } |b| \le |a| \\ 0 & \text{else} \end{cases} \quad . \tag{2.16}$$

By combining (2.15) and (2.14), it is obvious that the resulting numerical flux function, $F_{i+1/2}^n$, is equivalent to that of (2.12). Note that by (2.15) the calculation of $(\nabla\alpha)_i$ requires only a three-point stencil $\left\{\alpha_{i+1}^n, \alpha_i^n, \alpha_{i-1}^n\right\}$.

Now, the *minmod* evaluation in eq. (2.15) and (2.16) can be reformulated as

$$(\nabla\alpha)_i^n = \frac{\alpha_{i+1/2}^n - \alpha_{i-1/2}^n}{\Delta x} \quad , \tag{2.17}$$

with

$$\alpha_{i+1/2}^n = \begin{cases} \alpha_{i+1}^n & \text{if } \Delta_{i+1/2}\alpha^n \Delta_i\alpha^n > 0 \text{ and } \left|\Delta_{i+1/2}\alpha^n\right| < |\Delta_i\alpha^n| \\ \frac{\alpha_{i+1}^n + \alpha_i^n}{2} & \text{if } \Delta_{i+1/2}\alpha^n \Delta_i\alpha^n > 0 \text{ and } \left|\Delta_{i+1/2}\alpha^n\right| = |\Delta_i\alpha^n| \\ \alpha_i^n & \text{else} \end{cases} \quad , \tag{2.18a}$$

$$\alpha_{i-1/2}^n = \begin{cases} \alpha_{i-1}^n & \text{if } \Delta_{i-1/2}\alpha^n \Delta_i\alpha^n > 0 \text{ and } \left|\Delta_{i-1/2}\alpha^n\right| < |\Delta_i\alpha^n| \\ \frac{\alpha_i^n + \alpha_{i-1}^n}{2} & \text{if } \Delta_{i-1/2}\alpha^n \Delta_i\alpha^n > 0 \text{ and } \left|\Delta_{i-1/2}\alpha^n\right| = |\Delta_i\alpha^n| \\ \alpha_i^n & \text{else} \end{cases} \quad , \tag{2.18b}$$

where $\Delta_i\alpha^n = \frac{\alpha_{i+1}^n - \alpha_{i-1}^n}{2}$. For non-equidistant grids the $\Delta_{i\pm1/2}\alpha^n$ and $\Delta_i\alpha^n$ in (2.18b) need to be divided by the respective local grid spacings. A comparison of (2.15) and (2.16) with (2.17) and (2.18) shows that the resulting $(\nabla\alpha)_i^n$ are equivalent. Note that by (2.18a) the evaluation of $\alpha_{i+1/2}^n$ requires only the one-sided difference $\Delta_{i+1/2}\alpha^n$ and the central difference $\Delta_i\alpha^n$, and similarly for $\alpha_{i-1/2}^n$ in (2.18b).

### Stability and time-step constraint

The time derivative is discretized by an Euler-forward scheme in eq. (2.11). Note that the anti-diffusion correction is needed only as an interface-sharpening procedure, which is iterated in pseudo-time until a stopping criterion (see next section) is satisfied,

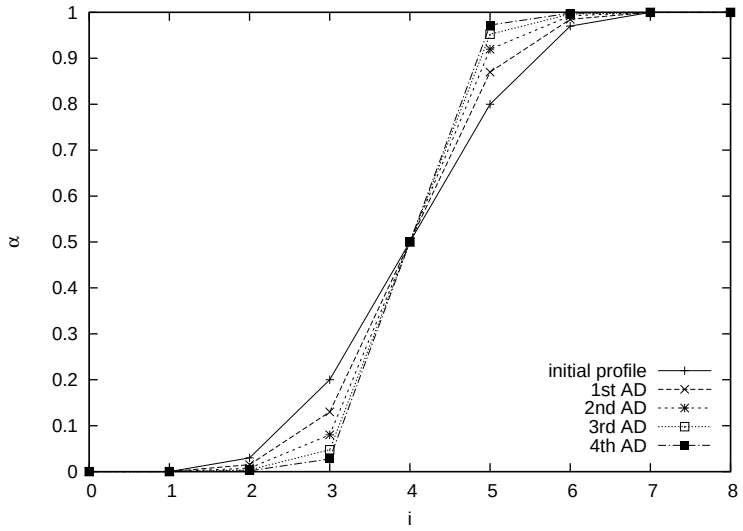


Figure 2.1: 1-dimensional profile of volume fraction $\alpha$. $i$ denotes the cell index. n-th AD denotes the profile after the n-th anti-diffusion correction.

so that a higher- order accuracy is not needed. The remaining concern is about the stability of time advancement of (2.11), where the relevant stability criterion for the discrete anti-diffusion equation [93] is given in Appendix A.

### Measurement of interface sharpness

The effect of the anti-diffusion correction is illustrated in Fig. 2.1. A smoothed Heaviside function, with a transition region across 6 cells, is taken as initial data to represent an interface smeared by numerical diffusion. The effect of several anti-diffusion time steps is then illustrated. As can be seen from the result, the anti-diffusion correction exhibits the desired properties: reduction of the thickness of the transition region, while preserving the interface position, and boundedness of the volume fraction between 0 and 1. With more iterations a three-point profile is obtained and maintained. However, a three-point interface is marginally resolved on the underlying mesh with respect to discrete operators at the interface. In particular in two or three dimensions and on unstructured meshes this marginal resolution implies direction dependent numerical resolution and may lead to nonphysical interface behavior as consequence of discrete approximations of surface normals and curvature. Therefore it is desirable to limit the interface sharpening.

For this purposes, two tolerances $TOL_1$ and $TOL_2$ are defined as

$$TOL_1 = \frac{\sum_i |\Delta_i \left( (\Delta_i \alpha)_{lim} \right)^n|}{\sum_i |\left( (\Delta_i \alpha)_{CD} \right)^n|^2} \quad , \tag{2.19a}$$

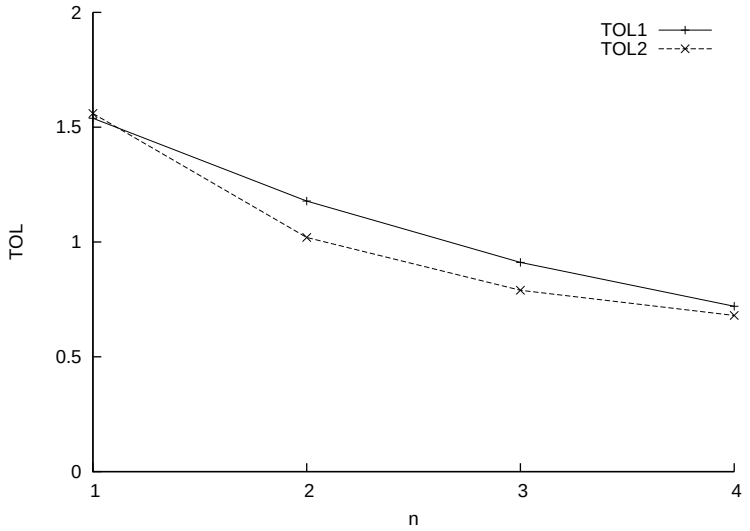


Figure 2.2: Evolution of $TOL_1$ and $TOL_2$ corresponding to the anti-diffusion correction in Fig. 2.1. $n$ denotes the number of anti-diffusion correction steps.

$$TOL_2 = \frac{\max_i \left( \left| \Delta_i \left( \left( \Delta_i \alpha \right)_{lim} \right)^n \right| \right)}{\max_i \left( \left| \left( \left( \Delta_i \alpha \right)_{CD} \right)^n \right|^2 \right)} \quad , \tag{2.19b}$$

where $\sum_i$ denotes the summation over all cells, $\max_i$ is the maximum over all cells. We denote $\left( \Delta_i \alpha \right)_{lim}$ as the gradient obtained in the regularized discrete approximation of the anti-diffusion equation. $\Delta_i \left( \left( \Delta_i \alpha \right)_{lim} \right)^n$ is the solution of the anti-diffusion equation, and $\left( \left( \Delta_i \alpha \right)_{CD} \right)^n$ is the gradient obtained from the central difference scheme. Corresponding definitions can be written in multiple dimensions and for unstructured meshes by taking the divided differences instead of the undivided differences $\Delta_i$. The evolution of $TOL_1$ and $TOL_2$ corresponding to the anti-diffusion correction in Fig. 2.1 is shown in Fig. 2.2.

## Extension to multiple dimensions, general meshes and nonlinear diffusion

To extend the interface sharpening by anti-diffusion to multiple dimensions and unstructured meshes, and to couple the anti-diffusion algorithm with the volume-fraction advection and the Navier-Stokes equations for realistic flow simulations, the diffusion coefficient is related to the numerical diffusion due to advection. A modified-differential equation analysis of the numerical diffusion induced by an upwind scheme gives that the numerical diffusion scales with the magnitude of the advection velocity, see e.g. [51]. As the anti-diffusion correction is intended to counteract the numerical diffusion, it is reasonable to set the diffusion coefficient in the anti-diffusion equation

as

$$D = |\mathbf{u}| \tag{2.20}$$

so that

$$\frac{\partial \alpha}{\partial \tau} = \nabla \cdot (-|\mathbf{u}| \nabla \alpha) \quad , \tag{2.21}$$

where $|\mathbf{u}|$ is constant with respect to $\tau$.

Eq. (2.21) is discretized by translating the discretization of (2.9) to multiple dimensions and general meshes. First, the cell average of $\nabla\alpha$ is calculated from the Gauss theorem with a limiter based on the directional derivative. The calculated cell-average $\overline{(\nabla\alpha^n)_i}$ at time step $n$ and for cell $i$ is multiplied by the diffusion coefficient to obtain $\left(-|\mathbf{u}_i| \overline{(\nabla\alpha^n)_i}\right)$. Note that with respect to $n$ the velocity $\mathbf{u}_i$ is constant. The cell-averaged divergence $\nabla \cdot (-|\mathbf{u}| \nabla\alpha^n)$ is calculated from the Gauss theorem to obtain $\overline{(\nabla \cdot (-|\mathbf{u}| \nabla\alpha^n))_i}$. An explicit Euler scheme is used for the discretization of the anti-diffusion equation in pseudo time.

**Calculation of $\overline{(\nabla\alpha^n)}$** Given cells P and its direct neighbors according to Fig. 2.3, first the cell-averaged gradient $\overline{(\nabla\alpha^n)}$ is calculated for the cell P by

$$\overline{(\nabla\alpha^n)} = \frac{\sum_{cf} (\alpha^n \mathbf{S})}{V} \quad . \tag{2.22}$$

$\sum_{cf}$ denotes the summation over all cell faces, $\mathbf{S}$ is the cell surface area vector, $V$ is the cell volume. $\alpha^n$ is obtained by averaging the volume fractions of the cell P and the respective neighbor N

$$\frac{\alpha_P^n d_N + \alpha_N^n d_P}{d_P + d_N} \ ,$$

where $\alpha_P^n$ and $\alpha_N^n$ are the volume fractions of cell P and N, and $d_P$ and $d_N$ are the distances from the cell centers P and N to the respective cell face centers. The directional derivative from cell P to cell N $\frac{\partial \alpha^n}{\partial c}$ is approximated as

$$\frac{\partial \alpha^n}{\partial c} \approx \frac{\alpha_N^n - \alpha_P^n}{|\mathbf{c}_N - \mathbf{c}_P|} \quad , \tag{2.23}$$

where $\mathbf{c}_P$ and $\mathbf{c}_N$ are the cell-center-position vectors of cell P and N respectively.

As the next step, $\overline{(\nabla\alpha^n)_P}$ is projected onto the cell-face-normal direction, leading to $\overline{(\nabla\alpha^n)_P} \cdot \hat{\mathbf{n}}_{cf}$, where $\hat{\mathbf{n}}_{cf}$ is the cell-face unit normal between the cells P and N. $\overline{(\nabla\alpha^n)_P} \cdot \hat{\mathbf{n}}_{cf}$ and $\frac{\partial \alpha^n}{\partial c}$ are compared to select the volume fraction $\alpha'^n$ from $\alpha_P^n$ and $\alpha_N^n$ for calculating the limited gradient of volume fraction in the next step. The selection is equivalent to (2.18) in the 1-dimensional setting. Direction and magnitude

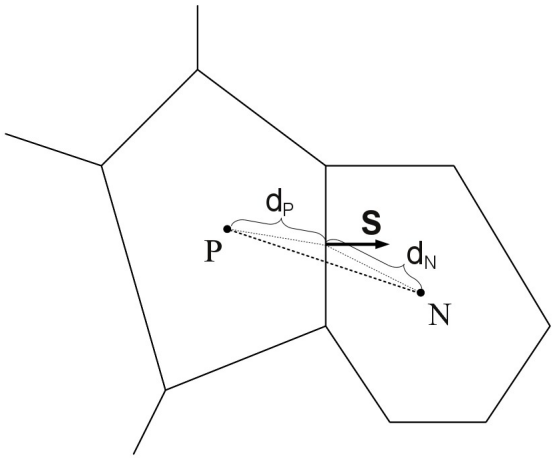


Figure 2.3: Cell arrangement for unstructured meshes.

of $\overline{(\nabla\alpha^n)_P} \cdot \hat{\mathbf{n}}_{cf}$ and $\frac{\partial\alpha^n}{\partial c}$ are compared for choosing the volume fraction as

$$\alpha'^n = \begin{cases} \alpha_N^n & \text{if } \overline{(\nabla\alpha^n)_P} \cdot \hat{\mathbf{n}}_{cf} \frac{\partial\alpha^n}{\partial c} > 0 \text{ and } \left|\overline{(\nabla\alpha^n)_P} \cdot \hat{\mathbf{n}}_{cf}\right| < \left|\frac{\partial\alpha^n}{\partial c}\right| \\ \frac{\alpha_P^n d_N + \alpha_N^n d_P}{d_P + d_N} & \text{if } \overline{(\nabla\alpha^n)_P} \cdot \hat{\mathbf{n}}_{cf} \frac{\partial\alpha^n}{\partial c} > 0 \text{ and } \left|\overline{(\nabla\alpha^n)_P} \cdot \hat{\mathbf{n}}_{cf}\right| = \left|\frac{\partial\alpha^n}{\partial c}\right| \\ \alpha_P^n & \text{else} \end{cases} \quad . \tag{2.24}$$

This procedure is applied to all cell pairs P and N.

Finally, the cell-averaged value of the volume-fraction gradient $\overline{(\nabla\alpha^n)_P}$ for cell P is calculated by the Gauss theorem using $\alpha'^n$

$$\overline{(\nabla\alpha^n)_P} = \frac{\sum_{cf}(\alpha'^n \mathbf{S})}{V} \quad . \tag{2.25}$$

This procedure is equivalent to step (2.17) in the 1-dimensional setting. Comparing (2.25) to the equation (2.22), it can be recognized that regularization is achieved by replacing cell-face values of $\alpha$ obtained from an arithmetic average by the $\alpha$ obtained from the above selection procedure.

**Divergence of** $(-|\mathbf{u}|\nabla\alpha^n)$ Equivalent to the flux calculation in the 1-dimensional setting, the flux at the cell face between cell P and cell N is limited by selection based on the minimum of $|\overline{(\nabla\alpha^n)_P}|$ and $|\overline{(\nabla\alpha)_N}|$

$$\overline{(\nabla\alpha^n)_P} = \begin{cases} \overline{(\nabla\alpha^n)_P} & \text{if } |\overline{(\nabla\alpha^n)_P}| \leq |\overline{(\nabla\alpha^n)_N}| \\ \overline{(\nabla\alpha^n)_N} & \text{if } |\overline{(\nabla\alpha^n)_N}| < |\overline{(\nabla\alpha^n)_P}| \end{cases} \quad . \tag{2.26}$$

The limited flux is multiplied by the diffusion coefficient $-|\mathbf{u}_{PN}|$

$$\mathbf{u}_{PN} = \frac{\frac{\mathbf{u}_P d_N + \mathbf{u}_N d_P}{d_P + d_N} \cdot \mathbf{S}}{|\mathbf{S}|} \ , \tag{2.27}$$

i.e. the magnitude of the linear-averaged velocity at the cell face between cell P and cell N. The diffusion for cell P is then calculated by the Gauss theorem as

$$\overline{\nabla \cdot \left(-|\mathbf{u}| \left(\nabla \alpha^n\right)\right)_P} = \frac{\sum_{cf} \left( \left( -|\mathbf{u}_{PN}| \overline{\left(\nabla \alpha^n\right)_P} \right) \cdot \mathbf{S} \right)}{V} \quad . \tag{2.28}$$

**Time-step criterion** The time derivative is discretized by an explicit Euler scheme. The volume fraction is forwarded in pseudo time by

$$\alpha_P^{n+1} = \alpha_P^n + \overline{\nabla \cdot \left(-|\mathbf{u}| \left(\nabla \alpha^n\right)\right)_P} \Delta\tau \quad , \tag{2.29}$$

where $\alpha_P^{n+1}$ and $\alpha_P^n$ are the volume fractions at the new and the old time step respectively. In the 1-dimensional setting the stability requirement (A.2) for the stabilized inverse diffusion equation applies. From numerical experimentation, it is found that stable time integration for multiple dimensions, unstructured meshes and variable diffusion coefficient is ensured by

$$\Delta\tau = \frac{1}{4} \frac{\left(\Delta x_{min}\right)^2}{|\mathbf{u}|_{max}} \quad , \tag{2.30}$$

where $\Delta x_{min}$ is the minimum cell width and $|\mathbf{u}|_{max}$ the maximum velocity magnitude over the entire computational domain.

**Stopping criterion for the anti-diffusion correction** A stopping criterion for the anti-diffusion correction in multiple dimensions and unstructured meshes uses $\nabla \cdot (-|\mathbf{u}| \nabla \alpha^n)$ as interface-steepness measure. Sharpness tolerances $TOL_1$ and $TOL_2$ are defined as

$$TOL_1 = \frac{\sum_i \left| \left( \overline{\nabla \cdot \left( \overline{\nabla \alpha} \right)_{lim}} \right)_i \right| V_i}{\sum_i |\left( \left( \overline{\nabla \alpha} \right)_{CD} \right)_i|^2 V_i} \quad , \tag{2.31a}$$

$$TOL_2 = \frac{\max_i \left( \left| \left( \overline{\nabla \cdot \left( \overline{\nabla \alpha} \right)_{lim}} \right)_i \right| V_i \right)}{\max_i \left( |\left( \left( \overline{\nabla \alpha} \right)_{CD} \right)_i|^2 V_i \right)} \quad . \tag{2.31b}$$

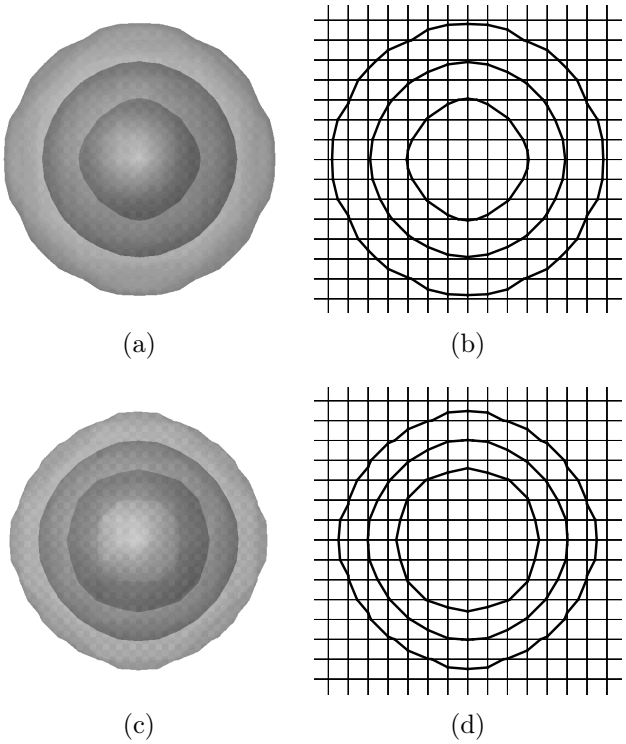


Figure 2.4: Volume-fraction contours 0.05, 0.5 and 0.95 of a 3-dimensional diffused profile. (a) Initial profile (3-dimensional view). (b) Initial profile (cross section). (c) Profile after 4 anti-diffusion corrections steps (3-dimensional view). (d) Profile after 4 anti-diffusion correction steps (cross section).

where $\left(\overline{\nabla \cdot \left(\overline{\nabla\alpha}\right)_{lim}}\right)_i$ is the solution obtained for the anti-diffusion equation in the 3-dimensional setting, and $\left(\left(\overline{\nabla\alpha}\right)_{CD}\right)_i$ is the gradient obtained from the central difference scheme. For demonstrating the effect of the tolerances, the anti-diffusion correction is applied to a steady diffused 3-dimensional profile, Fig. 2.4. The corresponding evolution of $TOL_1$ and $TOL_2$ is shown in Fig. 2.5. For pure transport, it is found by numerical experimentation that proper interface sharpness, ensuring overall stability of the interface evolution, can be achieved under the criterion that the anti-diffusion interface sharpening stops when $TOL_1$ and $TOL_2$ fall below 1. These interface-sharpness tolerances are used throughout all numerical computations in this work. It is found that in general the number of anti-diffusion step per advection is less than 5 times, while in most cases only 1 to 2 times of anti-diffusion correction per advection suffice for attaining the desired $TOL_1$ and $TOL_2$.

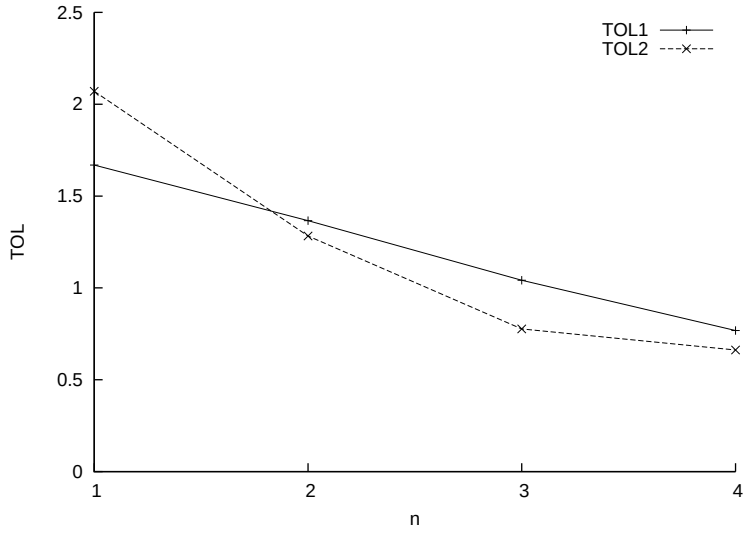


Figure 2.5: Evolution of $TOL_1$ and $TOL_2$ corresponding to the anti-diffusion correction in Fig. 2.4. $n$ denotes the number of anti-diffusion correction steps.

## 2.4 Numerical results

The anti-diffusion interface-steepening technique is validated with the following numerical examples. First, four passive-transport cases illustrate the interface-sharpening technique with pure advection. Following suggestions from literature [46, 62, 123, 75], a linearly advected square, a rotating circle, the Zalesak's disk problem and the single vortex case are considered. Second, five realistic flow configurations serve to study the fully coupled problem: a 2-dimensional rising bubble [62], a 3-dimensional axisymmetric rising bubble [31], a 3-dimensional rising bubble [6], the merging of two bubbles [111], and finally a 3-dimensional axisymmetric rising drop on a non-Cartesian mesh [29]. For all cases in the following section, the volume-fraction-transport equation is discretized by the van Leer MUSCL scheme [112] in space and a third-order TVD Runge-Kutta method for time integration. All computations are carried out with a CFL number of 0.5 for volume-fraction transport and momentum transport.

### Translation of square interface

The case of a square interface advected by a uniform velocity field [46] is used to validate the interface-sharpening method for a pure advection. A square of size $(l_{ref} \times l_{ref})$ is filled with phase "1". At the center of the domain a smaller square of size $\left(\frac{1}{8}l_{ref} \times \frac{1}{8}l_{ref}\right)$ with phase "2" is initialized. The reference length $l_{ref}$ is set to be 0.125. A uniform velocity field $(u, v) = (1, -1)$ is used to propagate phase "2" towards the lower right domain corner. Five levels of grid resolutions by dyadic refine-

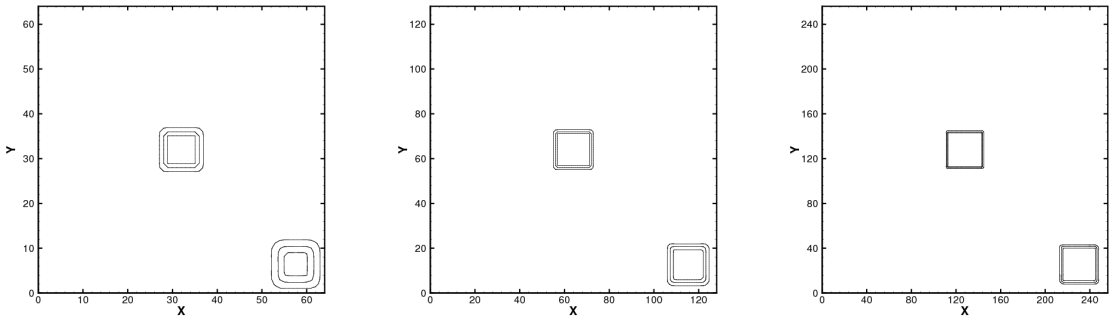


Figure 2.6: Volume-fraction contours 0.05, 0.5, 0.95 of the advected square at initial (center) and final (corner) positions for three different grid resolutions. From left to right: $64 \times 64$, $128 \times 128$, $256 \times 256$.

ment from $16 \times 16$ to $256 \times 256$ are used. For an overall impression volume-fraction contours 0.05, 0.5 and 0.95 of the square at $t = 0$ and at $t = 0.05$ are shown in Fig. 2.6. The results show that the square shape is well preserved for different grid resolutions, and compares well with interface-capturing methods where interface sharpening is built directly into the volume-fraction transport equation [14]. In order to study the order of accuracy of the advection together with the anti-diffusion correction, the $L_1$ error and the truncation error of the volume fraction field at $t = 0.05$ are calculated and shown in Table. 2.1, indicating an error of $\mathcal{O}(\Delta x)$ before round-off effects set in.

| Grid resolution | L1 error | error order |
|---|---|---|
| $16 \times 16$ | 0.020432 | |
| $32 \times 32$ | 0.008762 | 1.22 |
| $64 \times 64$ | 0.004239 | 1.05 |
| $128 \times 128$ | 0.001530 | 1.47 |
| $256 \times 256$ | 0.001058 | 0.53 |

Table 2.1: $L_1$ error and order of the truncation error at $t = 0.05$ for the moving-square case.

## Rotation of circular interface

The case of a rotating circle in a constant velocity field of Olsson and Kreiss [62] is considered. The computational domain, filled with phase "1", is defined as $2l_{ref} \times 2l_{ref}$. A circle of a diameter 0.5, filled with phase "2", is initialized at $(0.25, 0.25)$ with the

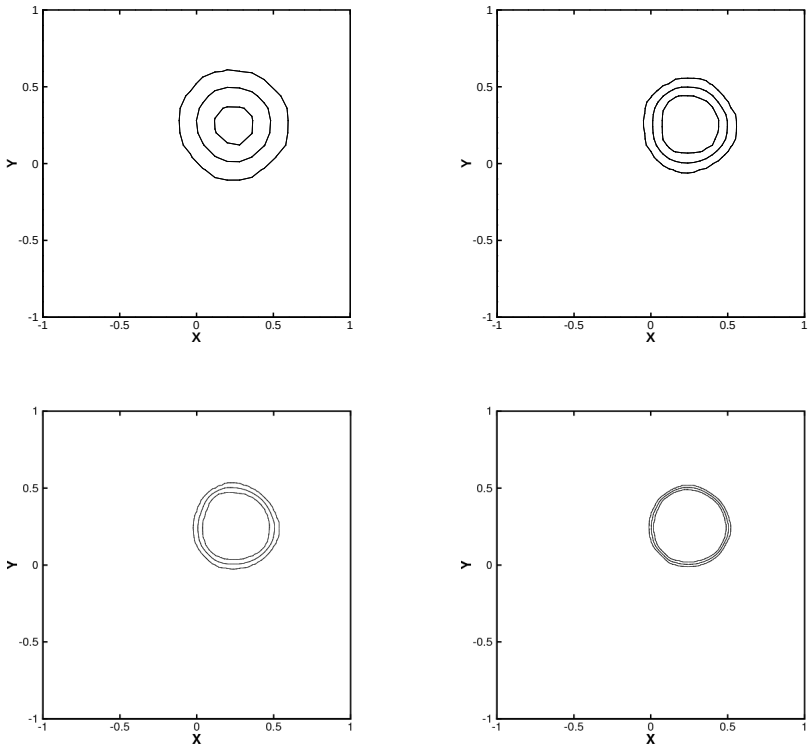


Figure 2.7: Volume-fraction contours 0.05, 0.5, 0.95 of the rotating circle at $t = 2\pi$ for four different grid resolutions. From left to right, top to bottom: $\Delta x = 0.08$, $\Delta x = 0.04$, $\Delta x = 0.02$,$\Delta x = 0.01$.

initial profile given by a smoothed Heaviside function

$$H_{sm}(\alpha) = \begin{cases} 0 & \alpha < -\epsilon \\ \frac{1}{2} + \frac{\alpha}{2\epsilon} + \frac{1}{2\pi}\sin\left(\frac{\pi\alpha}{\epsilon}\right) & -\epsilon \leqslant \alpha \leqslant \epsilon \\ 1 & \alpha > \epsilon \end{cases} . \tag{2.32}$$

where $\epsilon = \Delta x/2$. A constant velocity field $(u, v) = (y, -x)$ is imposed, and the circle is subjected to a rotation for one revolution about the domain center $(0, 0)$. Four different grid resolutions are used $\Delta x = 0.08$, $\Delta x = 0.04$, $\Delta x = 0.02$, and $\Delta x = 0.01$. Volume-fraction contours 0.05, 0.5 and 0.95 of the circle after one revolution are plotted in Fig. 2.7. The general shape of the circle is preserved under different grid resolutions. The interface sharpness is maintained at 2 to 3 cells. The $L_1$ error and the order of the truncation error are given in Table 2.2, demonstrating again an error of $\mathcal{O}(\Delta x)$.

| Grid resolution | L1 error | error order |
|---|---|---|
| $\Delta x = 0.08$ | 0.010027 | |
| $\Delta x = 0.04$ | 0.005505 | 0.87 |
| $\Delta x = 0.02$ | 0.003364 | 0.71 |
| $\Delta x = 0.01$ | 0.001682 | 1.00 |

Table 2.2: $L_1$ error and order of the truncation error at $t = 2\pi$ for the rotating-circle case.

## Zalesak disk problem

The solid-body rotation case of Zalesak [123], which is known as the "Zalesak disk problem", is considered. The computational domain, filled with phase "1", is discretized by 100×100 cells. A disk of phase "2" with 15 cells spanning the radius, and a slot of a width of 5 cells and a depth of 25 cells is initialized at the position $(50\Delta x, 75\Delta x)$ as shown in Fig. 2.8(a), where $\Delta x$ is a constant grid spacing. The disk is subjected to an anti-clockwise rotating flow about the position $(50\Delta x, 50\Delta x)$ for one revolution. No-slip boundary conditions are enforced at all four domain boundaries. In addition to the computation in Cartesian grid, in order to demonstrate the performance of the advection together with the anti-diffusion correction, the case is computed on a non-Cartesian grid, with a total number of cells of about $100^2$, as shown in Fig. 2.8(c).

Volume-fraction contours 0.05, 0.5 and 0.95 of the Zalesak disk after one revolution for the Cartesian grid and for the non-Cartesian grid are shown in Fig. 2.8(b) and (d). The general shape of the Zalesak disk after one revolution is preserved on Cartesian and non-Cartesian grids, with a performance comparable to other VOF interface capturing methods, e.g. [114].

## Single vortex case

The single vortex case of Rider and Kothe [75] is considered. The case has served as a standard validation case for various two-phase flow numerical methods. The case setup of [62] is adopted here for a direct comparison.

A circle of phase "1" and a radius of $0.15l_{ref}$ is initialized within a square domain of phase "2" and size $(l_{ref} \times l_{ref})$ at the position $(0.5l_{ref} \times 0.75l_{ref})$. The interface is defined by a smoothed Heaviside function (2.32) with $\epsilon = (\Delta x)^{0.9}/2$. Cartesian girds with four different grid resolutions are used: $32^2$, $64^2$, $128^2$, $256^2$. In addition, the case is computed on a non-Cartesian grid which is similar to the grid shown in Fig. 2.8(c), with approximately $256^2$ cells. No-slip boundary conditions are enforced at all four domain boundaries.

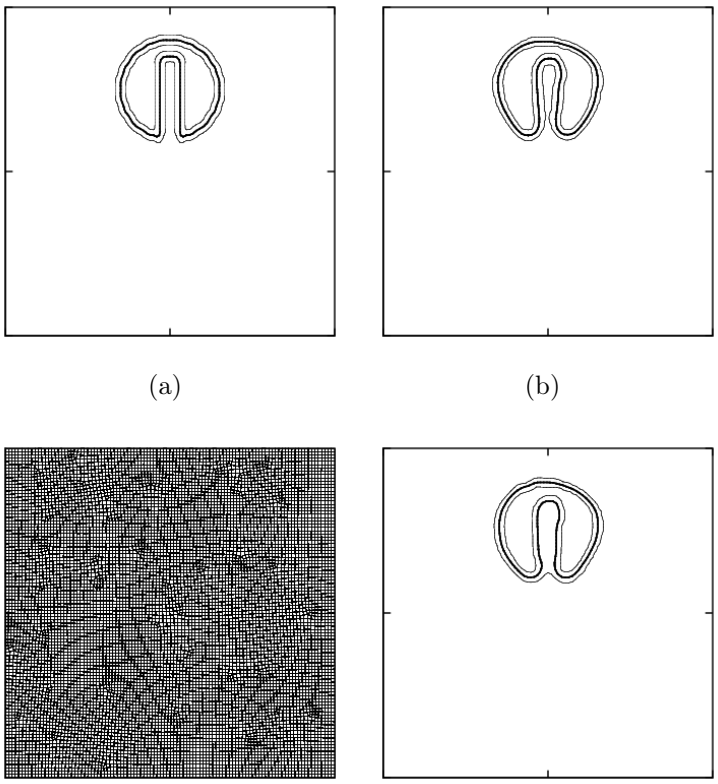


Figure 2.8: Volume-fraction contours 0.05, 0.5 and 0.95 of the Zalesak disk. The thick solid line refers to contour 0.5 and the thin solid line to contours 0.05 and 0.95. (a) Initial contour. (b) Contour after one revolution in Cartesian grid. (c) Non-Cartesian grid with approximately $100^2$ cells. (d) Contour after one revolution in non-Cartesian grid.

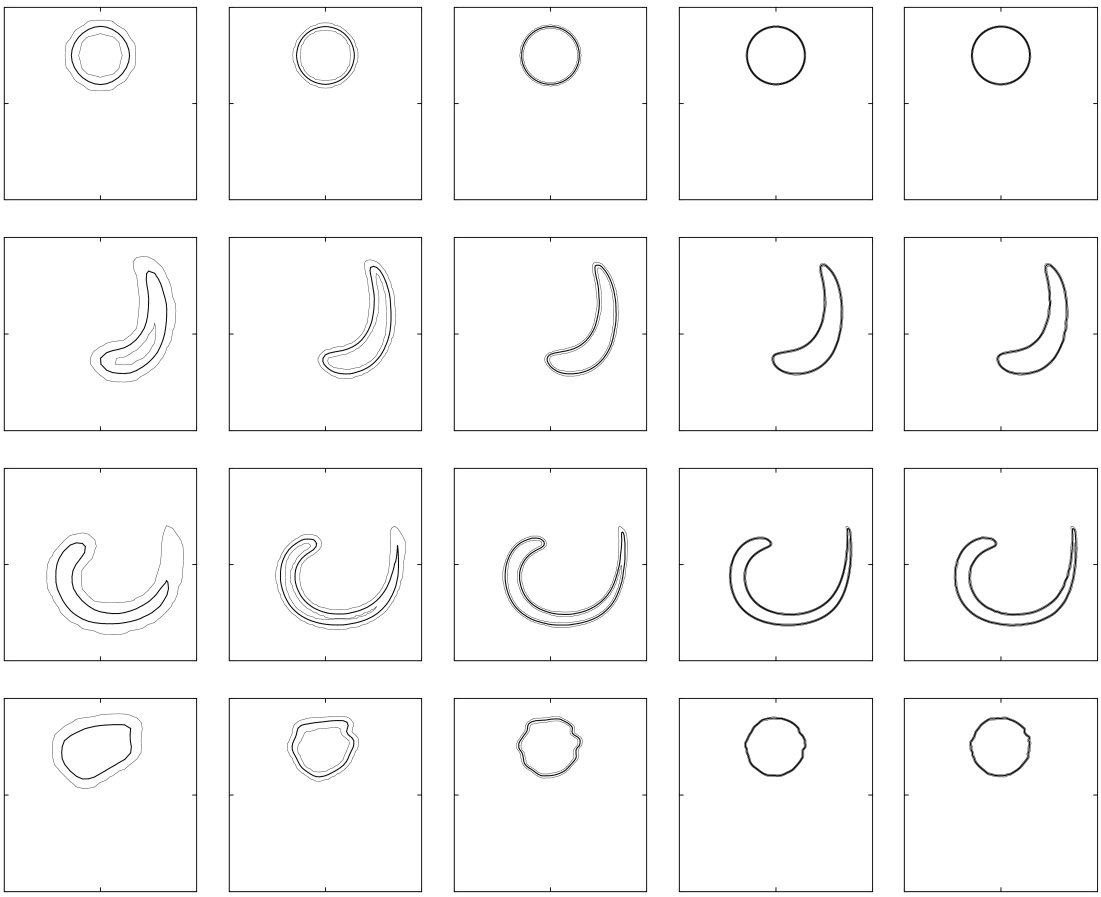

Figure 2.9: Volume-fraction contours 0.05, 0.5 and 0.95 of the single vortex. The thick solid line refers to contour 0.5 and the thin solid line to contours 0.05 and 0.95. Rows from top to bottom: $t = 0$, 0.5, 1, 2. Columns from left to right: $32^2$, $64^2$, $128^2$, $256^2$, the non-Cartesian grid of approximately $256^2$ cells.

The circle is first subjected to a clockwise-direction rotation, with the velocity field defined as: $u = -\sin^2(\pi x)\sin(\pi y)$, $v = \sin^2(\pi y)\sin(\pi x)$. $u$ is the velocity in x-direction and $v$ the velocity in y-direction. At time, $t = 1$ the flow is reversed to an anti-clockwise orientation, by reversing the signs of $u$ and $v$. At $t = 2$ the circle should recover the initial profile.

Volume-fraction contours 0.05, 0.5 and 0.95 of the circle at $t = 0$, 0.5, 1, 2 on a Cartesian grid and a non-Cartesian grid are plotted in Fig. 2.9. One can note that the results obtained by the proposed method do not show pinch-off artifacts at $t = 1$, as compared to the results in [62].

At $t = 2$, the advected profile is compared to the initial circular profile. The $L_1$ error and the order of the truncation error calculated for the Cartesian-grid cases are given in Table. 2.3, demonstrating an error of $\mathcal{O}(\Delta x)$.

Another simulation is conducted where the circle is subjected to the clockwise-

| Grid resolution | L1 error | error order |
|---|---|---|
| $32 \times 32$ | 0.03624 | |
| $64 \times 64$ | 0.01390 | 1.38 |
| $128 \times 128$ | 0.006015 | 1.21 |
| $256 \times 256$ | 0.002652 | 1.18 |

Table 2.3: $L_1$ error and order of the truncation error at $t = 2$ for the single vortex case.

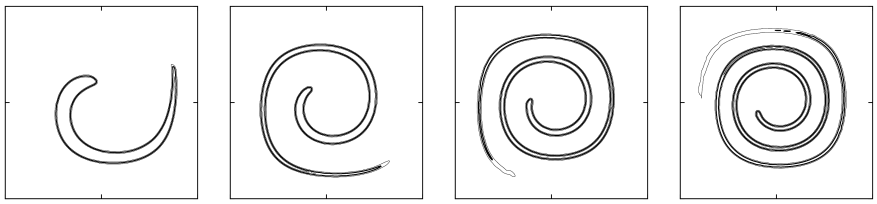

Figure 2.10: Volume-fraction contours 0.05, 0.5 and 0.95 for the single-vortex case on a Cartesian grid $256^2$. The thick solid line refers to contour 0.5 and the thin solid line to contours 0.05 and 0.95. From left to right: $t = 1$, 2, 3, 4.

direction vortical flow up to $t = 4$ on the Cartesian grid of $256^2$. The result, Fig. 2.10, represents the stretched filament without major artifacts, unlike the results in [62].

## Two-dimensional rising bubble

The 2-dimensional rising-bubble case of Olsson and Kreiss [62] is considered. The parameters of this case are: $\rho_1 = 1$, $\rho_2 = 0.0013$, $\mu_1 = 1$, $\mu_2 = 0.016$, $\sigma = 7.3 \times 10^{-2}\, N/m$, $Re = 500$, $Fr = 0.45$, $We = 0.68$, where $\rho$ is the density, $\mu$ is the liquid viscosity, $\sigma$ is the surface tension of the liquid, and the subscripts 1 and 2 refer to the water phase and the air phase, respectively. Reference parameters are $\rho_{ref} = 1.0 \times 10^3 kg/m^3$, $l_{ref} = 5.0 \times 10^{-3}\, m$ and $u_{ref} = 0.1\, m/s$. The computational domain size is $2l_{ref} \times 4l_{ref}$. The interface is defined by a smoothed Heaviside function (2.32) with $\epsilon = (\Delta x)^{0.9}/2$, and initially centered at $(l_{ref},\, l_{ref})$. Four different grid resolutions are used: $\Delta x = 2/25$, $\Delta x = 2/50$, $\Delta x = 2/100$, $\Delta x = 2/200$. No-slip boundary conditions are enforced at all four domain boundaries.

Volume-fraction contours 0.05, 0.5, and 0.95 of the bubble at $t = 0.5$ obtained by the anti-diffusion interface-sharpening method are shown in Fig. 2.11(a). The result of [62] is reproduced in Fig. 2.11(b) for comparison.

The bubble shapes at lower grid resolutions reproduce already the spherical-cap type, where the results are significantly better than that of [62]. It is also apparent that the prediction of the rising velocity in the present simulations is improved compared to that of [62], as shown in Fig. 2.12(b).

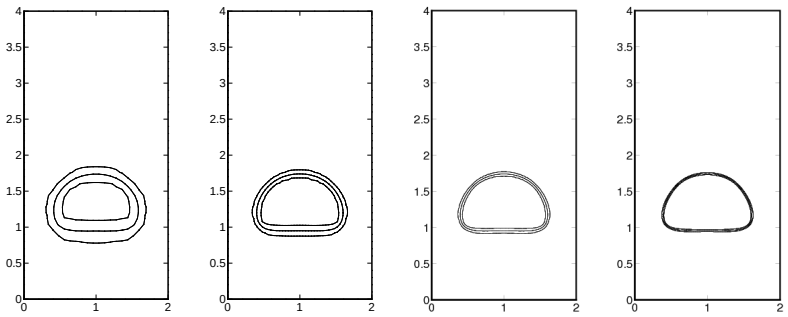

(a)

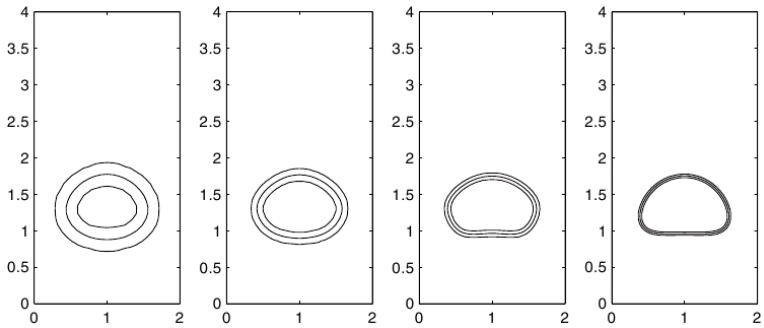

(b)

Figure 2.11: Volume-fraction contours 0.05, 0.5, 0.95 of the 2-dimensional rising bubble at $t = 0.5$ for four different grid resolutions. From left to right: $\Delta x = 2/25$, $\Delta x = 2/50$, $\Delta x = 2/100$,$\Delta x = 2/200$. (a) Result by anti-diffusion interface sharpening. (b) Result of [62], reproduced with permission.

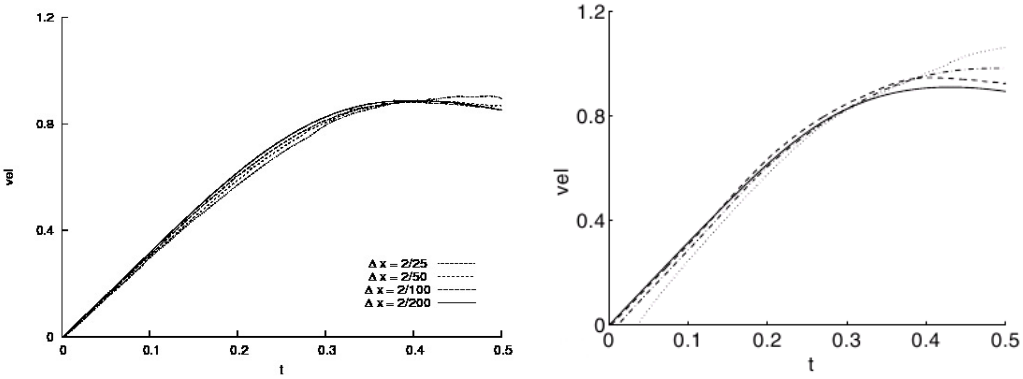


(a) (b)

Figure 2.12: Rising velocity of the 2-dimensional bubble for four different grid resolutions. (a) Result by anti-diffusion interface sharpening. (b) Result of [62], reproduced with permission. Dotted line: $25 \times 50$; dashed-dotted line: $50 \times 100$; dashed line: $100 \times 200$; solid line: $200 \times 400$.

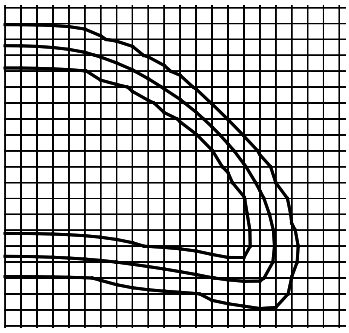

Figure 2.13: Cross section of volume-fraction contours 0.05, 0.5 and 0.95 of the stationary bubble at $t = 1.2s$.

## Axisymmetric rising bubble

To validate against experimental results of rising bubbles, the spherical cap bubble case of Hnat and Buckmaster [31] is considered. As in [101, 102], the rising bubble case is studied by 3-dimensional axisymmetric simulations.

The case refers to the spherical cap bubble "A" in [31]. The main flow parameters are given in Table 1 in [31]: $\rho_{liq} = 875.5\, kgm^{-3}$, $\mu_{liq} = 0.118 kgm^{-1}s^{-1}$, $\sigma_{liq} = 3.22 \times 10^{-2}\, Nm^{-1}$, $V = 9.4 \times 10^{-7}\, m^3$, and the relations given in [101] is used to calculate the air properties: $\rho_{liq}/\rho_{air} = 714$, $\mu_{liq}/\mu_{air} = 6667$, where $\rho$ is the density, $\mu$ is the viscosity, $\sigma$ is the surface tension, $V$ is the measured bubble volume and the subscripts $air$ and $liq$ refer to the air phase and the test-liquid phase, respectively. The Reynolds number, $Re_{\bar{r}}$, based on the effective bubble radius, $\bar{r}$, are defined as:

$$Re_{\bar{r}} = \frac{\rho_{liq} U \bar{r}}{\mu_{liq}}, \qquad \bar{r} = \left(\frac{3}{4\pi} V\right)^{1/3} \quad ,$$

where $U$ is the rising velocity.

The computational-domain size is $5\bar{r} \times 20\bar{r}$, discretized at a grid-resolution of $64 \times 256$. A spherical bubble of radius $\bar{r}$ is initialized at a height $4\bar{r}$. No-slip boundary conditions are enforced at all four domain boundaries.

The bubble reaches a stationary shape and the terminal rising velocity soon after the bubble starts to rise. Volume-fraction contours 0.05, 0.5, and 0.95 of the bubble at $t = 1.2s$ are shown in Fig. 2.13. The bubble shape agrees well with the experimental image in [31] and the interface sharpness is maintained across 2 to 3 cells. The rising velocity obtained from the simulation is $20.3\, cm/s$, which compares well with the experimental result of $21.5\, cm/s$ as reported in [31].

## Three-dimensional rising bubble

For validation in 3 dimensions, the case of an air bubble rising in a water-glucose solution based on the experiment of Bhaga and Weber [6] is considered. The configuration is characterized by the Reynolds number, the Eötvös number and the Morton number

$$Re = \frac{\rho d_B U_B}{\mu} = 2.47, \qquad E\ddot{o} = \frac{g d_B^2 \rho}{\sigma} = 116, \qquad Mo = \frac{g\mu^4}{\rho\sigma^3} = 848 \quad ,$$

where $\rho$ is the liquid density, $d_B = 0.0261\,m$ is the bubble volume-equivalent diameter, $U_B$ is the bubble terminal rising velocity, $\mu$ is the liquid viscosity, $\sigma$ is the surface tension of the liquid and $g$ is the gravitational acceleration. The computational-domain size is $5d_B \times 10d_B \times 5d_B$. The grid resolution is $50 \times 100 \times 50$. A spherical bubble of diameter $d_B$ is initialized at ($2.5d_B$, $1d_B$, $2.5d_B$). The boundary condition at the front, back, left, right and bottom domain boundaries is set as no-slip wall. Corresponding to the experimental setup of a rising bubble in a vertical tube open to the atmosphere, the top boundary is treated by a mixed inlet-outlet boundary condition, depending on the direction of the velocity.

The bubble reaches a steady shape after an initial transient period. The volume-fraction contour 0.5 of the steady bubble at $t = 0.5\,s$ is shown in Fig. 2.14(a). The interface sharpness can be evaluated by the volume-fraction contours 0.05, 0.5 and 0.95 in Fig. 2.14(b). A terminal oblate-ellipsoidal-cap bubble shape is obtained, which corresponds to the experimental observation [6]. The rising velocity of the bubble is plotted in Fig. 2.15. The computed Reynolds number based on the predicted terminal rising velocity is 2.34, which compares well with the experimental Reynolds number of 2.47.

## Merging of two bubbles

To validate the robustness of the interface method in flow configurations with topology changes, the case of the merging of two bubbles of [111] is considered. The fluid parameters are: $E\ddot{o} = 50$, $Mo = 1$, $\rho_o/\rho_b = 20$, $\mu_o/\mu_b = 26$, where $\rho$ is the density, $\mu$ is the viscosity, the subscripts $o$ and $b$ refer to the outer-liquid phase and bubble phase respectively. The definitions of $E\ddot{o}$ and $Mo$ are:

$$E\ddot{o} = \frac{g l_{ref}^2 \rho_o}{\sigma}, \qquad Mo = \frac{g\mu_o^4}{\rho_o \sigma^3},$$

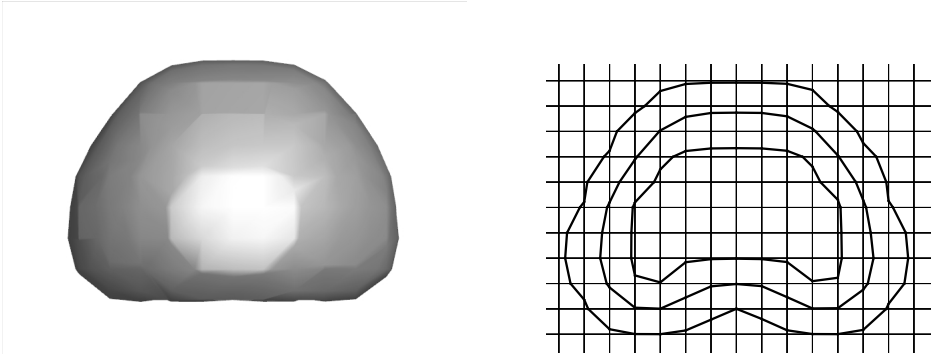

(a) (b)

Figure 2.14: (a) 3-dimensional view of volume-fraction contour 0.5 of the 3-dimensional rising bubble at steady state at $t = 0.5s$. (b) Cross section of volume-fraction contours 0.05, 0.5 and 0.95 of the stationary bubble at $t = 0.5s$.

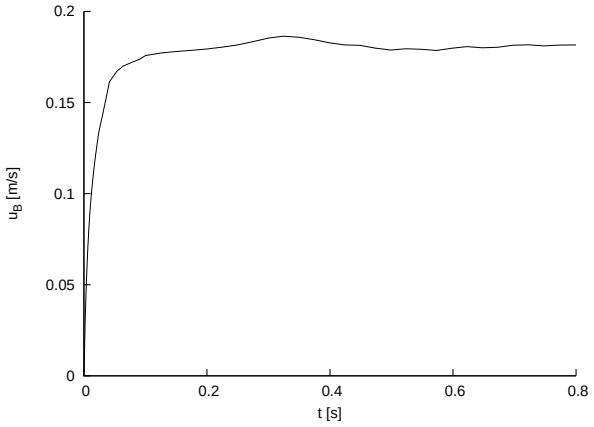


Figure 2.15: Rising velocity $u_B$ of the 3-dimensional bubble in the 3-dimensional rising-bubble case.

where $l_{ref}$ is the reference length, $\sigma$ the surface tension and $g$ the gravitational acceleration. The reference time is $t_{ref} = l_{ref}/U_{ref}$, and the reference velocity is $U_{ref} = \sqrt{g l_{ref}}$.

As in [52, 20], the domain is $4l_{ref} \times 8l_{ref} \times 4l_{ref}$. Two spherical bubbles with diameter $l_{ref}$ are initialized at positions $(2l_{ref}, 2l_{ref}, 2.15l_{ref})$ and $(2.5l_{ref}, 2l_{ref}, 1l_{ref})$. No-slip boundary conditions are enforced at all domain boundaries. The domain is discretized by a $64 \times 128 \times 64$ grid, which has the same effective grid resolution as [101].

The volume-fraction 3D contour of 0.5, and the cross section of the contours 0.05, 0.5 and 0.95 of the bubbles at $t_{ref} = 1.17$, 1.32, 1.63, 2.13 are plotted in Fig. 2.16 to illustrate bubble shape and interface thickness during the merging process. The results compare well with that in [108, 52, 20]. As is evident from the cross section of volume-fraction contours, the interface sharpness is maintained across 2 to 3 cells throughout the merging process. Note that at $t_{ref} = 2.13$ the tail of the lower bubble becomes under-resolved.

## Rising drop in a periodically constricted capillary tube

In order to validate the anti-diffusion correction algorithm for general meshes and comparably complex domains, a case of a drop rising in a periodically constricted capillary tube is considered. The case is based on the experiment of [29], and has been investigated by simulations in [56]. The parameters used in this numerical example are $\rho_o = 1160\,kg/m^3$, $\rho_d = 966\,kg/m^3$, $\mu_o = 87\,mPa\,s$, $\mu_d = 115\,mPa\,s$, $\sigma = 0.0042\,N/m$, where the subscripts $o$ and $d$ denote the ambient fluid and the drop fluid respectively. As in [56], a section of $26\,cm$ of a periodically constricted capillary tube is selected as the computational domain, shown in Fig. 2.17. The constricted capillary tube has the following geometric parameters: average radius, $R = 0.5\,cm$, wavelength of corrugations, $h = 4\,cm$, and amplitude of corrugations $A = 0.07\,cm$. The grid resolution of the computational domain is $32 \times 1664$. A drop is initialized at the height of $6\,cm$ along the centerline and its size is measured by $\kappa$ which is defined as the ratio of the equivalent spherical drop radius to $R$. The simulation time is non-dimensionalized by

$$t_{ref} = \frac{\mu_o}{\Delta\rho g_y R} \quad ,$$

where $t_{ref}$ is the reference time, $\Delta\rho = \rho_o - \rho_d$ and $g_y$ is the gravitational acceleration. The velocity is non-dimensionalized by

$$V_{ref} = \frac{\Delta\rho g_y R^2}{\mu_o} \quad ,$$

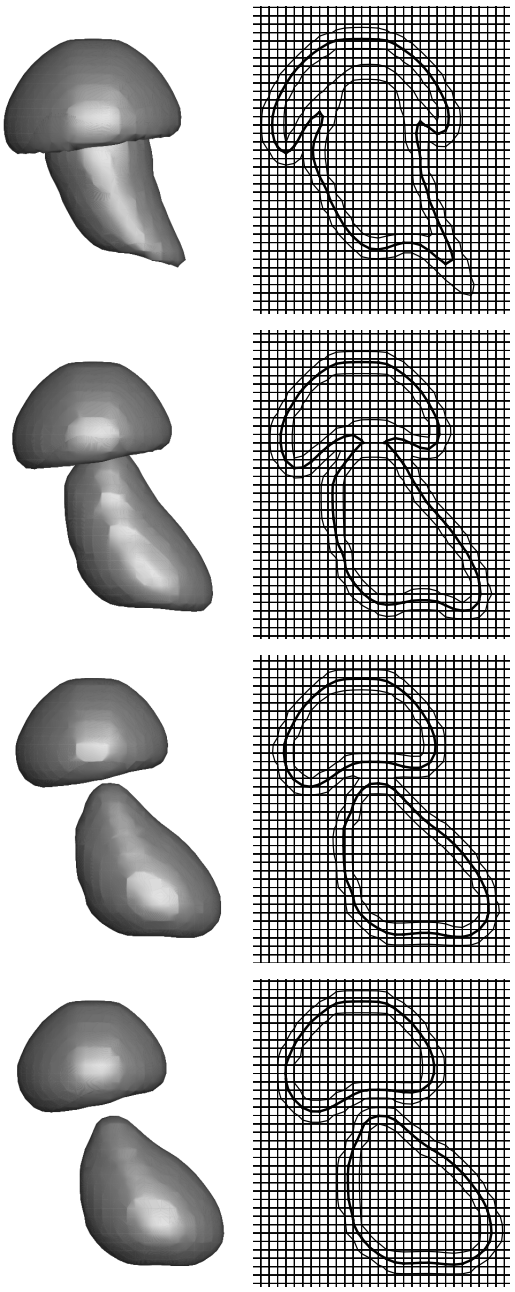

Figure 2.16: Volume-fraction contours 0.05, 0.5 and 0.95 of the two bubbles. Rows from bottom to top: $t_{ref} = 1.17$, 1.32, 1.63, 2.13. Left column: 3D contour of volume fraction 0.5. Right column: cross section of the volume fraction contours 0.05, 0.5 and 0.95. The thick solid line refers to contour 0.5 and the thin solid line to contours 0.05 and 0.95.

where $V_{ref}$ is the reference velocity. The drop position is characterized by $z$, which is the axial distance between the drop tip (defined from the volume-fraction contour 0.5) and the preceding constriction, normalized by the wavelength of corrugations, $h$. A similar parameter $z^*$ is defined as the axial distance between the drop tip and the constriction before the drop initial position, normalized by $h$. The drop shape is characterized by a deformation parameter $D$, which is defined as the ratio of the drop profile perimeter to that of the equivalent spherical drop, and by the axial length $L$, which is the axial length of the drop profile normalized by $h$. For comparison with the simulation of [56] and the experiment of [29], axisymmetric 3-dimensional simulations for $\kappa = 0.92$ and $\kappa = 0.95$ are carried out. Two different drop sizes are taken in order to determine the sensitivity of the results to $\kappa$ which is difficult to determine precisely from the experiments. The volume-fraction contours 0.05, 0.5 and 0.95 at different time instants are shown in Fig. 2.18(a) and (b), respectively. The periodic drop shapes at the constriction and expansion region for $\kappa = 0.92$ are shown in Fig. 2.19. A sharp interface is obtained on the underlying non-Cartesian mesh. Also, it can be seen that the drop shape is periodic with respect to the periodic corrugation. This is in good agreement with the experiment, where it is stated that the drop deformation parameter is found to be periodic for all drop sizes without drop breakup. Note that the simulations of [56] do not recover this behavior. The rising velocity of the mass centroid of the drop of $\kappa = 0.95$, $U_c$ is shown in Fig. 2.20. The velocity profile is periodic with respect to the periodic corrugation. The velocity evolution agrees reasonably with the experiment observations, where in [29] it is stated that for a drop of $\kappa > 0.7$, the rising velocity increases once the leading meniscus clears the throat. The average rising velocity across the constrictions is $0.97 \times 10^{-2}$, as compared to the experimental value of $0.9 \times 10^{-2}$. It is suspected that the difference of the average rising velocity may be due to an inconsistency of the Bond number as reported by [29], where $Bo = 13.0$ is specified explicitly in [29], however the Bond number calculated from the given material and geometry data with $Bo = \Delta\rho g R^2/\mu$ rather results in $Bo = 11.3$. The inconsistency is also reported by [56]. Despite the discrepancy of the velocity, the overall evolution, periodic motion of the drop and periodic profile of the rising velocity are well reproduced by the present method. The deformation parameter $D$ and the axial length $L$ for a drop of $\kappa = 0.95$ are compared with the experiment in Fig. 2.21 and Fig. 2.22, respectively. Extrema of the deformation parameter $D$ and its profile agree with the experiment, but the profile is shifted with respect to the axial coordinate. This shift is also observed for the axial length $L$. Again, this shift can be attributed to the inconsistency of the specified Bond number. For further assessment of simulation errors, results across successive constrictions are shown in Fig. 2.21 and

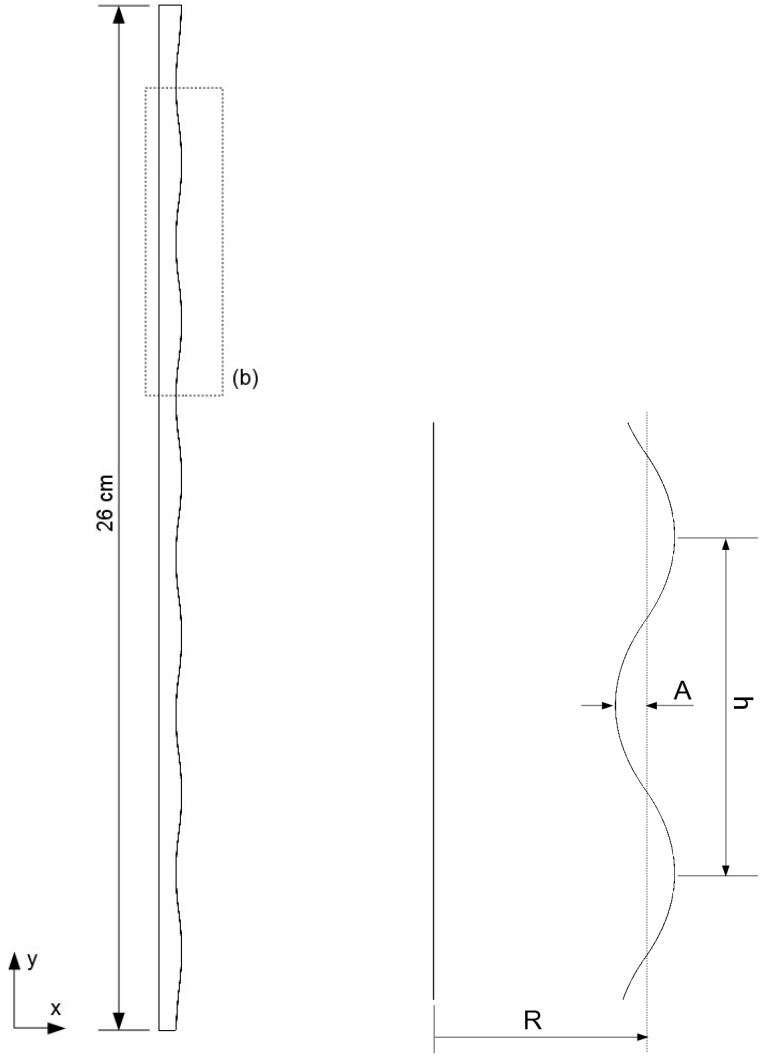


(a) (b)

Figure 2.17: Computational domain for the axisymmetric 3-dimensional rising drop in a periodically constricted capillary tube. (a) Full domain. (b) Plan view showing dimensional details (not to scale).

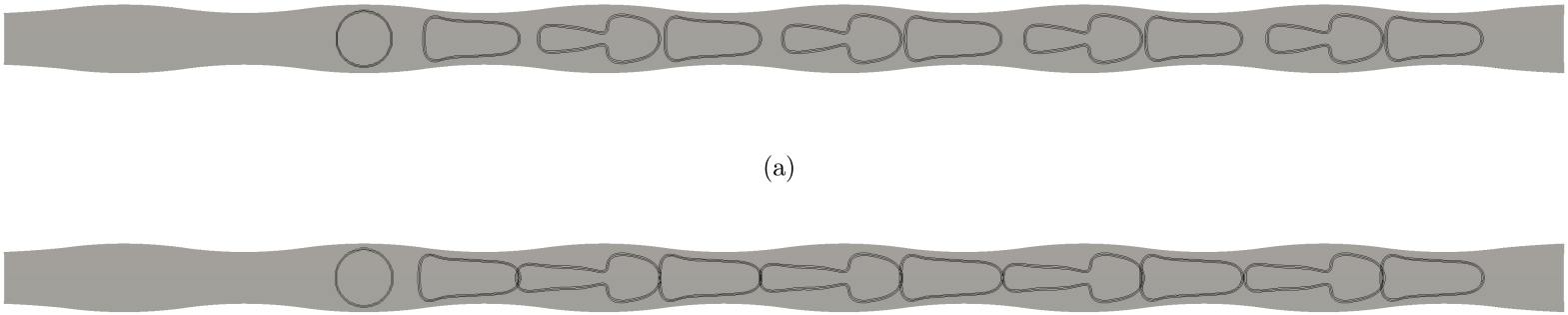

(a)

(b)

Figure 2.18: Volume-fraction contours 0.05, 0.5 and 0.95 of the rising drop between $t = 0$ and $t = 3773.8$. The first drop image refers to $t = 0$, and the remaining drop images of the periodic motion between $t = 492.2$ and $t = 3773.8$ at constant time increments. (a) $\kappa = 0.92$. (b) $\kappa = 0.95$.

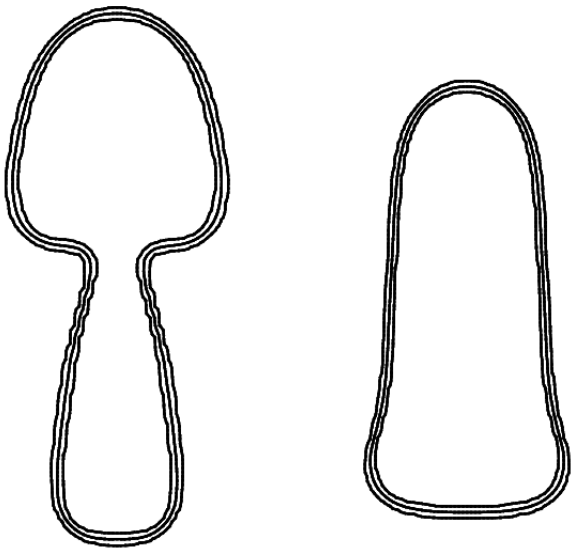

(a) (b)

Figure 2.19: Volume-fraction contours 0.05, 0.5 and 0.95 of the rising drop with $\kappa = 0.92$. (a) $t = 1722.8$. (b) $t = 2133.0$.

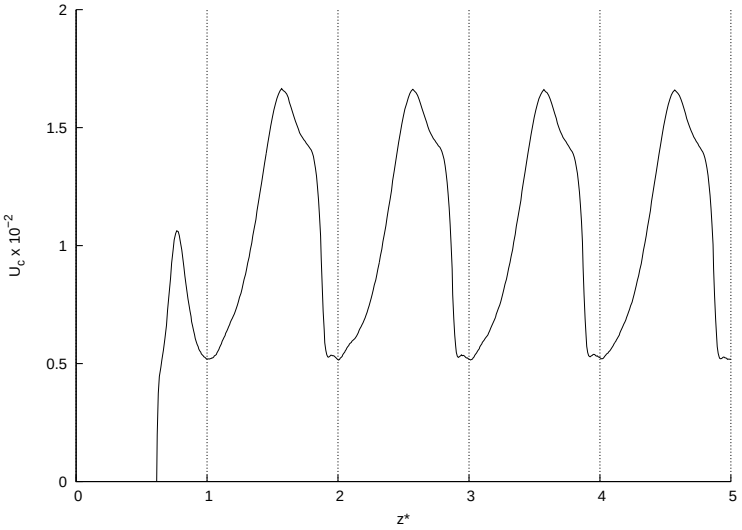


Figure 2.20: Rising velocity of the mass centroid of the drop at $\kappa = 0.95$ vs axial position $z^*$. The vertical dotted lines indicate the constriction nodes. $z^* = 1$ refers to the first constriction reached by the drop tip.

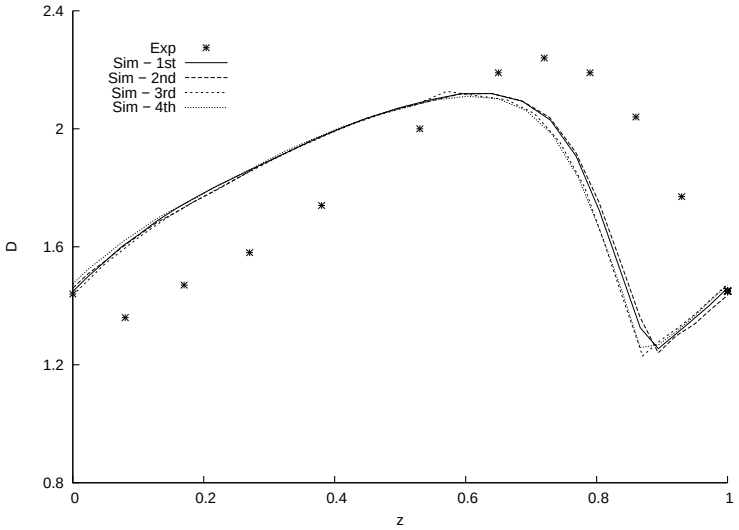


Figure 2.21: Deformation parameter $D$ of rising drop for experiment and simulation, $\kappa = 0.95$, within one period of corrugation. "Exp" denotes the experimental data. "Sim - 1st" denotes the simulation results for the first period of corrugation the drop passes through.

Fig. 2.22. With respect to the experiment, it is stated in [29] that the variation of single measurements is less than 5%. Also, in [29] it is stated that when a drop of $\kappa > 0.7$ reaches a constriction, the leading end follows the capillary wall contour and the drop is squeezed through the throat. Their statement implies that the drop should be continuously stretched from the onset of the constrictions, meaning that $D$ and $L$ should increase at $z = 0$. Such a behavior of $D$ and $L$ is observed in the present simulations but is not apparent from the experimental data [29].

Despite the discrepancies to the experiment, which may be related to an inconsistent specification of experimental parameters, this test case is significant for validation, as proper mass conservation and periodicity of the solution need to be reproduced by the simulation. The present simulation clearly recovers these properties, whereas some deficits in this respect can be observed for the simulations of [56].

## 2.5 Concluding remarks

In this chapter, an interface-sharpening technique by an anti-diffusion correction is presented for two-phase incompressible flows based on the VOF interface-capturing method. The method possesses the following properties:

- The interface-sharpening step is separate from the volume-fraction transport and thus can be used in conjunction with any underlying VOF schemes.

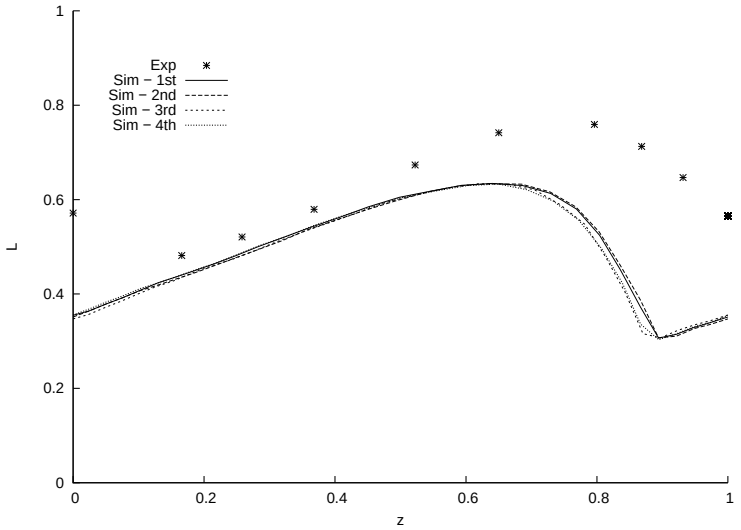


Figure 2.22: Axial length $L$ of rising drop for experiment and simulation, $\kappa = 0.95$, within one period of corrugation. "Exp" denotes the experimental data. "Sim - 1st" denotes the simulation results for the first period of corrugation the drop passes through.

- No interface reconstruction is required for the volume-fraction transport to achieve an accuracy similar to that of comparable (in terms of discretization-scheme accuracy) level-set approaches, while being conceptually simpler.

- A desired interface representation is maintained throughout the simulation based on a case- and grid-resolution independent, robust interface-sharpness measure.

The key ingredients of the interface-sharpening method are a regularization based on a *minmod* limiter and a grid-independent interface-sharpness measure. Starting from the standard *minmod* limiter with a 5-point stencil, an equivalent compact limiter, suitable for general, unstructured meshes has been formulated in 1 spatial dimension and extended to 3 dimensions. With this limiter a stable regularization of the discrete anti-diffusion equation is obtained that maintains a local extremum principle. The anti-diffusion correction is evolved in pseudo time after each advection step of the volume-fraction transport. In principle the anti-diffusion could be iterated until a steady state is achieved, that steady state, however, may extend the resolution capabilities of the underlying volume-fraction and flow-transport discretization beyond its limits. This is particularly important in higher dimensions as the discretization resolution becomes anisotropic. This issue can be handled by introducing a stopping criterion. The stopping criterion imposes two thresholds on the interface sharpness which is computed from a comparison of discrete volume-fraction divergence and discrete volume-fraction gradient. As these expressions are evaluated in the solution of

the anti-diffusion equation, the sharpness measure does not imply additional computational cost. The thresholds for the sharpness measure can be set to unity, and the overall solution is rather insensitive to these thresholds.

For demonstration and validation purposes, the anti-diffusion method is coupled with a discretization of the volume-fraction advection and the Navier-Stokes equation which is typical for practical applications in engineering for realistic flow simulations. Validation computations are performed for passive transport, a 2-dimensional and 3-dimensional rising-bubbles and a rising-drop configuration. These application examples involve Cartesian and non-Cartesian, unstructured meshes. The results agree well with reference data from literature and with experiments. In particular, the method is more accurate, even at low grid resolutions compared, e.g., to [62], and exhibits an improved accuracy. The challenging test case of a drop rising in a periodically constricted capillary tube demonstrates that the present method, while being rather simple, represents a significant improvement as compared to that of [56].

Two by-products of the anti-diffusion method may be also of more general interest to other computational modeling problems. First, as the proposed compact modification of the *minmod* function can be employed as a general slope limiter, it may also be applied more generally for discretization schemes on unstructured meshes. Second, as the proposed interface-steepness measure gives a general assessment of the quality and resolvability of a VOF interface representation, it may also be used in conjunction with other interface models.

# Chapter 3

# Interface-sharpening technique for two-phase compressible flow simulation

## 3.1 Introduction

In this chapter,the anti-diffusion technique presented in chapter 2 is extended to two-phase compressible flow simulations. Compressible flows pose the particular challenge of ensuring consistency among the flow variables during the interface-sharpening step. It is the objective of this chapter to present a further development of the interface-sharpening method for two-phase compressible flows with numerical validation results and some applications as feasibility demonstration.

This chapter is organized as follows: First, the governing equations for two-phase compressible flows adopted are described. Second, the underlying Riemann solver, the numerical method for the volume-fraction transport equation are detailed, and the numerical method for interface sharpening by solving an anti-diffusion equation is recapitulated. In particular, special consideration is given to modifications of the incompressible formulation necessary for compressible flows. Validation cases for different equations of state (EOS) and in 1 and 2 dimensions are then presented to illustrate the improvement obtained by the interface-sharpening method, where a detailed discussion of simulations of shock-bubble interactions and an application of the method to a complex interaction problem are given. Finally, the merits of the numerical method and the improvements achieved in numerical results are summarized in concluding remarks.

## 3.2 Governing flow equations

Various mathematical models for two-phase compressible flow simulations have been developed with different sets of governing equations [41, 83, 45]. In this work, a basic conservative formulation of the Euler equations assuming a single velocity and pressure equilibrium is employed. The two phases are represented by the respective volume fractions, where the formulation of the volume-fraction transport equations of [25] is adopted. This volume-fraction transport equation formulation has been extensively studied by [55] for simulations with the ideal-gas EOS and the Mie-Grüneisen EOS [74], and employed for a computational study of shock-bubble interactions of different gas pairs and at different shock speeds by [59]. With two volume-fraction-transport equations, two mass conservation equations, one momentum conservation equation and one energy conservation equation, a six-equation model is obtained as follows:

$$\frac{\partial \alpha}{\partial t} + \nabla \cdot \alpha \mathbf{u} = \alpha \frac{\overline{K}_S}{K_S^\alpha} \nabla \cdot \mathbf{u} \quad , \tag{3.1}$$

$$\frac{\partial \beta}{\partial t} + \nabla \cdot \beta \mathbf{u} = \beta \frac{\overline{K}_S}{K_S^\beta} \nabla \cdot \mathbf{u} \quad , \tag{3.2}$$

$$\frac{\partial \alpha \rho^\alpha}{\partial t} + \nabla \cdot \alpha \rho^\alpha \mathbf{u} = 0 \quad , \tag{3.3}$$

$$\frac{\partial \beta \rho^\beta}{\partial t} + \nabla \cdot \beta \rho^\beta \mathbf{u} = 0 \quad . \tag{3.4}$$

$$\frac{\partial \rho \mathbf{u}}{\partial t} + \nabla \cdot \rho \mathbf{u}\mathbf{u} + \nabla p = 0 \quad , \tag{3.5}$$

$$\frac{\partial \rho E}{\partial t} + \nabla \cdot (\rho E + p)\, \mathbf{u} = 0 \quad , \tag{3.6}$$

where $\alpha$ and $\beta$ are the volume fractions of the two phases respectively, $t$ is the time, $\mathbf{u}$ is the velocity, $\overline{K}_S$ is the mixture bulk modulus, $K_S^\alpha$ and $K_S^\beta$ are the phase bulk moduli, $\rho^\alpha$ and $\rho^\beta$ are the phase densities, $p$ is the pressure and $E$ is the total energy.

It should be noted that, instead of solving Eq. (3.2), $\beta$ can be computed directly from $\alpha$ based on the relation $\alpha + \beta = 1$. Here the original form of the volume-fraction transport equations (3.1) and (3.2) as adopted in [25] are maintained unchanged for demonstrating the modularity of the interface-sharpening method and the applicability of the method to general underlying VOF discretizations.

As the formulation of the volume-fraction transport equations are capable of simulations with the ideal-gas EOS and the Mie-Grüneisen EOS as studied in [25, 55, 59],

these two EOS are also considered in this work as examples. The ideal-gas EOS reads

$$p\left(\rho,e\right)=\left(\gamma-1\right)\rho e \quad , \tag{3.7}$$

where $\gamma$ is the ratio of specific heats and $e$ is the internal energy. The Mie-Grüneisen EOS reads

$$p\left(\rho,e\right)=p_{ref}+\Gamma\left(\rho\right)\rho\left(e-e_{ref}\right) \quad , \tag{3.8}$$

where $p_{ref}=\rho_0 c_0^2\eta/\left(1-s\eta\right)^2$, $\eta=1-\left(\rho_0/\rho\right)$, $\Gamma\left(\rho\right)=\Gamma_0\rho_0/\rho$, $e_{ref}=0.5p_{ref}\eta/\rho_0$ and $\rho_0$, $c_0$, $s$, $\Gamma_0$ are constant coefficients.

A general EOS can be formulated to represent both the ideal-gas EOS and the Mie-Grüneisen EOS. The general EOS for each phase reads

$$p^k\left(\rho^k,e^k\right)=\Gamma^k\left(\rho^k\right)\rho^k e^k+f^k\left(\rho^k\right) \quad , \tag{3.9}$$

where $\Gamma^k\left(\rho^k\right)$ and $f^k\left(\rho^k\right)$ are functions of $\rho^k$, and the superscript $k$ denotes the phase, i.e. $\alpha$ or $\beta$.

By assuming pressure equilibrium, i.e. $p^\alpha=p^\beta$ , $p$ can be calculated by

$$p\left(\rho,e,\alpha,\beta\right)=\frac{\rho e+\left(\frac{\alpha f^\alpha(\rho^\alpha)}{\Gamma^\alpha(\rho^\alpha)}+\frac{\beta f^\beta\left(\rho^\beta\right)}{\Gamma^\beta\left(\rho^\beta\right)}\right)}{\left(\frac{\alpha}{\Gamma^\alpha(\rho^\alpha)}+\frac{\beta}{\Gamma^\beta\left(\rho^\beta\right)}\right)} \quad . \tag{3.10}$$

## 3.3 Numerical methods

### Riemann solver

It should be pointed out that the particular choice of Riemann solver serves as an example for using the interface-sharpening method which can be formulated for other Riemann solvers in a straight-forward way.

The HLL Riemann solver [106] is adopted for calculating the numerical flux at the cell face, $\mathbf{F}_{HLL}$,

$$\mathbf{F}_{HLL}=\begin{cases}\mathbf{F}_L & \text{if } 0\le S_L,\\ \frac{S_R\mathbf{F}_L-S_L\mathbf{F}_R+S_LS_R(\mathbf{U}_R-\mathbf{U}_L)}{S_R-S_L} & \text{if } S_L\le 0\le S_R,\\ \mathbf{F}_R & \text{if } 0\ge S_R,\end{cases} \quad , \tag{3.11}$$

where $\mathbf{U}=\left(\alpha,\beta,\alpha\rho^\alpha,\beta\rho^\beta,\rho\mathbf{u},\rho E\right)$ is the vector of the cell-averaged conserved variables, $\mathbf{F}$ is the cell-average flux, $S$ is the bound of the fastest signal velocity,

and the subscripts $L$ and $R$ denote the variables at the cell face computed by the reconstructed values at the two sides of the cell face.

The lower and upper bounds of the fastest signal velocities are calculated by

$$S_L = \min\left(u_L - a_L, u_R - a_R\right) \quad , \quad S_R = \max\left(u_L + a_L, u_R + a_R\right) \quad , \tag{3.12}$$

where $u_L$ and $u_R$ are the flow velocity at the cell face, $a_L$ and $a_R$ are the mixture sound speeds at the cell face. The Wood formula or the frozen speed of sound [83] can be used for calculating $a_L$ and $a_R$, and the latter is adopted in this work as the numerical results do not show significant differences for both:

$$a_L = \sqrt{\frac{(\alpha\rho^\alpha)_L}{\rho_L}\left(c_L^\alpha\right)^2 + \frac{(\beta\rho^\beta)_L}{\rho_L}\left(c_L^\beta\right)^2} \quad , \quad a_R = \sqrt{\frac{(\alpha\rho^\alpha)_R}{\rho_R}\left(c_R^\alpha\right)^2 + \frac{(\beta\rho^\beta)_R}{\rho_R}\left(c_R^\beta\right)^2} \quad , \tag{3.13}$$

where $c_L^\alpha$, $c_R^\alpha$, $c_L^\beta$ and $c_R^\beta$ are the phase sound speeds at the cell face computed based on the respective EOS.

## Volume-fraction transport equations

The numerical method for solving the volume-fraction transport equations (3.1) and (3.2) is detailed in [25, 55] and illustrated below.

The volume fractions are updated in two steps. First the volume-fraction transport equations without the source terms are solved:

$$\frac{\partial \alpha}{\partial t} + \nabla \cdot \alpha \mathbf{u} = 0 \quad , \tag{3.14}$$

$$\frac{\partial \beta}{\partial t} + \nabla \cdot \beta \mathbf{u} = 0 \quad . \tag{3.15}$$

The solutions of Eqs. (3.14) and (3.15) are denoted respectively as $\alpha^*$ and $\beta^*$ which are the intermediate states. Then the compressibility effect represented by the source term is taken into account for the final solution:

$$\alpha^{n+1} = \alpha^* \left[1 + \left(\frac{\overline{K}_S}{K_S^\alpha}\left[1 - (\alpha^* + \beta^*)\right]\right)\right] \quad , \tag{3.16}$$

$$\beta^{n+1} = \beta^* \left[1 + \left(\frac{\overline{K}_S}{K_S^\beta}\left[1 - (\alpha^* + \beta^*)\right]\right)\right] \quad , \tag{3.17}$$

where $\alpha^{n+1}$ and $\beta^{n+1}$ are the volume fractions at the new time step.

The numerical method ensures the relation $\alpha + \beta = 1$ during the evolution of

the volume fractions. As mentioned in section 3.2, instead of solving Eqs. (3.15) and (3.17), $\beta^{n+1}$ can be computed directly from $\alpha^{n+1}$ based on the relation $\alpha + \beta = 1$ which holds for all time steps.

## Anti-diffusion interface sharpening

The anti-diffusion interface-sharpening technique presented in chapter 2 is adopted and extended to two-phase compressible flow equations as described in the previous section. The idea of sharpening the two-fluid interfaces is to provide a correction algorithm which can be applied as post-processing to the volume-fraction field after each time step. For this purpose, an anti-diffusion equation, i.e. a diffusion equation with a positive diffusion coefficient, is solved to counter-act the numerical diffusion in the volume-fraction-transport equation:

$$\frac{\partial \alpha}{\partial \tau} = -\nabla \cdot (D \nabla \alpha) \quad , \tag{3.18}$$

where $D > 0$ is an anti-diffusion coefficient and $\tau$ is a pseudo time.

The essential points in solving the anti-diffusion equation are recapitulated below and the differences from the incompressible formulation are detailed. First, the limited cell-averaged value of the gradient of $\alpha$ is obtained by the regularization based on a minmod limiter - this is hereafter denoted by $\left(\overline{\nabla \alpha}\right)_{lim}$. Then, the anti-diffusion flux for $\alpha$, $F^{\alpha}_{AD}$, at the cell face between cell P and cell N is obtained by:

$$F^{\alpha}_{AD} = \begin{cases} -D \left(\left(\overline{\nabla \alpha}\right)_{lim}\right)_P \cdot \mathbf{S} & \text{if } |\left(\left(\overline{\nabla \alpha}\right)_{lim}\right)_P| \leq |\left(\left(\overline{\nabla \alpha}\right)_{lim}\right)_N| \quad , \\ -D \left(\left(\overline{\nabla \alpha}\right)_{lim}\right)_N \cdot \mathbf{S} & \text{if } |\left(\left(\overline{\nabla \alpha}\right)_{lim}\right)_N| < |\left(\left(\overline{\nabla \alpha}\right)_{lim}\right)_P| \quad , \end{cases} \tag{3.19}$$

where $\left(\left(\overline{\nabla \alpha}\right)_{lim}\right)_P$ and $\left(\left(\overline{\nabla \alpha}\right)_{lim}\right)_N$ are the respective limited cell-averaged value of the gradient in cell P and cell N, $\mathbf{S}$ is the cell face area vector which points from cell P to cell N.

The right-hand-side of Eq. (3.18) is calculated by

$$\overline{\nabla \cdot (-D(\nabla \alpha))} = \frac{\sum_{cf} \left(F^{\alpha}_{AD}\right)}{V} \quad , \tag{3.20}$$

where $\sum_{cf}$ denotes the summation over all cell faces and $V$ is the cell volume.

The volume fraction is advanced in pseudo time by an explicit Euler scheme

$$\alpha^{N+1} = \alpha^{N} + \overline{\nabla \cdot (-D(\nabla \alpha^{N}))} \Delta \tau \quad , \tag{3.21}$$

with $N$ being the pseudo time index, and the time step limit on pseudo time,

$$\Delta\tau = \frac{1}{4}\frac{(\Delta x_{min})^2}{D} \quad , \tag{3.22}$$

where $\Delta x_{min}$ is the minimum cell width.

In the following, $(\cdot)^{AD}$ denotes a quantity that is obtained after applying the sharpening procedure. As proposed in the incompressible simulations, it should be noted that the anti-diffusion equation does not need to be integrated up to a certain pseudo time. Rather a certain number of iterations is performed to achieve a desired interface steepness, which is controlled by a stopping criterion detailed below. While other time-integration schemes can be used for the solution of the anti-diffusion equation, the explicit Euler scheme is employed here for its low computational cost.

As the anti-diffusion equation is meant to counteract the numerical diffusion resulting from the volume-fraction transport, the choice of $D$ is based on an estimation of the numerical diffusion of the underlying numerical scheme. Following the formulation of the HLL Riemann solver, $D$ is chosen to be

$$D = \left| \frac{S_L S_R \left(\alpha_R - \alpha_L\right)}{S_R - S_L} \right| \quad . \tag{3.23}$$

After $\alpha$ has been sharpened, all other flow variables in the governing equations have to be updated to ensure the consistency across the flow variables which is important for simulating the correct flow physics. As demonstrated in [88] where the interface compression technique is applied, in case only the interface function is compressed without updating the other flow variables, the mismatch of the compressed interface function and the smeared density field leads to an incorrect interface evolution. To update the other flow variables the authors in [88] employ a hyperbolic function together with their interface compression technique for the mass conservation equation to localize the compression to the interface region. For the momentum and energy field, they first compute the primitive variables before applying the interface compression technique, and based on these primitive variables and the compressed interface function they estimate the new conserved variables. It is noted that based on this approach the compression in the interface function equation and in the mass conservation equation is not exactly consistent, and the update of the momentum and energy field is not conservative. Alternatively in this work, all the flow variables are updated according to $\alpha^{AD}$ for ensuring the consistency. For each time the $\alpha$ field is sharpened by solving an anti-diffusion equation, the other flow variables $\beta$, $\alpha\rho^{\alpha}$, $\beta\rho^{\beta}$, $\rho\mathbf{u}$, $\rho E$ are updated accordingly by respective flux defined based on $F^{\alpha}_{AD}$. These fluxes

to update the other variables are denoted by $F_{AD}^{\beta}$, $F_{AD}^{\alpha\rho^{\alpha}}$, $F_{AD}^{\beta\rho^{\beta}}$, $F_{AD}^{\rho\mathbf{u}}$, $F_{AD}^{\rho E}$, respectively for the flow variables $\beta$, $\alpha\rho^{\alpha}$, $\beta\rho^{\beta}$, $\rho\mathbf{u}$, $\rho E$.

To preserve the relation $\alpha + \beta = 1$, $F_{AD}^{\beta}$ is defined as

$$F_{AD}^{\beta} = -F_{AD}^{\alpha} \quad . \tag{3.24}$$

$F_{AD}^{\alpha\rho^{\alpha}}$, $F_{AD}^{\beta\rho^{\beta}}$ are defined based on $F_{AD}^{\alpha}$ and $F_{AD}^{\beta}$, and the flow variables $\alpha$, $\beta$, $\alpha\rho^{\alpha}$, $\beta\rho^{\beta}$ interpolated at the cell face:

$$F_{AD}^{\alpha\rho^{\alpha}} = F_{AD}^{\alpha}\rho_f^{\alpha} \quad , \tag{3.25}$$

$$F_{AD}^{\beta\rho^{\beta}} = -F_{AD}^{\alpha}\rho_f^{\beta} \quad , \tag{3.26}$$

$$\rho_f^{\alpha} = \frac{(\alpha\rho^{\alpha})_f}{\alpha_f} \quad , \quad \rho_f^{\beta} = \frac{\left(\beta\rho^{\beta}\right)_f}{\beta_f} \quad , \tag{3.27}$$

$$(\cdot)_f = \frac{(\cdot)_P d_N + (\cdot)_N d_P}{d_P + d_N} \quad , \tag{3.28}$$

where $(\cdot)_P$ and $(\cdot)_N$ are the cell-averaged variables in cell P and N, $d_P$ and $d_N$ are the distances from the cell centers P and N to the respective cell-face centers, and $(\cdot)_f$ denotes the reconstruction at the cell face of the variables.

$F_{AD}^{\rho\mathbf{u}}$ is defined based on $F_{AD}^{\alpha\rho^{\alpha}}$, $F_{AD}^{\beta\rho^{\beta}}$, and the flow variables $\alpha\rho^{\alpha}$, $\beta\rho^{\beta}$, $\rho\mathbf{u}$ interpolated at the cell face:

$$F_{AD}^{\rho\mathbf{u}} = \left(F_{AD}^{\alpha\rho^{\alpha}} + F_{AD}^{\beta\rho^{\beta}}\right) \frac{(\rho\mathbf{u})_f}{(\alpha\rho^{\alpha})_f + (\beta\rho^{\beta})_f} \quad , \tag{3.29}$$

which can be rewritten as

$$F_{AD}^{\rho\mathbf{u}} = F_{AD}^{\alpha}\left(\rho_f^{\alpha} - \rho_f^{\beta}\right) \frac{(\rho\mathbf{u})_f}{(\alpha\rho^{\alpha})_f + (\beta\rho^{\beta})_f} \quad . \tag{3.30}$$

$F_{AD}^{\rho E}$ is defined based on the assumption of pressure equilibrium. Given the phase EOS based on Eq. (3.9)

$$p^{\alpha} = \Gamma^{\alpha}(\rho e)^{\alpha} + f^{\alpha} \quad , \tag{3.31}$$

$$p^{\beta} = \Gamma^{\beta}(\rho e)^{\beta} + f^{\beta} \quad , \tag{3.32}$$

and the pressure-equilibrium EOS Eq. (3.10),

$$p = \frac{\rho e + \left(\frac{\alpha f^{\alpha}}{\Gamma^{\alpha}} + \frac{\beta f^{\beta}}{\Gamma^{\beta}}\right)}{\left(\frac{\alpha}{\Gamma^{\alpha}} + \frac{\beta}{\Gamma^{\beta}}\right)} \quad , \tag{3.33}$$

$F_{AD}^{\rho E}$ is obtained by imposing $p^\alpha = p = p^\beta$:

$$F_{AD}^{\rho E} = F_{AD}^{\alpha} \left[ \left( \Gamma \left( \rho e \right) \right)_f + f_f + \left( \rho E_k \right)_f \right] \quad , \tag{3.34}$$

$$\left( \Gamma \left( \rho e \right) \right)_f = \left( \frac{\Gamma_f^\beta - \Gamma_f^\alpha}{\alpha_f \Gamma_f^\beta + \beta_f \Gamma_f^\alpha} \right) \left( \left( \rho E \right)_f - \frac{\frac{1}{2} \left| \left( \rho \mathbf{u} \right)_f \right|^2}{\left( \alpha \rho^\alpha \right)_f + \left( \beta \rho^\beta \right)_f} \right) \quad , \tag{3.35}$$

$$f_f = \left( \frac{f_f^\beta - f_f^\alpha}{\alpha_f \Gamma_f^\beta + \beta_f \Gamma_f^\alpha} \right) \quad , \tag{3.36}$$

$$\left( \rho E_k \right)_f = \left( \frac{\frac{\left( \alpha \rho^\alpha \right)_f}{\alpha_f} - \frac{\left( \beta \rho^\beta \right)_f}{\beta_f}}{\left( \alpha \rho^\alpha \right)_f + \left( \beta \rho^\beta \right)_f} \right) \left( \frac{\frac{1}{2} \left| \left( \rho \mathbf{u} \right)_f \right|^2}{\left( \alpha \rho^\alpha \right)_f + \left( \beta \rho^\beta \right)_f} \right) \quad . \tag{3.37}$$

For cases with the ideal-gas EOS it is $f_f = 0$. It can be seen that $F_{AD}^{\beta}$, $F_{AD}^{\alpha\rho^\alpha}$, $F_{AD}^{\beta\rho^\beta}$, $F_{AD}^{\rho\mathbf{u}}$, $F_{AD}^{\rho E}$ are all defined based on $F_{AD}^{\alpha}$ and the flow variables interpolated at the cell face. Note that, as the relation $\alpha + \beta = 1$ always holds, $F_{AD}^{\beta}$ can be calculated first instead of $F_{AD}^{\alpha}$, and $F_{AD}^{\alpha}$, $F_{AD}^{\alpha\rho^\alpha}$, $F_{AD}^{\beta\rho^\beta}$, $F_{AD}^{\rho\mathbf{u}}$, $F_{AD}^{\rho E}$ can be calculated based on $F_{AD}^{\beta}$ in a similar fashion as illustrated above. Both solution procedures give the same set of anti-diffusion sharpening flux since $\overline{\nabla \alpha} = -\overline{\nabla \beta}$.

The variables $\beta$, $\alpha\rho^\alpha$, $\beta\rho^\beta$, $\rho\mathbf{u}$, $\rho E$ are then updated in the same way as $\alpha$ according to Eqs. (3.20) and (3.21) based on the above $F_{AD}^{\beta}$, $F_{AD}^{\alpha\rho^\alpha}$, $F_{AD}^{\beta\rho^\beta}$, $F_{AD}^{\rho\mathbf{u}}$, $F_{AD}^{\rho E}$ with the same pseudo time step. It should be noted that the formulation of the anti-diffusion sharpening flux for phase mass, momentum and energy is conservative.

The anti-diffusion equation can be solved repeatedly to attain an even sharper profile. A case- and grid- independent stopping criterion (i.e. no explicit dependence on fluid or geometry parameter and no explicit dependence on cell-size measurement) based on the measurement of the tolerance of the interface sharpness, $TOL$, as developed in the chapter 2 is employed to terminate the sharpening iterations:

$$TOL = \frac{\sum_i \left| \left( \overline{\nabla \cdot \left( \overline{\nabla \alpha} \right)_{lim}} \right)_i \right| V_i}{\sum_i | \left( \left( \overline{\nabla \alpha} \right)_{CD} \right)_i |^2 V_i} \quad , \tag{3.38}$$

where $\sum_i$ denotes the summation over all cells, the subscript $i$ indicates the cell index, and $V_i$ is the volume of the cell $i$. One can see that $TOL$ essentially compares the two gradients of the volume-fraction field: $\left( \overline{\nabla \alpha} \right)_{lim}$ which is the limited gradient obtained in the solution of the anti-diffusion equation, and $\left( \overline{\nabla \alpha} \right)_{CD}$ which is the gradient

calculated by a central difference scheme. As the interface becomes sharper after each time the anti-diffusion equation is solved, the right-hand-side of Eq. (3.38) decreases. Numerical experiments show that $TOL = 1$ is a suitable threshold for the anti-diffusion interface sharpening to stop for all cases considered in this work. It is noted that the choice of $TOL = 1$ is also adopted in the incompressible simulations in chapter 2. Numerical experiments also show that the interface-sharpness is not sensitive to the choice of $TOL$ - the interface sharpness does not vary much for $TOL$ around 1. Too small a $TOL$, however, would sharpen the interface beyond the resolution limit of the underlying scheme and could introduce numerical instabilities. Typically, only 1-2 sharpening iterations are sufficient at each time step. Based on the test cases in sections 3.4, the computational overhead of the interface-sharpening is found to be $5 - 10\%$.

## Overall solution procedure

The solution algorithm of the two-phase compressible flow with the anti-diffusion interface sharpening for $\mathbf{U} = \left(\alpha, \beta, \alpha\rho^{\alpha}, \beta\rho^{\beta}, \rho\mathbf{u}, \rho E\right)$ from time step $n$ to $n+1$ can be summarized as follows:

1. Solve Eqs. (3.14), (3.15), (3.3), (3.4), (3.5), (3.6) based on the flux calculated by the HLL Riemann solver for $\left(\alpha^{*}, \beta^{*}, \left(\alpha\rho^{\alpha}\right)^{n+1'}, \left(\beta\rho^{\beta}\right)^{n+1'}, \left(\rho\mathbf{u}\right)^{n+1'}, \left(\rho E\right)^{n+1'}\right)$ where $(\cdot)^{n+1'}$ indicates the variable at time step $n+1$ without interface sharpening.

2. Solve Eqs. (3.16) and (3.17) for $\left(\alpha^{n+1'}, \beta^{n+1'}\right)$.
   $\left(\alpha^{n+1'}, \beta^{n+1'}, \left(\alpha\rho^{\alpha}\right)^{n+1'}, \left(\beta\rho^{\beta}\right)^{n+1'}, \left(\rho\mathbf{u}\right)^{n+1'}, \left(\rho E\right)^{n+1'}\right)$ obtained here is the base solution of the flow variables without interface sharpening at time step $n+1$.

3. Solve Eqs. (3.18) to (3.21) for $\alpha^{AD}$. After each time $\alpha^{AD}$ is found, $\beta^{AD}$, $\left(\alpha\rho^{\alpha}\right)^{AD}$, $\left(\beta\rho^{\beta}\right)^{AD}$, $\left(\rho\mathbf{u}\right)^{AD}$, $\left(\rho E\right)^{AD}$ are computed accordingly, calculated from the fluxes in Eqs. (3.24), (3.25), (3.26), (3.30) and (3.34).

4. The anti-diffusion sharpening (Step 3.) is iterated until the stopping criterion of $TOL \leq 1$ based on Eq. (3.38) is satisfied.
   The result of step 3 $\left(\alpha^{AD}, \beta^{AD}, \left(\alpha\rho^{\alpha}\right)^{AD}, \left(\beta\rho^{\beta}\right)^{AD}, \left(\rho\mathbf{u}\right)^{AD}, \left(\rho E\right)^{AD}\right)$ is taken as the final solution
   $\left(\alpha^{n+1}, \beta^{n+1}, \left(\alpha\rho^{\alpha}\right)^{n+1}, \left(\beta\rho^{\beta}\right)^{n+1}, \left(\rho\mathbf{u}\right)^{n+1}, \left(\rho E\right)^{n+1}\right)$ at time step $n+1$.

## 3.4 Numerical results

First, a 1-dimensional air-helium shock-tube problem and a 1-dimensional molybdenum-MORB shock-contact problem are considered to verify the interface sharpening method with the ideal-gas EOS and the Mie-Grüneisen EOS respectively. Then, 2-dimensional shock-bubble interactions based on the experiments of [26], and a 2-dimensional shock-contact problem are considered to verify the interface sharpening method in multiple-dimensions, and to illustrate the small-scale interface structures recovered by the interface sharpening method.

For all cases in this section the reconstruction of $\mathbf{U}_L$ and $\mathbf{U}_R$ is based on the van Leer MUSCL scheme [112]. A third-order TVD Runge-Kutta method is employed for the time integration. The time step for the governing equations is determined by the CFL requirement with a CFL number of 0.2. The zero fraction of one phase in another pure phase is represented as $10^{-6}$ at the initialization of simulations.

### Shock-tube problem

The one-dimensional air-helium shock tube case of [33] is considered. The domain is defined as $[0, 1]$ and discretized by 200 cells. The ideal-gas EOS is employed for the two phases and the initial condition is

$$(\rho, \mathbf{u}, p, \gamma) = \begin{cases} (1, 0, 1, 1.4) & \text{if } 0 \leq x < 0.5 \\ (0.125, 0, 0.1, 1.667) & \text{else} \end{cases} . \tag{3.39}$$

The results with and without the application of the anti-diffusion interface sharpening technique at $t = 0.15$ are shown in Fig. 3.1. The results at higher grid resolutions, 400 cells and 800 cells, are shown in the Fig. 3.2.

First, the flow variables in all cases agree well with the exact solution. By comparing the results with and without the interface sharpening, one can see that the phase interface is better resolved, as represented by the reduced number of transition points in $\alpha$, with the application of the anti-diffusion interface sharpening technique. Then by comparing the results with the interface sharpening at different grid resolutions, the interface is resolved by a similar number of grid points in the vicinity of the position of volume fraction 0.5, which demonstrates the interface sharpness controlled by the grid-independent stopping criterion Eq. (3.38). It should also be noted that the improved interface resolution also transfers to the other variables at the two-phase interface.

In order to study and compare the order of truncation error of the two-phase

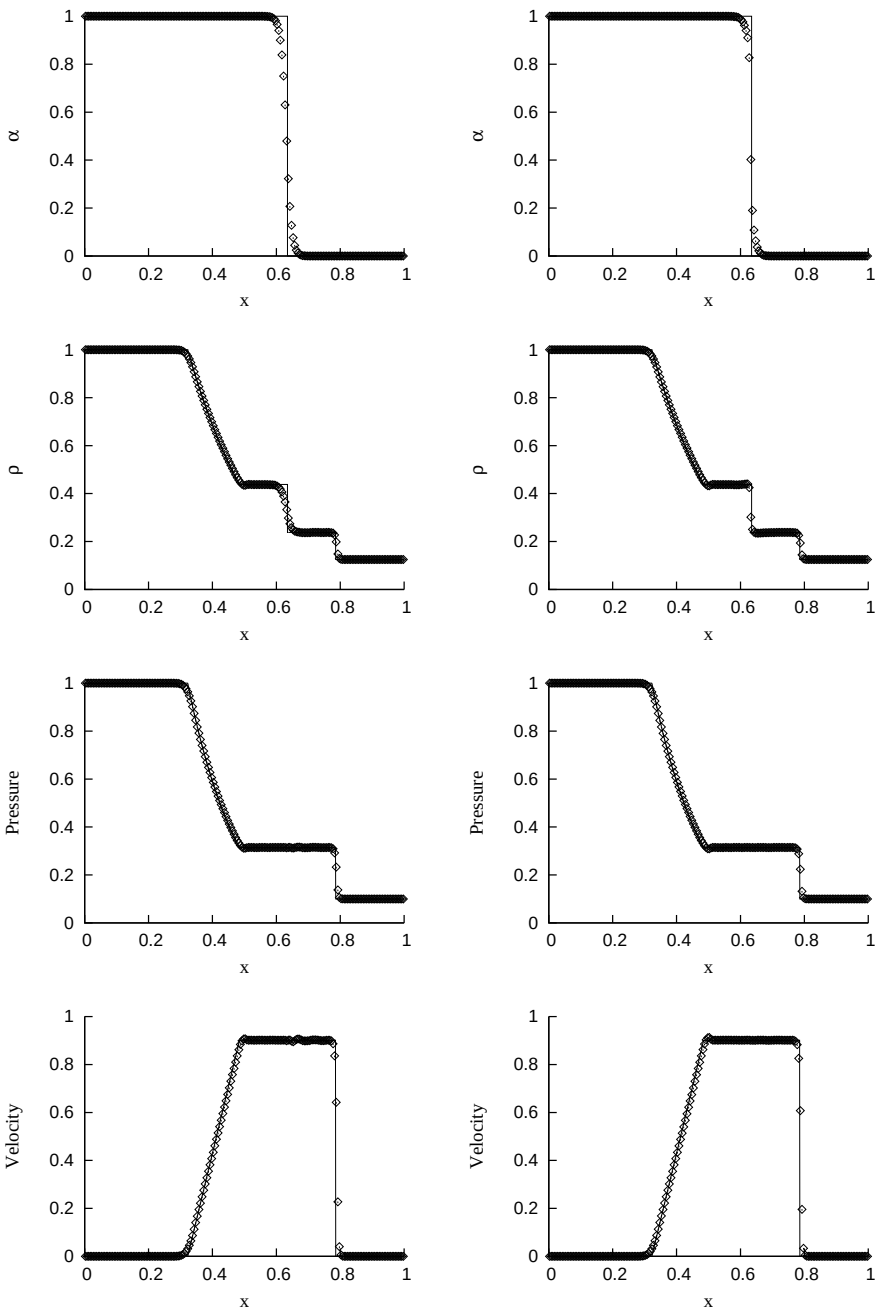


Figure 3.1: Variables at $t = 0.15$ of the air-helium shock tube. Numerical results at the grid resolution of 200 cells. Symbols are the numerical results and solid lines are the exact solutions. Left column: no interface sharpening; right column: with interface sharpening.

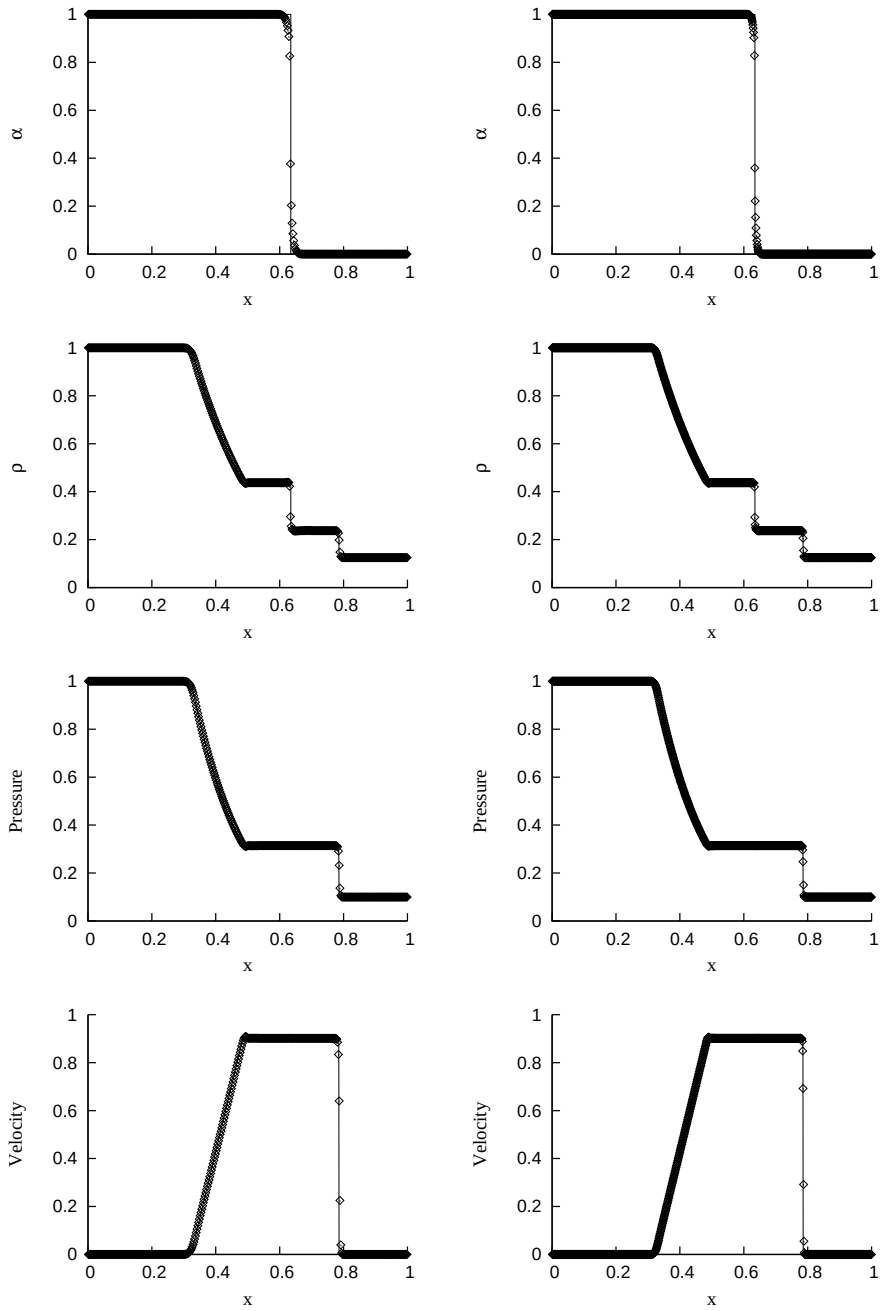


Figure 3.2: Variables at $t = 0.15$ of the air-helium shock tube. Numerical results with interface sharpening. Symbols are the numerical results and solid lines are the exact solutions. Left column: grid resolution of 400 cells; right column: grid resolution of 800 cells.

interface evolution with and without the application of the interface-sharpening technique, the $L_1$ errors and the orders of the truncation error of the volume-fraction field at $t = 0.15$ are calculated and shown in Table. 3.1. The analysis indicates an error of $\mathcal{O}(\Delta x)$ for both computations with and without the application of the anti-diffusion interface-sharpening technique, and the $L_1$ error is reduced when the interface-sharpening technique is applied.

| | no interface sharpening | | with interface sharpening | |
|---|---|---|---|---|
| Grid resolution | $L_1$ error | Error order | $L_1$ error | Error order |
| 100 cells | 0.02113 | | 0.01571 | |
| 200 cells | 0.01183 | 0.84 | 0.00729 | 1.11 |
| 400 cells | 0.00732 | 0.69 | 0.00418 | 0.80 |
| 800 cells | 0.00456 | 0.68 | 0.00244 | 0.78 |

Table 3.1: $L_1$ errors and orders of the truncation error at $t = 0.15$ for the air-helium shock tube.

The exact conservation (to the 64-bit machine double precision) of the conservative variables is shown in the Table. 3.2 for the computation at the grid-resolution of 200 cells.

| | no interface sharpening | with interface sharpening |
|---|---|---|
| $\sum(\alpha\rho^\alpha)_{initialized} - \sum(\alpha\rho^\alpha)_{final}$ | -7.10543e-14 | -2.84217e-14 |
| $\sum(\beta\rho^\beta)_{initialized} - \sum(\beta\rho^\beta)_{final}$ | -1.59872e-14 | -1.59872e-14 |
| $\sum(\rho E)_{initialized} - \sum(\rho E)_{final}$ | -2.27374e-13 | -5.68434e-14 |

Table 3.2: Exact conservation (to the 64-bit machine double precision) for the air-helium shock tube at the grid resolution of 200 cells. $\sum(\cdot)$ denotes the summation of the variable over the entire computational domain. The subscripts *initialized* and $final$ denote respectively the initialized state and the final state.

## 1-dimensional shock-contact problem

The interaction of a shock wave in molybdenum and an encapsulated MORB (Mid-Ocean Ridge Basalt) liquid of [55, 90, 89, 33] in a 2-dimensional setting is first considered as a 1-dimensional case. The Mie-Grüneisen EOS is employed for the two materials with coefficients

$$(\rho_0, c_0, s, \Gamma_0) = \begin{cases} (9.961, 4.77, 1.43, 2.56) & \text{for molybdenum} \\ (2.66, 2.1, 1.68, 1.18) & \text{for MORB liquid} \end{cases}. \tag{3.40}$$

The domain is defined as $[0, 1]$ and discretized by 200 cells. The shock is initialized at position 0.4 and the two-phase interface at position 0.6, where the initial condition

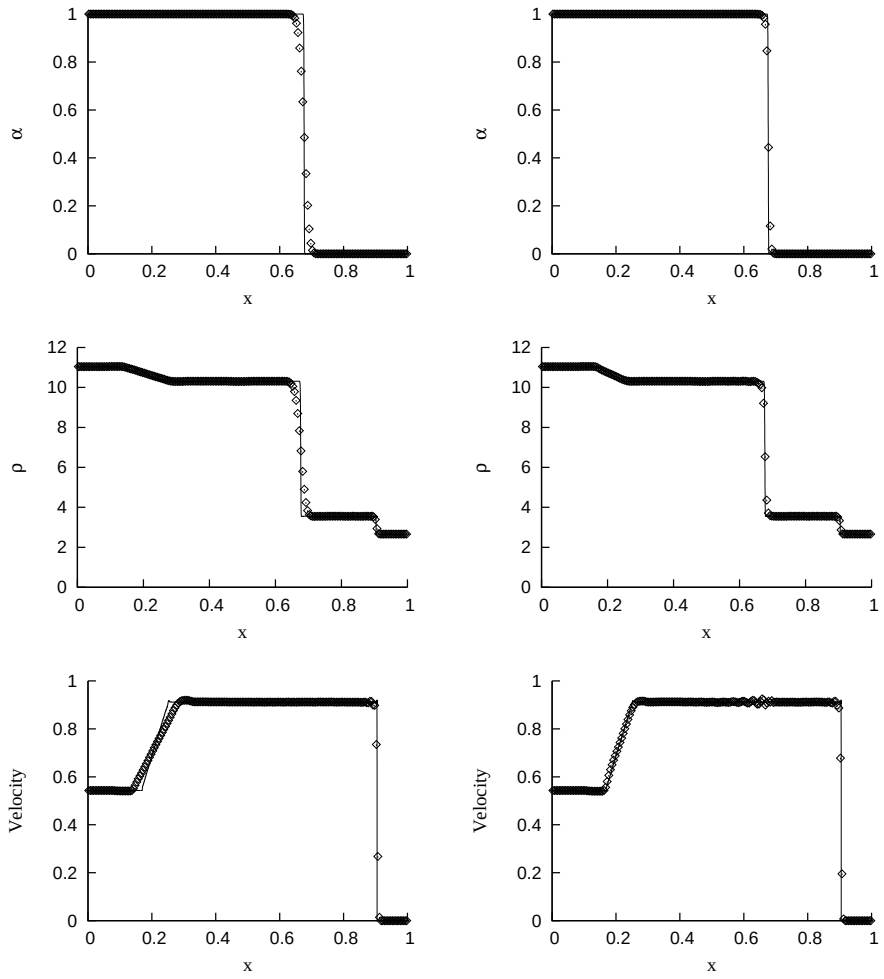


Figure 3.3: Variables at $t = 0.12$ of the 1D shock-contact problem. Numerical results at the grid resolution of 200 cells. Symbols are the numerical results and solid lines are the reference solutions. Left: no interface sharpening; right: with interface sharpening.

is

$$(\rho, \mathbf{u}, p) = \begin{cases} (11.042, 0.543, 30) & \text{if } 0 \leq x < 0.4 \\ (9.961, 0, 0) & \text{if } 0.4 \leq x < 0.6 \\ (2.66, 0, 0) & \text{else} \end{cases} . \tag{3.41}$$

The results with and without the application of the anti-diffusion interface sharpening technique at $t = 0.12$ are shown in Fig. 3.3. The results at grid resolutions of 400 cells and 800 cells are shown in Fig. 3.4.

All flow variables in all cases agree well with the reference solutions and literature. As in the test case of the ideal-gas EOS, the phase interface is better resolved and the flow variables are consistent with the application of the anti-diffusion interface sharpening technique. The interface is resolved by a similar number of grid points

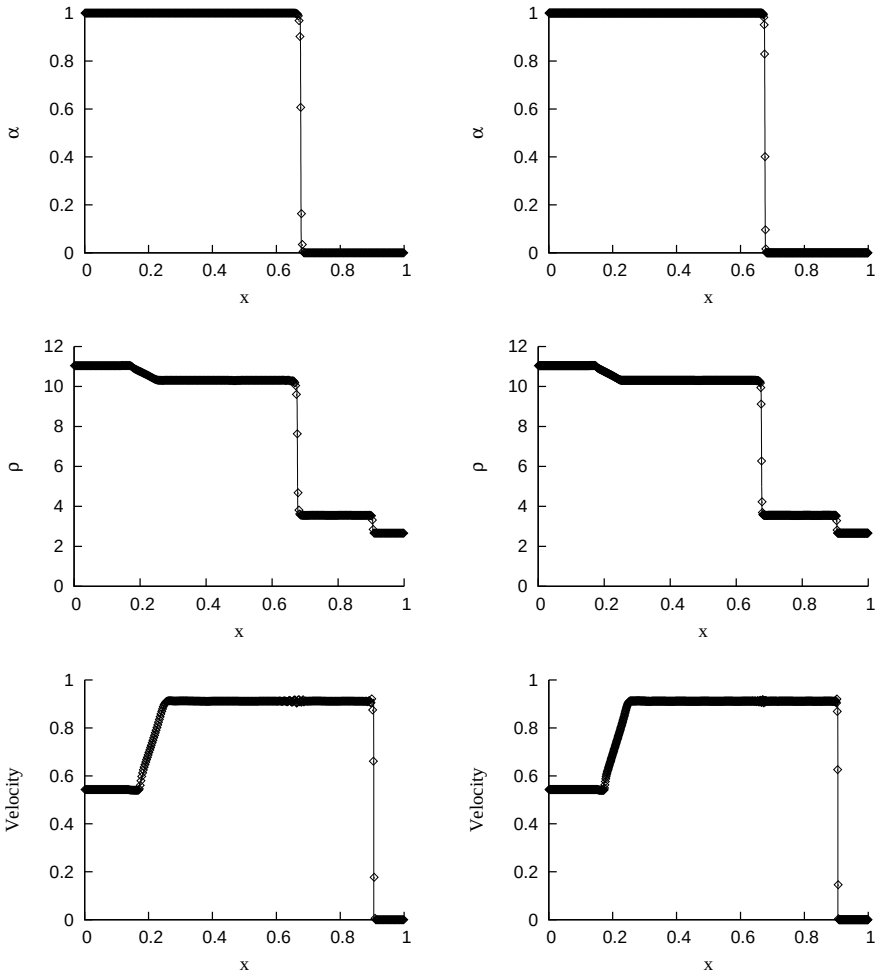


Figure 3.4: Variables at $t = 0.12$ of the 1D shock-contact problem. Numerical results with interface sharpening. Symbols are the numerical results and solid lines are the reference solutions. Left column: grid resolution of 400 cells; right column: grid resolution of 800 cells.

in the vicinity of the position of volume fraction 0.5 at different grid resolutions as found in the previous test case, which demonstrates the independence of the interface-sharpening stopping criterion on the grid resolution and the case.

## 2-dimensional air-R22 shock-bubble interaction

The experimental case of a R22 cylinder in air hit by a shock wave at Mach number of 1.22 of [26] is considered to demonstrate the improvement by the interface sharpening and the recovery of the small-scale interface structures by the interface sharpening method. Results of the case have been given in a number of references employing interface capturing methods [69, 61, 5, 18, 45, 58, 79, 86]. Corresponding to the reference literature, the configuration is considered as 2-dimensional, and the set-up of [86] and the fluid parameters of [69] are adopted here. Flow field symmetry about the streamwise center axis is assumed, and thus only the top half domain is computed. A zero-gradient boundary condition is imposed at the left and right boundaries, and the symmetry-plane boundary condition is imposed at the top and bottom boundaries. The case is computed on three levels of grid resolution in order to highlight the consistent recovery of small-scale structures as the grid resolution increases. The domain is discretized by Cartesian grids with size $\Delta x/D = \Delta y/D = 0.01$, $\Delta x/D = \Delta y/D = 0.005$ and $\Delta x/D = \Delta y/D = 0.0025$, where $\Delta x, \Delta y, D$ are the cell sizes in x-direction and y-direction, and the bubble initial diameter. These grid sizes correspond to grid-resolutions of 100, 200 and 400 cells across the bubble initial diameter. Schlieren-type images, $|\nabla\rho|$, at time instants corresponding to the experimental images [26], i.e. $t = 55\mu s,\ 115\mu s,\ 135\mu s,\ 187\mu s,\ 247\mu s,\ 318\mu s,\ 342\mu s,\ 417\mu s$ after the shock impact, are shown in Figs. 3.5 and 3.6. The enlarged images at the grid-resolution of 400 cells across the bubble initial diameter at $t = 247\mu s,\ 318\mu s,\ 342\mu s,\ 417\mu s$ after the shock impact are shown in Figs. 3.7. The positions of the characteristic interface points and waves are recorded against time corresponding to [26, 90, 44] and shown in Fig. 3.8.

First, for the results without the application of anti-diffusion interface-sharpening, the large-scale structures and interface evolution agree well with the reference literature which confirms the validity of the underlying governing equations and numerical method. Second, with the application of interface-sharpening, the phase interface becomes significantly better resolved while the large-scale structures remain consistent with the reference solution where no sharpening is applied and with the reference literature. The comparison between the results with and without interface-sharpening shows that more small-scale structures are recovered by the sharpening technique.

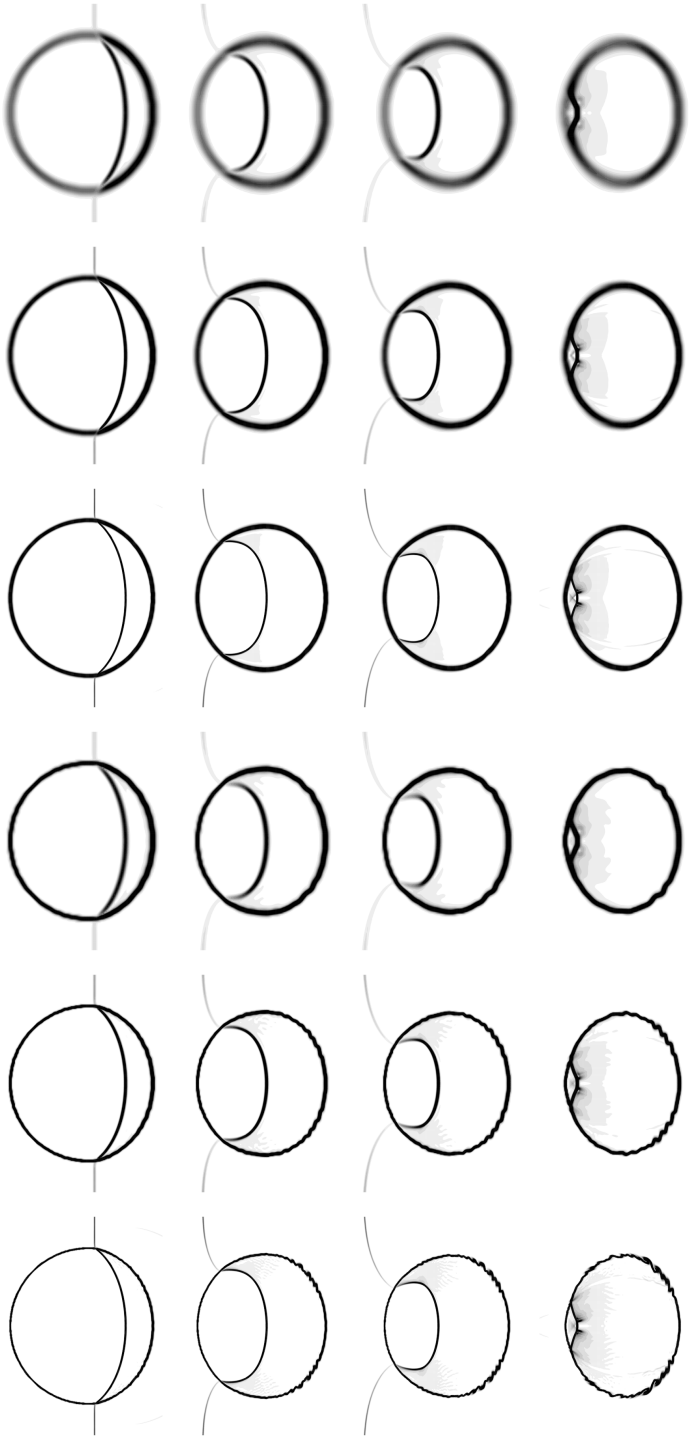

Figure 3.5: Schlieren-type images, $|\nabla\rho|$, of the air-R22 shock-bubble interaction. Top 3 rows: numerical results without interface sharpening; bottom 3 rows: numerical results with interface sharpening. From top to bottom in each set: $\Delta x/D = \Delta y/D = 0.01,\ \Delta x/D = \Delta y/D = 0.005,\ \Delta x/D = \Delta y/D = 0.0025$. From left to right: $t = 55\mu s,\ 115\mu s,\ 135\mu s,\ 187\mu s$ after the shock impact.

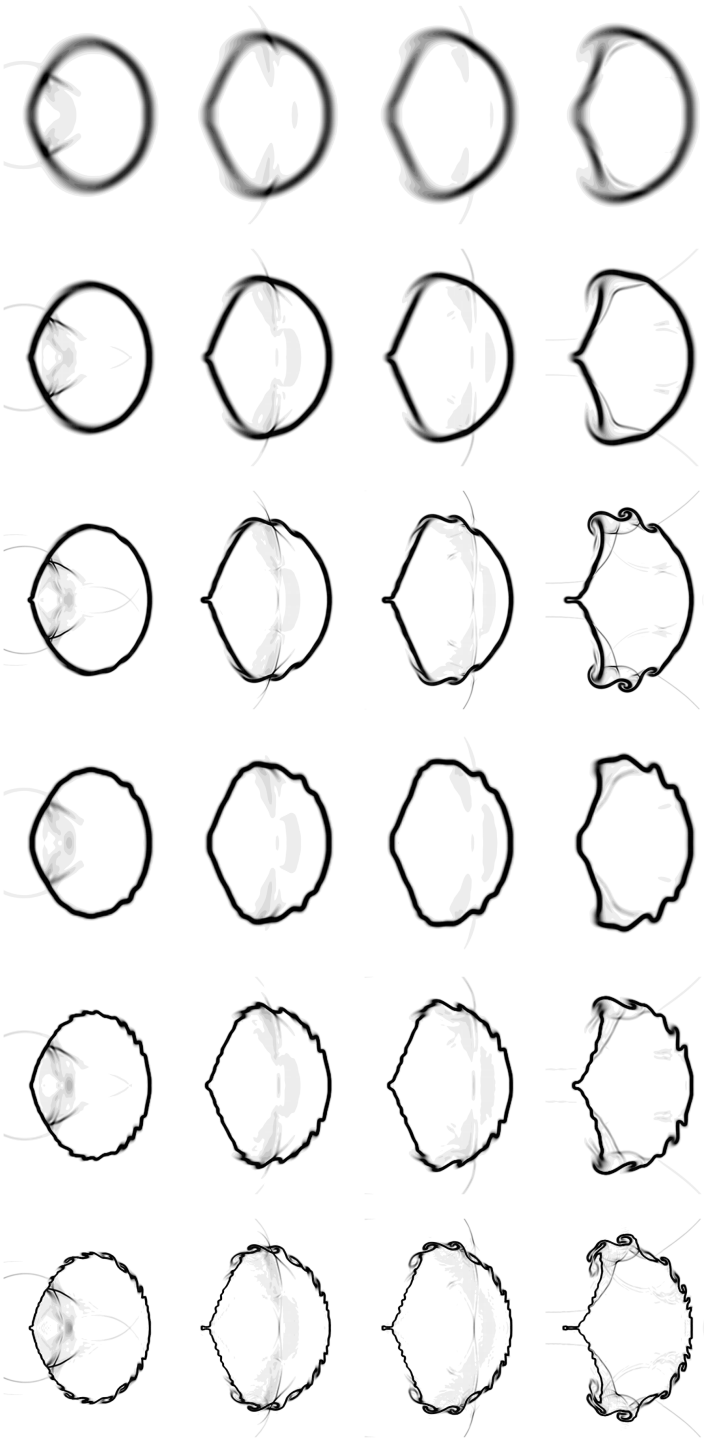

Figure 3.6: Schlieren-type images, $|\nabla\rho|$, of the air-R22 shock-bubble interaction. Top 3 rows: numerical results without interface sharpening; bottom 3 rows: numerical results with interface sharpening. From top to bottom in each set: $\Delta x/D = \Delta y/D = 0.01,\ \Delta x/D = \Delta y/D = 0.005,\ \Delta x/D = \Delta y/D = 0.0025$. From left to right: $t = 247\mu s,\ 318\mu s,\ 342\mu s,\ 417\mu s$ after the shock impact.

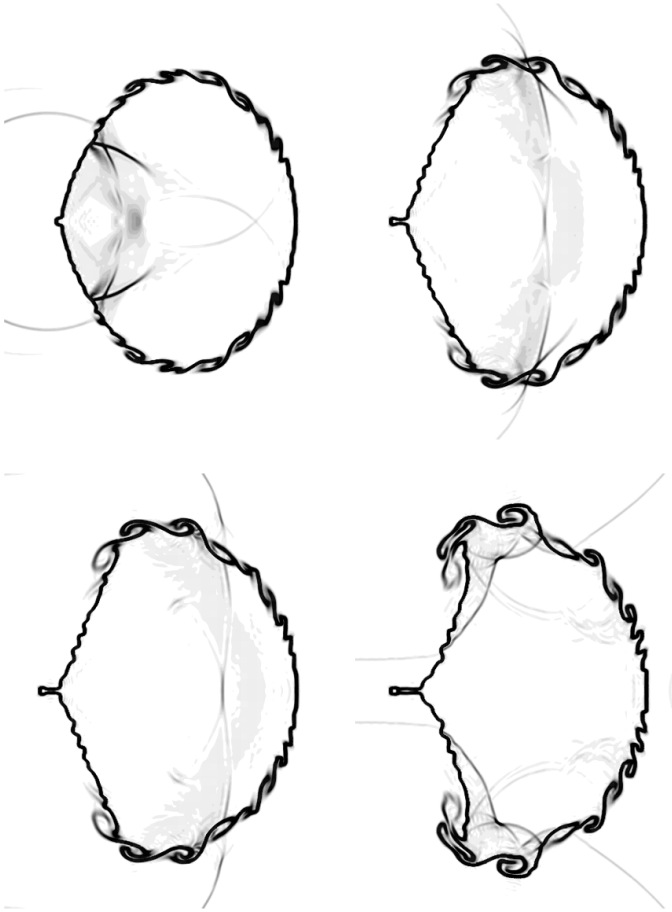

Figure 3.7: Schlieren-type images, $|\nabla\rho|$, of the air-R22 shock-bubble interaction, with interface sharpening, at the grid-resolution of $\Delta x/D = \Delta y/D = 0.0025$. From left to right, top to bottom: $t = 247\mu s,\ 318\mu s,\ 342\mu s,\ 417\mu s$ after the shock impact.

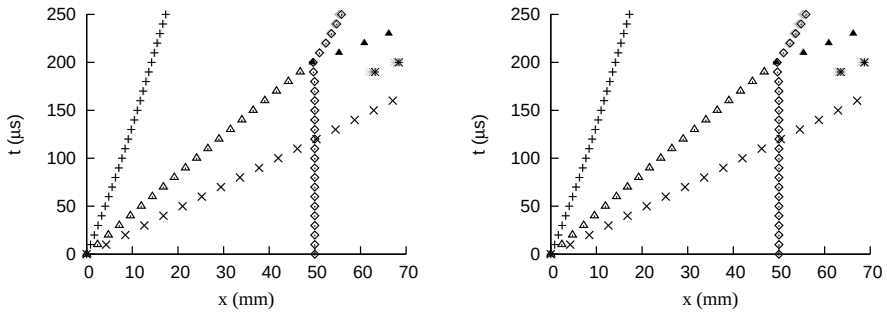


Figure 3.8: Space-time diagram for the characteristic interface points and waves of the air-R22 shock-bubble interaction: '+' denotes the upstream interface, '$\diamond$' denotes the downstream interface, '$\times$' denotes incident shock, '$\triangle$' denotes the refracted shock, '$\blacktriangle$' and '$*$' denote transmitted shocks. Symbols of light grey color denote $\Delta x/D = \Delta y/D = 0.01$, symbols of dark grey color denote $\Delta x/D = \Delta y/D = 0.005$, symbols of black color denote $\Delta x/D = \Delta y/D = 0.0025$. Left: no interface sharpening; right: with interface sharpening.

As compared to reference results obtained by adaptive mesh refinement (AMR) algorithms using interface-capturing methods [69, 61, 5, 79] where the effective grid resolution is approximately 800 to 900 cells across the bubble initial diameter, the interface evolution obtained by the present method agrees well with respect to prominent features of the interface roll-up present in these reference results. The present results also agree well with reference results computed by a VOF interface-tracking method [90] at a grid resolution of 400 cells across the bubble initial diameter. The interface instability first develops at the interface near the upper side in the bubble windward direction at $t = 115\mu s$ after the passage of the shock, and the interface rolls up at the windward side from $t = 247\mu s$ after the shock impact onwards. The interface evolutions at $t = 318\mu s,\ 342\mu s,\ 417\mu s$ after the shock impact clearly shows that the Kelvin-Helmholtz instability is recovered by the anti-diffusion interface-sharpening method. In particular, when the present results at grid resolution $\Delta x/D = \Delta y/D = 0.005$ are compared with the reference high grid-resolution results [69, 61, 5, 79], it can be observed that a similar interface evolution can already be recovered by the simulations with the interface sharpening on a mesh which is about 16 times coarser at the interface. One can note that the simulation of the same case in [44] computed by an anti-diffusive numerical scheme which is based on a limited downwind strategy, the interface roll-up is not recovered even for a grid with approximately 562 cells across the bubble initial diameter.

Third, the comparison of the numerical results at different grid resolutions shows the consistent development of the small-scale interface structures recovered by the interface-sharpening method. This is best illustrated by a comparison of numerical results at $t = 247\mu,\ 318\mu s,\ 342\mu s$ after the shock impact: as the grid resolution increases from $\Delta x/D = \Delta y/D = 0.01$ to $\Delta x/D = \Delta y/D = 0.005$, more small-scale interface structures are recovered; when the grid resolution further increases to $\Delta x/D = \Delta y/D = 0.0025$, even finer small-scale interface structures and fine details are recovered. While no pointwise convergence for the numerical solution of the compressible Euler equations as an initial-value problem can be expected as suggested in [81], the interface evolution with the application of the interface-sharpening technique is resolved in a consistent manner with increased recovery of small-scale structures as the grid resolution increases.

## 2-dimensional air-helium shock-bubble interaction

Another experimental case of [26] where a helium cylinder in air hit by a shock wave at Mach number of 1.22 is considered. The case has been simulated by [69, 2, 39, 5,

104, 86, 28, 118]. While most of the results from the reference literature agree on the early-time evolution of large-scale structures, differences are observed for the evolution of small-scale structures at late times. Here mainly the early-time bubble evolution is studied and the numerical results are compared with a high grid-resolution numerical result of [28] which is based on a wavelet-adaptive grid method that reaches an effective grid resolution of approximately 1638 cells across the bubble initial diameter and uses a fifth-order WENO scheme. The numerical results are presented using a non-dimensional time $\tilde{t}$, which is the same as in [28] and given by $\tilde{t} = (t - t_{impact} M c_s / r)$ where $t,\ t_{impact},\ M,\ c_s,\ r$ are the physical time, the physical time at the shock impact, the Mach number of the shock, the sound speed of the surrounding air and the bubble initial radius, respectively.

As only the early-time evolution is considered, the domain size used in section 3.4 is reduced in the streamwise direction and resized to $[80mm, -30mm]$ centered at the bubble center for reducing the computational effort. The same boundary conditions as those in the section 3.4 and the fluid parameters of [86] are adopted. The case is computed at three levels of grid resolution, with grid sizes $\Delta x/D = \Delta y/D = 0.005$, $\Delta x/D = \Delta y/D = 0.0025$ and $\Delta x/D = \Delta y/D = 0.00125$, which correspond to resolutions of 200, 400 and 800 cells across the bubble initial diameter. The density and the vorticity fields at $\tilde{t} = 0.5,\ 1.0,\ 2.0,\ 4.0$ are shown in Fig. 3.9. The enlarged images at the grid resolution of 800 cells across the bubble initial diameter at $\tilde{t} = 2.0,\ 4.0$ are shown in Fig. 3.10. The positions of the characteristic interface points are recorded against time corresponding to [28] and shown in Fig. 3.11.

Similar findings as in the section 3.4 also apply to this test case:

- For the numerical results without the anti-diffusion interface-sharpening method the large-scale structures agree with the reference literature [28], which confirms the validity of the underlying governing equations and numerical method.

- For the numerical results with application of the interface-sharpening method the interface is better resolved, and the large-scale evolution agrees with the results without interface-sharpening and the reference literature [28].

- Finer small-scale interface structures are recovered by the interface-sharpening method. Increasingly small-scale interface structures are recovered in a consistent manner as the grid resolution increases.

As compared to the high-resolution results of [28], the mushroom-shaped structures due to Richtmyer-Meshkov instability [13] are recovered reliably in the numerical results with the interface-sharpening method for the grid $\Delta x/D = \Delta y/D = 0.00125$.

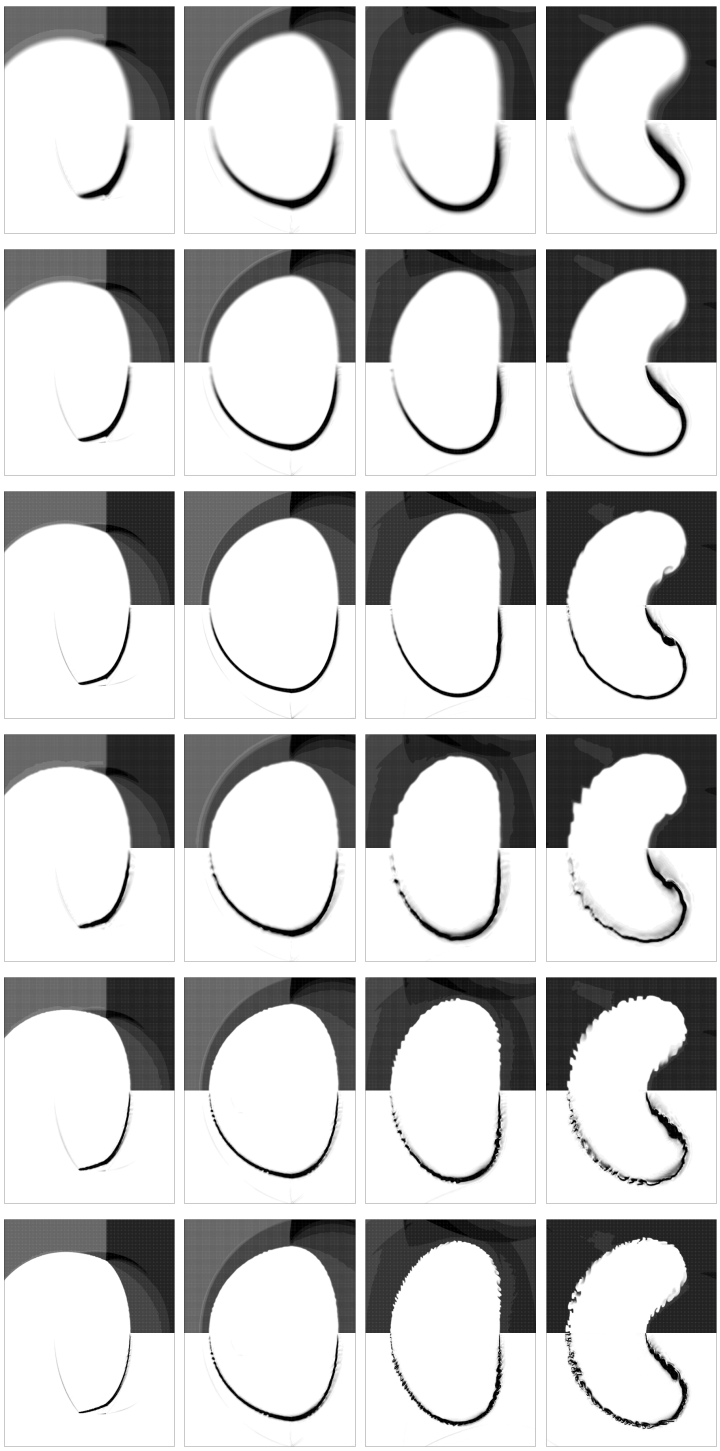

Figure 3.9: Density (upper half) and vorticity (lower half) fields of the air-helium shock-bubble interaction. Top 3 rows: numerical results without interface sharpening; bottom 3 rows: numerical results with interface sharpening. From top to bottom in each set: $\Delta x/D = \Delta y/D = 0.005,\ \Delta x/D = \Delta y/D = 0.0025,\ \Delta x/D = \Delta y/D = 0.00125$. From left to right: $\tilde{t} = 0.5,\ 1.0,\ 2.0,\ 4.0$.

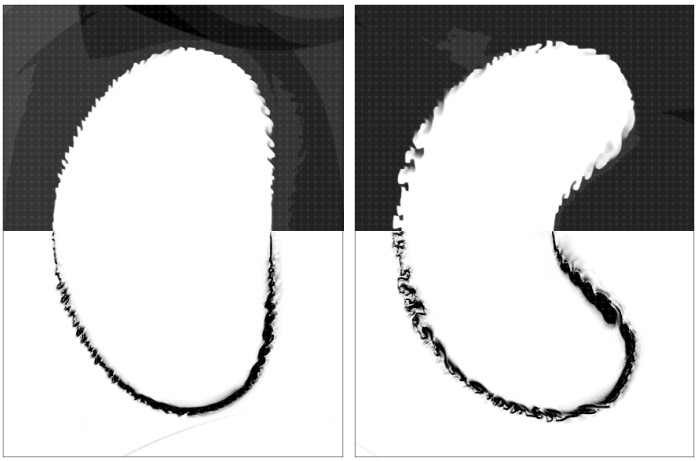

Figure 3.10: Density (upper half) and vorticity (lower half) fields of the air-helium shock-bubble interaction, with interface sharpening, at the grid-resolution of $\Delta x/D = \Delta y/D = 0.00125$. From left to right: $\tilde{t} = 2.0,\ 4.0$.

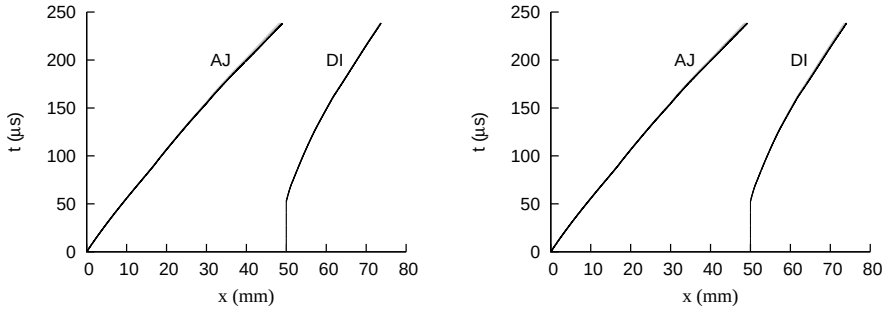


Figure 3.11: Space-time diagram for the characteristic interface points of the air-helium shock-bubble interaction: 'AJ' denotes the air jet head, 'DI' denotes the downstream interface. Lines of light grey color denote $\Delta x/D = \Delta y/D = 0.005$, lines of dark grey color denote $\Delta x/D = \Delta y/D = 0.0025$, lines of black color denote $\Delta x/D = \Delta y/D = 0.00125$. Left: no interface sharpening; right: with interface sharpening. Numerical results are dimensionalized in accordance with [28].

One can note that in the simulation of the same case computed by an interface compression scheme in [88], no instability at the interface is found for a grid with resolution of approximately 225 cells across the bubble initial diameter.

## 2-dimensional shock-contact problem

To demonstrate the improvement by the interface sharpening method for problems with the Mie-Grüneisen EOS, the shock-contact problem of [55, 89, 90, 33] is considered. The problem is the 2-dimensional extension of the corresponding numerical case in 1 dimension and involves a shock wave of Mach number 1.163 propagating from molybdenum to MORB liquid. Mie-Grüneisen EOS are employed for the two materials with coefficients

$$(\rho_0, c_0, s, \Gamma_0) = \begin{cases} (9.961, 4.77, 1.43, 2.56) & \text{for molybdenum} \\ (2.66, 2.1, 1.68, 1.18) & \text{for MORB liquid} \end{cases} . \tag{3.42}$$

A unit square computational domain is defined, and the shock is initialized at $x = 0.35$ traveling towards the positive x-direction. MORB liquid is initialized in the region $[0.4, 0.7] \times [0, 0.5]$, and molybdenum otherwise. The dimensional reference values are $1000kg/m^3$, $1GPa$ and $1m$. The initial condition is

$$(\rho, \mathbf{u}, p) = \begin{cases} (9.964, (0, 0), 0) & \text{pre-shock molybdenum} \\ (11.042, (0.543, 0), 30) & \text{post-shock molybdenum} \end{cases} . \tag{3.43}$$

A wall boundary condition is enforced at the bottom of the domain, an inflow boundary condition at the left of the domain, an outflow boundary condition with a zero gradient at the top and the right of the domain. Numerical results including the volume-fraction contours, Schlieren-type images of density and pressure, with and without the application of the interface sharpening technique, and of two grid resolutions, namely $200 \times 200$ and $400 \times 400$ are shown in Fig. 3.12. To emphasize weak flow features, the non-linear shading function $\phi$ of [69] is used for the Schlieren-type images of density and pressure. For density the function reads

$$\phi = exp\left(-k\frac{|\nabla\rho|}{|\nabla\rho|_{max}}\right) \quad , \tag{3.44}$$

where $k$ is a constant which takes a value of 20 for this test case.

First, by comparing the volume-fraction contours of the results with and without the interface sharpening, one can note that the interface is significantly sharper when

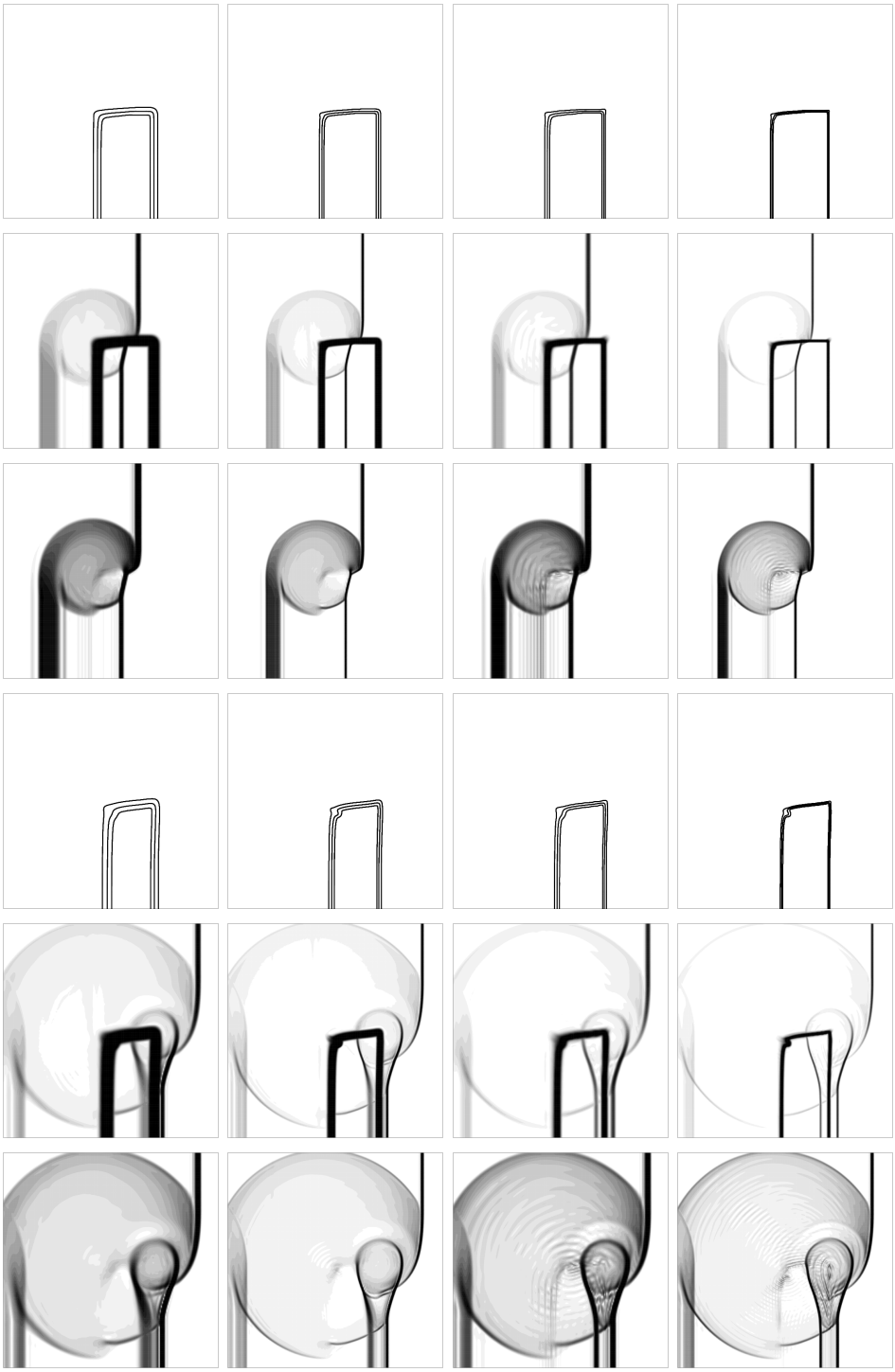

Figure 3.12: Numerical results of the 2D shock-contact problem. The set of top 3 rows: $t = 50\ \mu s$; the set of bottom 3 rows: $t = 100\ \mu s$. From top to bottom in each set: Volume-fraction contours 0.05, 0.5, 0.95; Schlieren-type images of density; Schlieren-type images of pressure. From left to right: $200 \times 200$ (without interface sharpening), $400 \times 400$ (without interface sharpening), $200 \times 200$ (with interface sharpening), $400 \times 400$ (with interface sharpening).

the interface sharpening is applied. The Schlieren-type images of density show that the high-speed jet at $t = 100\ \mu s$ near the tip of the MORB liquid as found in [33], and in [55] computed by an AMR algorithm, is better recovered with the application of interface sharpening. The Schlieren-type images of density and pressure are also in good agreement with [90, 33] at comparable grid resolutions. It should be noted that the results in Fig. 12 in [90] are not computed at the grid resolution $200 \times 200$ as described in the text but at a higher resolution [33, 96].

## 3.5 Concluding remarks

In this chapter, the interface-sharpening technique based on solving an anti-diffusion equation is extended to two-phase compressible flow simulations. A conservative formulation of the Euler equations with the volume-fraction equations of [25] which are capable of simulations with the ideal-gas EOS and the Mie-Grüneisen EOS is employed as the flow governing equations. The HLL Riemann solver and the numerical method for solving the volume-fraction transport equations are described as example for the application and illustration of the interface-sharpening method. The adaptation to other Riemann solvers is straight-forward. The main concept of the interface sharpening is to solve an anti-diffusion equation for the volume-fraction field for counter-acting the numerical diffusion resulting from the underlying VOF discretization scheme. The numerical scheme for solving the anti-diffusion equation ensures the boundedness of the volume fraction and the numerical stability. The merits of the anti-diffusion interface-sharpening method are:

- No interface reconstruction is required to locate the interface.
- No interface-normal calculation and in particular no specific schemes for the interface-normal calculation as in [88] are required.
- The phase masses, momentum and energy are updated consistently in accordance with the sharpened volume-fraction field. The update of the phase masses, momentum and energy are conservative. No hyperbolic function is employed to localize the compression to the interface region for the density equation as required in [88].
- The rate of sharpening across the entire field is variable and derived from the numerical scheme of the underlying VOF discretization schemes. The interface is not compressed to a state determined based merely on the cell size regardless of the compression velocity of the interface sharpening as in [88].

- The interface-sharpening algorithm is modular and applicable to general underlying VOF discretization schemes. The interface-sharpening method can not only be applied to two-phase compressible flow simulations as shown in this work, but also to two-phase incompressible flow simulations based on a VOF discretization, as presented and verified in [93].

- The interface-sharpening algorithm can be formulated for unstructured grids as detailed in [93]. Also, a stopping criterion for the interface-sharpening method is formulated based only on the comparison of gradients of the volume-fraction field. It does not depend on the cell size and thus is not restricted to equidistant Cartesian grids. Thus, the entire interface sharpening method is readily applicable to underlying unstructured grid discretizations.

The anti-diffusion interface-sharpening method is verified by the numerical validation for different EOS and in 1 and 2 dimensions. Simulation results obtained by the interface-sharpening method at different grid resolutions are studied and compared with the reference literature, in particular with the reference high-resolution numerical results based on AMR algorithms. The improvements of the simulation results achieved by the anti-diffusion interface-sharpening method as shown by these test cases are:

- A good agreement of the large-scale interface structures obtained by the interface-sharping method with the results obtained without interface sharpening, experimental results and simulation results from reference literature is observed. The interface is better resolved and finer small-scale interface structures can be recovered with the application of the interface-sharpening method.

- The recovery of finer small-scale interface structures by the interface-sharpening method increases consistently with the grid resolution.

- In compressible flows involving different ideal gases where the Richtmyer-Meshkov instability and the Kelvin-Helmholtz instability are significant for the evolution of the two-phase interface, the method performs particularly well in recovering interfacial instabilities as found for the reference high-resolution numerical results based on AMR algorithms. It is noted that similar details of interface evolution are not recovered in [88, 44] at comparable grid resolutions.

- Numerical cases for the Mie-Grüneisen EOS illustrate the applicability of the interface-sharpening method to different EOS with improved interface representation.

# Chapter 4

# Quantification of initial condition uncertainty in shock-bubble interaction

## 4.1 Introductions

In this chapter, the uncertainties of initial condition in a shock-bubble interaction experiment are modeled and analyzed by simulations. The uncertainties in initial conditions of a widely studied experimental case of the shock-bubble interaction of Haas & Sturtevant [26] are studied and modeled. A non-intrusive stochastic collocation approach is employed to transport the input uncertainties to the output quantities of interest. The evolution of the statistics and of the PDF of the quantities of interest over time is presented and discussed.

This chapter is organized as follows: In preliminaries, the shock-bubble interaction studied, the definition of the uncertainty parameter and the quantities of interest are described. Then, the governing equations and the numerical methods of the flow solver, and the uncertainty quantification methods are presented. The collocated results under each and both uncertainty parameters and the main findings are discussed. Finally, the work is summarized in concluding remarks.

## 4.2 Preliminaries

### Case studied

The experimental case of a cylindrical-helium-bubble in air hit by a shock wave at Mach number of 1.22 of Haas & Sturtevant [26] serves as the basis for the study. The

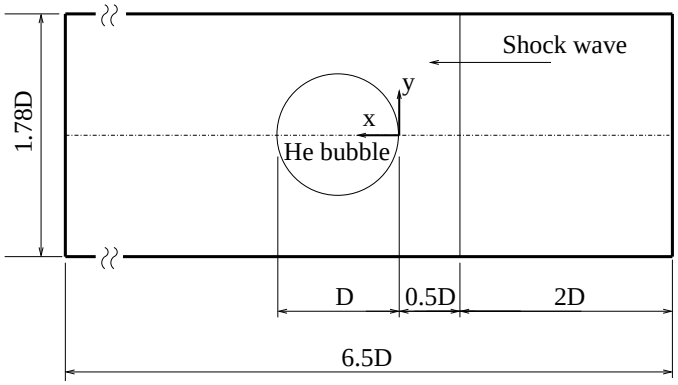


Figure 4.1: Schematic of the computational domain for the shock-bubble interaction simulation. The helium bubble diameter, $D$, is $50mm$.

case can be categorized as a slow-fast interaction (in terms of the ideal-gas sound speed) or a divergent case (helium bubble acts as a divergent acoustic lens in the surrounding air). The experiment was first performed by Haas & Sturtevant to study the refraction and diffraction of shock waves in cylindrical and spherical gas inhomogeneities. It has since been widely studied and simulated, e.g. by Picone & Boris [67] and Quirk & Karni [69] to examine vorticity generation and the dynamics of shock-bubble interaction, and, as a test case, to verify numerical methods [104, 86].

In the experiment, a circular gas-cylinder filled with helium was formed by a microfilm-solution membrane in air. A shock-wave of Mach number of 1.22 was generated in air and hit the helium-cylinder. In simulation the case is treated as a two-dimensional case and the same computational domain as adopted by Shankar et al. [86] is used. Here a different reference system is adopted and the domain is shown in Fig. 4.1.

The flow conditions are determined by the Rankine-Hugoniot jump conditions to be:

- Pre-shock air :$\rho = 1.20kg/m^3$, $\mathbf{u} = (0m/s, 0m/s)$, $p = 101325Pa$, $\gamma_{air} = 1.4$.
- Post-shock air: $\rho = 1.65kg/m^3$, $\mathbf{u} = (114.7m/s, 0m/s)$, $p = 159060Pa$, $\gamma_{air} = 1.4$.
- Helium cylinder: $\rho = 0.166kg/m^3$, $\mathbf{u} = (0m/s, 0m/s)$, $p = 101325Pa$, $\gamma_{helium} = 1.667$.

## Uncertainties in shock-bubble interactions

In shock-bubble interactions, the experimental condition of the bubble is one of the main sources of variation and thus uncertainty. Undesired test gas impurity inside

the bubble and imperfect bubble shape are present in many shock-bubble interaction experiments, whether membrane [26, 49] or no membrane [35, 105] is used for the bubble formation, despite the careful control of experiment conditions. To perform the uncertainty quantification, two uncertainty parameters are defined to represent the variability typically observed in experiments.

The first uncertainty parameter $\xi_1$ describes the amount of initial gas contamination inside the bubble, and a relevant range is derived directly from the error and the methodology for the gas contamination estimation as described in the work of Haas & Sturtevant [26]. The second uncertainty parameter $\xi_2$ is introduced to represent the initial bubble deformation that has been shown to be important in shock-bubble interaction experiments. The present methodology translates these uncertain parameters into random quantities, so that the original problem becomes stochastic.

**Uncertainty of gas contamination**

The test gas impurity is a major source of uncertainty in shock-bubble interaction experiments, and its effect on the interface evolution is reported to be significant in the literature. In the numerical study of Shankar et al. [87], it is demonstrated by means of a series of numerical simulations that in an air-SF6 shock-bubble interaction, the effect of an uncertain amount of acetone in the bubble (added to the bubble gas for experimental image tracing purposes) on the evolution of the RMI and mixing is not negligible. Zhai et al. [124] also studied the effect of the air contamination inside a helium bubble in shock-bubble interactions and they concluded that the air contamination has a significant effect on the bubble evolution.

In the experiment of Haas & Sturtevant [26], the authors reported that the helium-cylinder was contaminated by 28% by mass of air. With reference to [26] (Section 6.1 in the literature), the evaluation of the air-contamination was based on the comparison of the speed of sound estimated from the experiment, $c_{est}$, with the speed of sound of pure media ($1010m/s$ for pure helium). The authors calculated $c_{est}$ by $c_{est} = V_R/M_{est}$, where $V_R$ is the measured velocity of the refracted shock, and $M_{est}$ is the estimated Mach number obtained from the pressure measurement. They obtained $c_{est}$ to be $910m/s$ for the weak-shock case and $833m/s$ for the strong-shock case; the mean value from the experiments, $872m/s$ was used to estimate the air contamination, which yielded the air-contamination of 28% by mass as reported. Further analysis reveals that $c_{est}$ is subject to errors, where the error of $V_R$ is 10 to 20% as given in table 2 in the literature, and the error of $M_{est}$ is not detailed. When the errors are taken into account, $c_{est}$ falls into the range of $[1010m/s, 727m/s]$ (where the maximum is bounded to be $1010m/s$ for pure helium). Based on this, the air-contamination in the helium-

cylinder is selected as an uncertainty parameter, and its range is formulated based on $c_{est}$, which is $[1010m/s, 727m/s]$ centered at $871.5m/s$. This in turn corresponds to an air-contamination by mass of $[0\%, 52.80\%]$ (by volume of $[0\%, 13.40\%]$), centered at 28.45% (by volume 5.21%) corresponding to $c_{est} = 871.5m/s$. Here the uncertainty parameter, $\xi_1$, is denoted by the fraction of air by mass inside the bubble, $f^{air}_{mass} \in [0\%, 52.80\%]$. $\xi_1$ is assumed to be a uniform random variable as no information on its probability distribution is available.

**Uncertainty of bubble deformation**

In most shock-bubble interaction experiments, the bubble is formed and designed to have a perfect circular cross section such as the cylinders and spheres. Correspondingly in simulations which are based on the experiments, a perfect circular shape is used as the initial condition [24, 48]. However, as observed in experiments, when the densities of the gas pair differ to a large extend, the bubble shape can deviate from a perfect circular shape, e.g. approximately becomes a teardrop shape [26, 47, 48, 49]. When the initial shape deviation is not precisely measured, its evolution becomes uncertain. For example, as reported in the experiments of Layes & Le Metayer [48], the variation of the radius of the spherical bubble can reach $2.0 \pm 0.3$ mm. It is also noted that in the numerical simulations of Giordano & Burtschell [24] which simulated the experiments of Layes & Le Metayer [48], the initial bubble shape of a teardrop was represented by a perfect circle in the simulations and no account of the shape deviation was made.

The deformation of a circular bubble to elliptical shape can also be observed in the experiments using a retractable bubble injector with soap films [70]. When the injector is retracted after the bubble formation, the bubble assumes a free fall (or rise) inside the vertical shock tube, but an oscillatory motion initiated by the motion of the retractable bubble injector is also observed, e.g. due to the surface tension effect of the soap membrane film. While the bubble is falling (or rising) with an oscillatory motion inside the shock tube, the shock wave is then triggered and it is thus plausible when the shock approaches the bubble, its cross section is not perfectly circular but assumes an elliptical shape.

On the other hand, an elliptical bubble hit by a shock was studied numerically and experimentally, where based on numerical simulations, Ray et al. [73] purposed an interface circulation deposition model for elliptical bubbles, and experimentally Zou et al. [126] studied the interface evolution of elliptic gas cylinder with different axis ratio in shock-bubble interactions.

As a generic approach to describe the bubble deformation, in the present work the bubble is assumed to be elliptical with its axis along the streamwise direction varying,

and define the uncertainty parameter, $\xi_2$, as the eccentricity, $e = \sqrt{1-(b/a)^2}$, where $b$ and $a$ are respectively the semi-minor axis and the semi-major axis of the ellipse. By the original definition of eccentricity, $e \in [0, 1]$. Here, it is defined alternatively

$$e = \begin{cases} \sqrt{1-(b/a)^2} & \text{if } a \text{ is along x-axis} \\ -\sqrt{1-(b/a)^2} & \text{if } b \text{ is along x-axis} \end{cases}, \tag{4.1}$$

and we choose $e \in [-0.5, +0.5]$ with the middle value at $e = 0$, i.e. a circle. It is assumed that $\xi_2$ to be a random variable with a uniform probability distribution.

Although it is possible that the air contamination leads to considerable difference in bubble weight and, therefore, to bubble deformation, here it is assumed that the two effects are not correlated. In the following, $\xi_1$ and $\xi_2$ are assumed to be independent random variables.

## Definition of quantities of interest

The interface evolution measured by the characteristic interface points and primary vorticity production are considered as the quantities of interest to characterize the simulation results.

### Interface evolution and characteristic interface points

To characterize the simulation results of shock-bubble interactions, the first quantity of interest is the evolution of the bubble interface. For code verification purposes, the interface evolution is an important quantity of interest for the comparison between different numerical results as well as the comparison with experimental results [86]. The characteristic interface points, namely the upstream location $q^u$, the downstream location $q^d$ and the jet $q^j$ of the interface [26], are used to charteristize the interface evolution. The volume fraction contour of 0.5 is used to define the interface location for measuring the characteristic interface points.

The jet is of particular interest in certain studies such as the interaction of shock waves with gas cavities in fluids. Its formation and evolution are key parameters to characterize the cavity collapse [9]. On the other hand, the interface evolution is also studied extensively by experiments [47, 49], where different geometries, e.g. bubble length, vortex area, etc. of the shocked bubble under different gas pairs were recorded for characterizing the shock-bubble interactions.

As shown below in section 4.4, the maximum variance is located at the vortex position which cannot be measured by the characteristic interface points. Therefore,

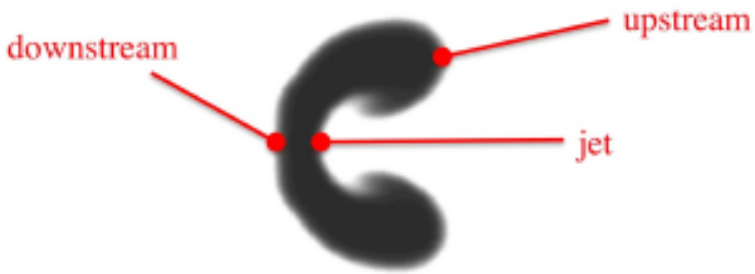


Figure 4.2: Helium bubble after the shock impact. Three characteristic points are identified at the bubble surface [97].

to examine the interface evolution on the whole flow field, the density field is used to illustrate the interface evolution in addition to the characteristic interface points.

### Primary vorticity production

In a shock-bubble interaction, the vorticity generated in the system is strongly associated with the baroclinic generation of vorticity due to the misalignment of $\nabla\rho$ and $\nabla p$. The baroclinic vorticity production is the major mechanism of vorticity generation in the early phase of interaction (vorticity deposition phase). In the subsequent time known as the vorticity evolution phase, mechanisms including the secondary baroclinic effects, the vortex roll-up, the development of vortex cores, Kevin-Helmholtz instability and Richtmyer-Meshkov instability come into play. The large-scale motion breaks into smaller scales and eventually into turbulence. In this work, the focus is on the uncertainty in the vorticity deposition phase - the period in which the shock sweeps through the bubble (i.e. the shock travels one bubble-diameter distance). The total vorticity, $q^{\Gamma}$, which is the integration of the magnitude of vorticity over the entire control volume, is employed as the second quantity of interest:

$$q^{\Gamma} = \int |\omega| \, dxdy \quad , \tag{4.2}$$

where $\omega$ is the vorticity defined as $\nabla \times \mathbf{u}$, and $\mathbf{u}$ is the velocity.

This should be noted that the 3-dimensional turbulent mixing effects in shock-bubble interactions cannot be simulated by a 2-dimensional setting as in the present work. In this regard, as shown in [119] where the shock-bubble interaction of a $SF_6$ cylinder in air is studied, the evolution of the circulation computed by 2-dimensional and 3-dimensional simulations are comparable. Thus in this work, the 2-dimensional simulations are deemed to be sufficient to compute the correct evolution of vorticity

for a shock-cylindrical-bubble interaction as the quantity of interest.

The above uncertainty parameters and quantities of interest are generic to most experiments of shock-bubble interaction. It should be added that other uncertainties still exist in shock-bubble interaction experiments. As the case studied in the work is concerned, they include the uncertain gas diffusion across the interface, the varying shock strength; and the uncertainties due to the effect of the existence and the rupture of the membrane for forming the helium cylinder, the effect of the intruding support structure and the 3-dimensional nature in 2-dimensional simulations are difficult to quantify. In particular, the varying shock strength can be a significant source of uncertainty in shock-bubble interaction experiments. Nevertheless, as no systematic estimate of the incident shock strength variation is available in [26], it is a reasonable assumption that the authors has made their effort to present their results without the significant influence from the uncertain incident shock strength, and correspondingly the incident shock strength is not modeled as an uncertainty in this work.

## 4.3 Methods

### Governing equations, numerical method and setup for shock-bubble interaction simulation

To simulate the shock-bubble interaction, the basic two-phase compressible flow governing equation as presented in chapter 3 is adopted. For the simulation under the uncertainty parameters $\xi_1$ and $\xi_2$, the flow field is assumed to be symmetrical about the center axis and thus only the top half domain is computed. The zero-gradient boundary condition is imposed on the left and right boundaries, and the symmetry-plane boundary condition is imposed on the top and bottom boundaries. The grid resolution employed is $\Delta x/D = \Delta y/D = 0.01$.

It should be noted that interface sharpening methods as detailed in the chapter 3 and more involved numerical methods [104, 86, 96] can be adopted for the recovery of the small-scale structures of the interface in late times. However for the numerical solution of the compressible Euler equations as an initial-value problem, no pointwise convergence is expected [81] and thus it is difficult to obtain converged results for the quantities of interest such as the total vorticity at late times. As the quantities of interest in this work are the bubble large-scale structure and the total vorticity at the vorticity-deposition phase, the basic numerical method without the anti-diffusion interface sharpening is found to be sufficient for the purpose and is employed.

In order to verify the simulation code, and to demonstrate that the quantities of

interest computed are accurate, a grid-convergence study is conducted and the results are compared with other established numerical results for the base deterministic case simulated by reference literature. This base deterministic case corresponds to $f_{mass}^{air} = 28.45\%$, $e = 0$, $f_{in}^{air} = 0$. In Fig. 4.3, the characteristic interface points converge as the grid refines (which is also shown in chapter 3), and by comparing the results with that of the experiment [26] and by other numerical methods [86], it can be seen that the evolution of the characteristic interface points are in good agreement with the reference literature. $q^{\Gamma}$ converges upon the refinement of the grid for $t = 0 - 150\mu s$. The evolution of $q^{\Gamma}$ also agrees with the observations of the study by Quirk & Karni [69] where for $t = 0 - 60\mu s$, the shock front traverses one bubble-radius distance, i.e. it sweeps through the windward side of the bubble, and $q^{\Gamma}$ bottoms out at around $t = 60\mu s$, which is the moment when the refracted wave emerges from the bubble.

## Uncertainty quantification method

The objective of the uncertainty quantification is to evaluate the effect of the two uncertainty parameters $\xi_1$ and $\xi_2$ on the quantities of interest ($q^k$ with $k = u, d, j, \Gamma$).

The polynomial chaos approach is adopted to approximate the relationship between the output and the input $q^k = q^k(\xi_1, \xi_2)$ by a (truncated) polynomial basis:

$$q^k(\xi_1, \xi_2) = \sum_{\ell=0}^{\infty} q_\ell^k \psi_\ell(\xi_1, \xi_2) \approx \sum_{\ell=0}^{P} q_\ell^k \psi_\ell(\xi_1, \xi_2) \quad , \tag{4.3}$$

where $q_\ell^k$ are coefficients to be determined and $\psi_\ell$ are orthogonal polynomials such that

$$\langle \psi_i \psi_j \rangle = \int_{\Xi} \psi_i(\xi_1, \xi_2) \psi_j(\xi_1, \xi_2) d\xi_1 d\xi_2 = \delta_{ij} C_{ij} \quad . \tag{4.4}$$

$\Xi$ is the domain spanned by the parameters $\xi_1$ and $\xi_2$ while $C_{ij}$ is a normalization constant [103] and $\delta_{ij}$ is the Kronecker delta. The coefficients $q_\ell^k$ can be obtained by projection:

$$q_\ell^k = \frac{\langle q^k(\xi_1, \xi_2), \psi_\ell(\xi_1, \xi_2) \rangle}{\langle \psi_\ell \psi_\ell \rangle} \quad . \tag{4.5}$$

The evaluation of the coefficients $q_\ell^k$ requires the numerical evaluation of the integrals in Eq. 4.5, where the details refer to [97] and are described in Appendix B.

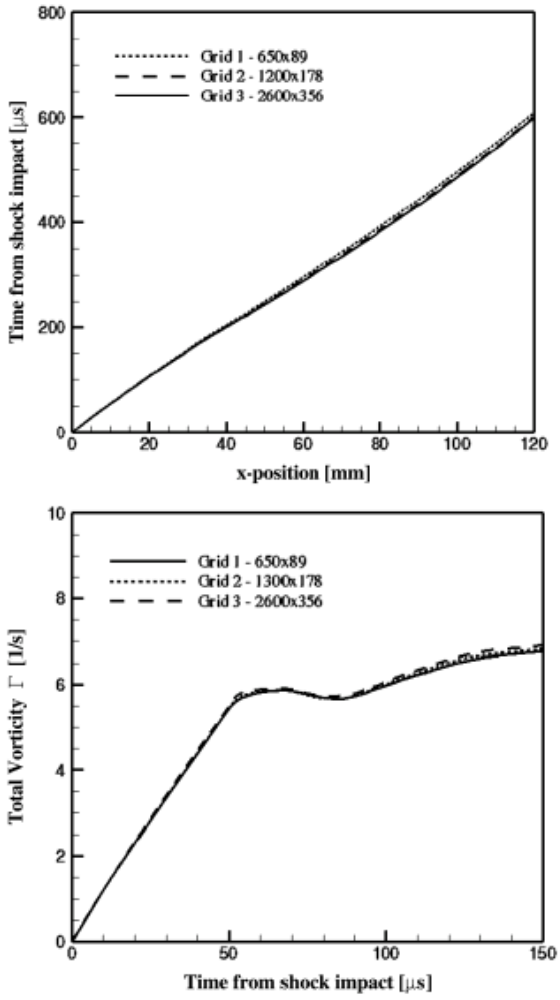


Figure 4.3: Top: space-time diagrams for the upstream position; bottom: total vorticity against time. Solid line, $\Delta x/D = 0.0025$, dashed line, $\Delta x/D = 0.005$; dotted line, $\Delta x/D = 0.01$.

## 4.4 Results

The uncertainties in the initial conditions have a direct impact on the time evolution of the helium bubble and the process of vorticity generation at the interface. Before the shock impact, the variability due to the uncertainties in the initial conditions is confined to the bubble density and shape, which can be observed in the first panel of Fig. 4.4. Once the shock hits the bubble, the uncertainty is transported into the entire domain. The density field of the shock-bubble interaction at different time instants is reported in the subsequent panels in Fig. 4.4, which shows the resulting variability of the interface location. The shock speed in the bubble is directly affected by the density variability and as a result large variance in the shock location is also observed. As for the vorticity generation at the interface, it is also directly affected by both the uncertainty in air contamination, $\xi_1$, and the variability in the initial shape of the bubble, $\xi_2$. The respective effect of the 2 uncertainties on the quantities of interest is described in the following sections.

### Time evolution of the statistics of the quantities of interest

The analysis of the statistics of the quantities of interest is presented in this section. First, the effect of the input uncertainties on the evolution of the interface in terms of the three characteristic interface points, $q^u, q^d, q^j$, is studied. The evolution of the mean location does not show significant difference from the nominal evolution as reported in Fig. 4.3. On the other hand, the time evolution of the variability as reported in Fig. 4.5 reveals the impacts due to the presence of the uncertainties. The upstream tip of the bubble is first located at the origin of the domain to keep the time of the shock hitting fixed. The uncertainty in the air contamination, $\xi_1$, strongly affects its location as the shock hits the bubble. In the initial phase, the variability of the upstream location grows linearly in response to the variability in the bubble density. At $t \approx 100\mu s$, the jet is formed and the variance of the upstream location decreases for a small time interval, before it starts to increase again at $t \approx 200\mu s$. This is a consequence of the overall reduction in speed of the upstream point once the jet is detached. The jet location variability on the other hand continues to increase strongly in an non-linear fashion until it impacts the downstream side of the bubble (at $t \approx 500\mu s$). The large variability in the relative position of the downstream and the jet locations is also evident from the last panel in Fig. 4.4. The uncertainty in the downstream location remains largely constant as it is mainly resulted from the initial uncertainty in the bubble shape. The variability increases considerably when the jet impacts the leeward side of the bubble at $t \approx 500\mu s$.

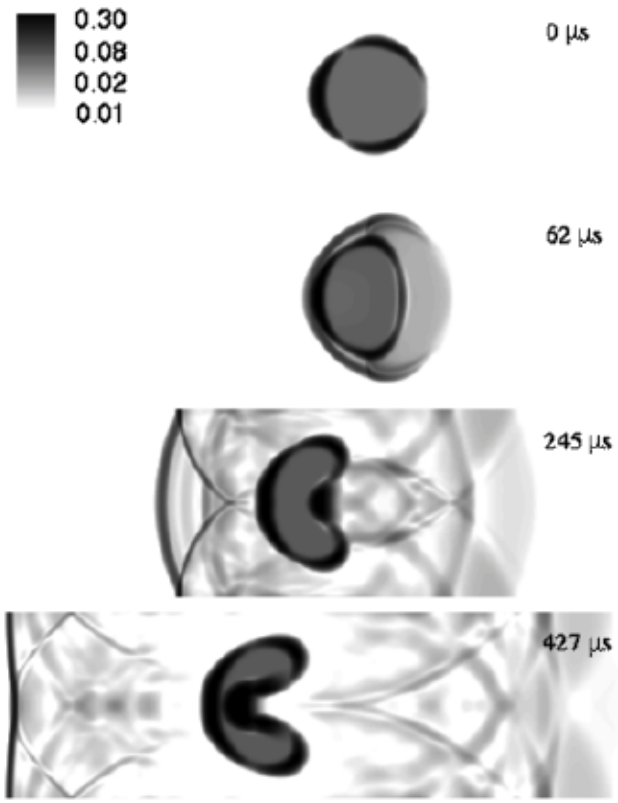


Figure 4.4: Time evolution of the standard deviation of the density field $[kg/m^3]$. The top figure corresponds to the initial conditions before the shock impact. The uncertainty is confined to the bubble (air-contamination) and connected to its shape (circular vs. elliptic). After the shock impact the uncertainty is transported into the entire domain.

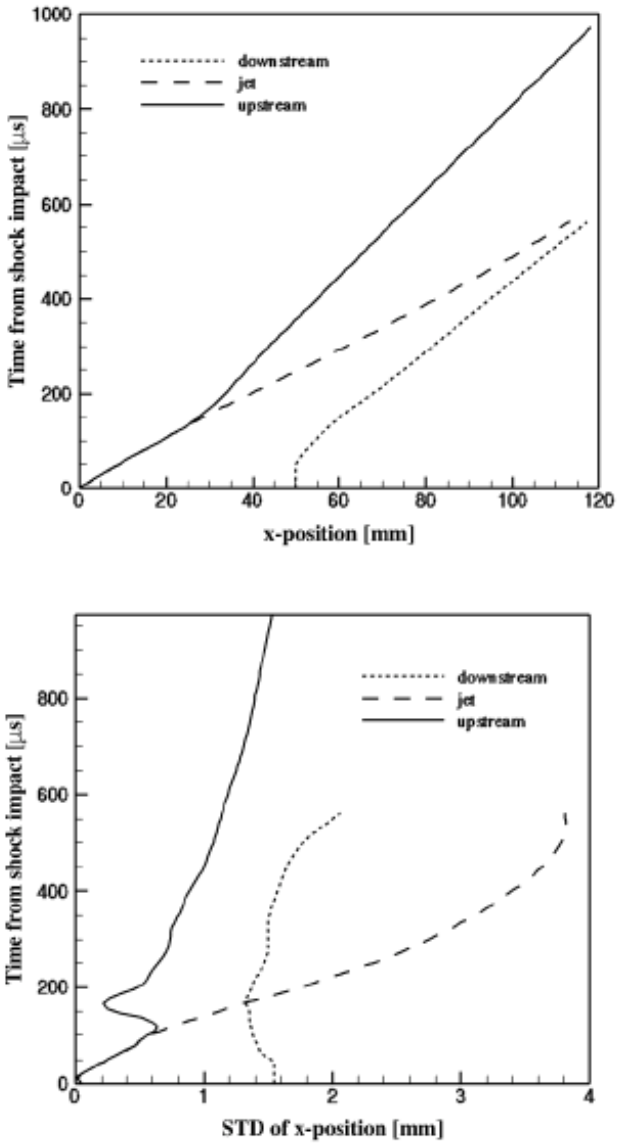


Figure 4.5: Time evolution of the mean (top) and standard deviation (bottom) for 3 characteristic points at the bubble interface (see Fig. 4.2).

The evolution of the vorticity, $q^{\Gamma}$, is affected by input uncertainties mainly due to variability of the baroclinic vorticity production at the interface, the misalignment of the pressure gradient and the density gradient during the passage of the shock across the bubble. The impact of the air contamination and bubble shape uncertainty on the total vorticity generated during the interaction is reported in Fig. 4.6 in terms of its mean and standard deviation. As for the characteristic interface points defined in Fig. 4.2, the mean of total vorticity does not show any substantial difference with respect to the nominal case. The evolution of the standard deviation on the other hand shows the effect of the presence of the uncertainties. In the initial phase at $t \approx 100\mu s$, the standard deviation grows linearly and then remains fairly constant up to $t \approx 400\mu s$ when the jet moves close to the downstream side of the bubble. During the jet impingement, the variance increases considerably. To investigate the effect of the input uncertainties independently and discern the uncertainty which has a dominant impact on the vorticity, the standard deviation due to the combination of both input uncertainties is reported in Fig. 4.6 (bottom) together with the effect of only the air contamination or the bubble shape.

It is clear that in the first phase of the interaction (up to $t \approx 100\mu s$) the two uncertainties have competing effects as illustrated in Fig. 4.7, the overall effect of air contamination is dominant. Initially the impact of air-contamination is of primary importance; the change in bubble density directly affects the amount of vorticity *deposited* on the interface. In this phase, the effect of the bubble shape uncertainty is limited to a change in curvature that is negligible for the cases considered here. However, at $t \approx 50\mu s$ the variability induced by the bubble shape starts to increase because the downstream edge of the bubble starts to move, and at the same time the effect of the air-contamination is reduced because the shock propagates toward the leeward side of the bubble in regions of reduced misalignment between $\nabla\rho$ and $\nabla p$.

As mentioned earlier, a strong sensitivity to grid resolution and numerical methods is expected after the initial vorticity deposition phase. The results reported here show that for a given discretization scheme and a fixed mesh, the initial conditions might induce a similar increased sensitivity. On the other hand, the results of uncertainty quantification rely on the numerical quadrature for computing the coefficient of the polynomial chaos expansion of the quantity of interest (Eq. 4.3) as described above. The statistical convergence of the output uncertainty is described in [97] and summarized in Appendix C.

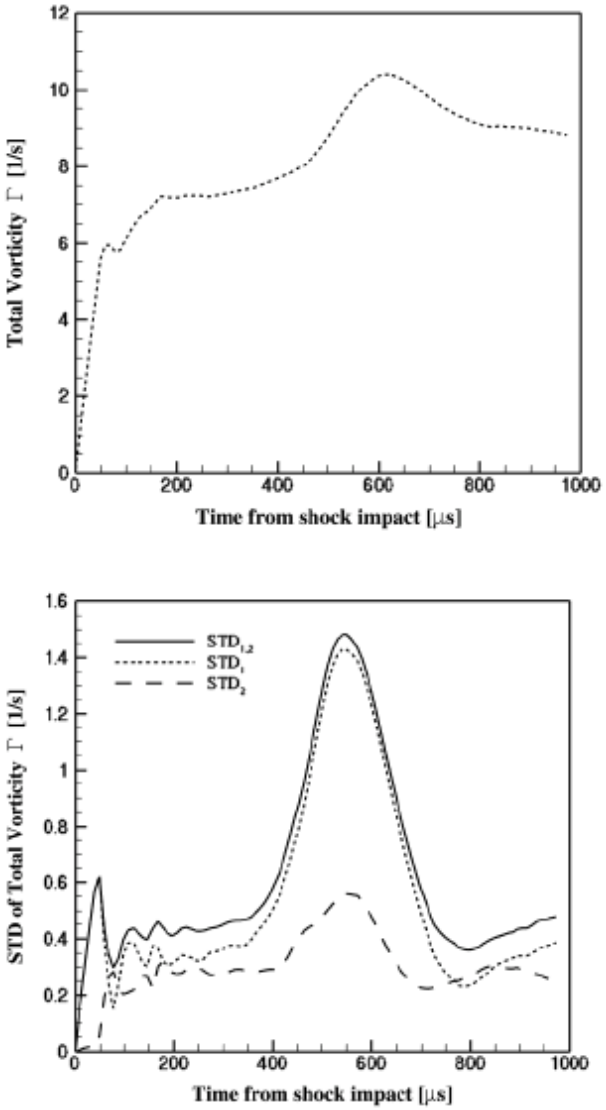


Figure 4.6: Time evolution of the mean (top) and standard deviation (bottom) of the total vorticity in the domain. $STD_{1,2}$ refers to the variability due to the combination of both input uncertainties while $STD_1$ and $STD_2$ correspond to the effect of the air contamination and bubble shape respectively.

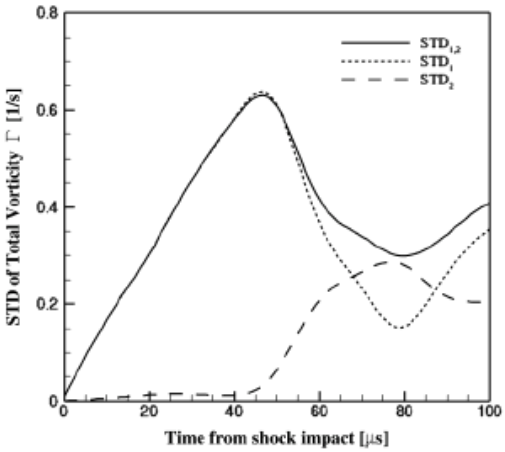


Figure 4.7: Time evolution of the standard deviation of the total vorticity in the domain.$STD_{1,2}$ refers to the variability due to the combination of both input uncertainties while $STD_1$ and $STD_2$ correspond to the effect of the air contamination and bubble shape respectively.

## Time evolution of the probability density functions of the quantities of interest

The probability density functions (PDF) of the quantities of interest are studied and presented in this section. In Fig. 4.8, the PDF of the downstream point is shown when considering both the uncertainties or one at the time, where a dramatic change of the shape of the PDF can be observed. In the initial phase, the PDF resembles a uniform distribution which is consistent with the assumed input uncertainty. At later stages, it has a very distinct peak which indicates that with a high probability, the evolution is equivalent to the one resulting in the absence of uncertainties. The width (support) of the distribution suggests that there is a large remaining uncertainty in the evolution even at later stages, which is also indicated by the evolution of the standard deviation. The individual effect of input uncertainty is shown in last two panels in Fig. 4.8. where the PDF of the location of the downstream point induced by the air contamination and the bubble initial shape are reported. The effect of air contamination uncertainty $\xi_1$ is almost negligible after $t \approx 300\mu s$, while the effect of the uncertainty in shape $\xi_2$ remains almost unchanged as time progresses.

The PDF of the total vorticity is reported in Fig. 4.9 and it confirms the dynamics illustrated in Fig. 4.6. The largest variability observed at $t \approx 500\mu s$ results in a broad distribution. The effect of the air contamination and the bubble shape is comparable at $t \approx 100\mu s$ and $t \approx 800\mu s$ while in the intermediate phases the first one dominates.

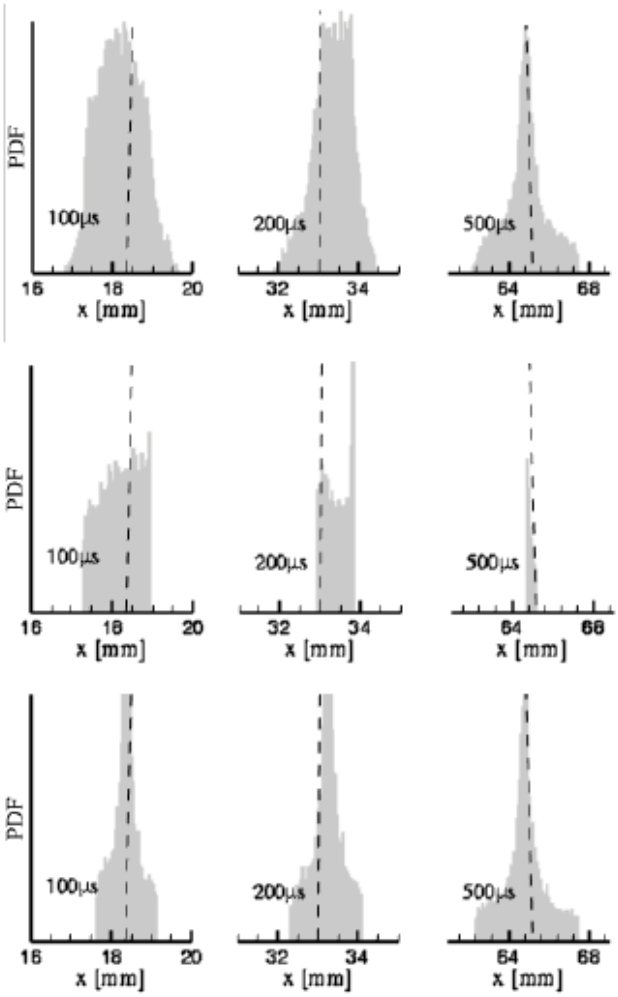


Figure 4.8: Time evolution of the probability density function of the characteristic downstream point (Fig. 4.2). Top: uncertainty in both the air contamination and bubble shape; middle: uncertainty in air contamination alone; bottom: uncertainty in bubble shape alone. The dashed line corresponds to the location of the downstream point in the nominal conditions.

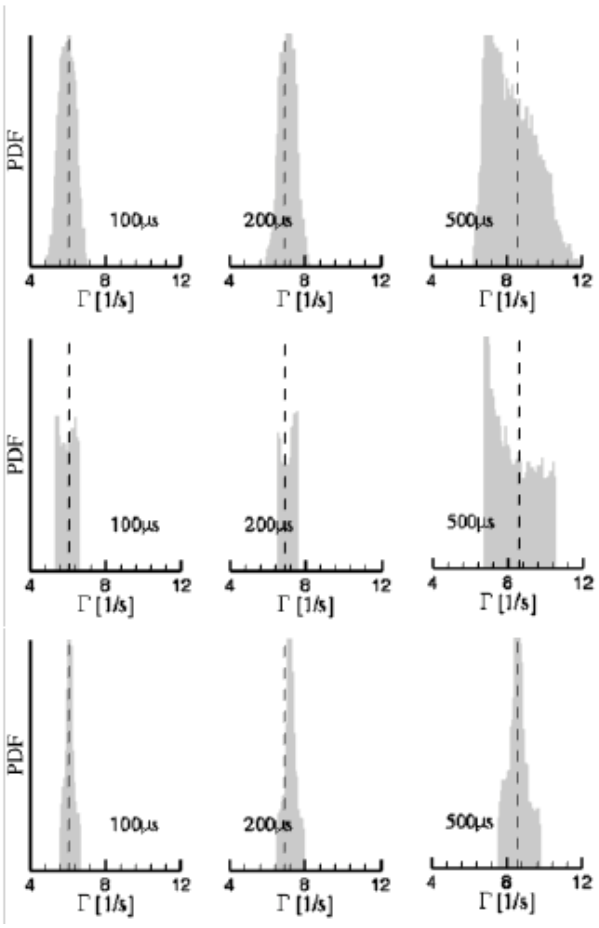


Figure 4.9: Time evolution of the probability density function of the total vorticity. Top: uncertainty in the both air contamination and bubble shape; middle: uncertainty in air contamination alone; bottom: uncertainty in bubble shape alone. The dashed line corresponds to the total vorticity in the nominal conditions.

## 4.5 Concluding remarks

The interaction of a shock with a helium bubble in air is investigated using numerical simulations. The effect of uncertainties in the initial conditions on the dynamics of the bubble interface and the vorticity generation process is studied in this work. The air contamination in the helium bubble and the non-circular initial shapes are considered as the two dominant sources of uncertainty and relevant ranges of probable scenarios are defined according to experimental observations. A compressible gas model and a discretization method based on the volume-of-fluid approach is employed, and the uncertainties are characterized probabilistically using a polynomial chaos technique.

The results illustrate that the initial uncertainty strongly affects the evolution of the interface, especially the location of the jet formed inside the bubble. A large variability is also observed in terms of vorticity generation, where initially the air contamination uncertainty dominates the variability of the quantities of interest, but in the late time as the shock moves across the bubble, the effect of the shape uncertainty becomes comparable.

# Chapter 5

# Conclusions

In this work, the shock-bubble interaction under uncertainties have been investigated by CFD simulations. The primary goals were to develop novel numerical methods, suitable for two-phase flow simulations and shock-bubble interactions; and to investigate and analyze the uncertainties in physical shock-bubble interactions by means of simulations.

Correspondingly, a novel numerical method for maintaining the interface sharpness in two-phase flow simulations based on VOF methods was developed and verified for both incompressible and compressible regimes. Essential techniques for this interface-sharpening method were developed including a specified discretization scheme and stopping criterion for solving the anti-diffusion equation, and a consistent and conservative update of all flow variables in compressible-flow formulations. Numerical results for incompressible regimes showed that the method is competitive even with level-set approaches when similar discretizations are used for the level-set transport as for the volume-fraction transport, so that both methods imply comparable computational cost. For compressible regimes, the simulations of shock-bubble interaction shows that the interface sharpness can be maintained and more small-scale structures recovered in a consistent and reliable manner as the grid resolution increases. Important interface roll-up phenomena due to the Richtmyer-Meshkov instability and the Kelvin-Helmholtz instability in shock-bubble interactions can be reliably simulated, where the numerical results are comparable to reference high grid-resolution numerical solutions based on adaptive-mesh-refinement algorithms. In summary, the proposed interface-sharpening technique based on VOF methods offer a general numerical algorithm for two-phase flow simulations where the conservation of the flow variables is exact and the interface sharpness is maintained in the course of simulation. The implementation of the interface-sharpening technique to other VOF underlying discretizations and industrial unstructured-grid CFD codes are straight-forward which

makes the technique suitable for engineering applications.

A widely studied experimental case of helium-air shock-bubble interaction was then studied by simulations. The initial condition of the amount of gas contamination inside the bubble and of the deformation of the initial bubble shape were selected as the uncertainty parameters, where the interface evolution and the total vorticity were considered as the quantities of interest. The propagation of the input uncertainty to the output quantities of interest by means of the stochastic collocation method showed that the jet formed inside the bubble and the baroclinic vorticity generation during the vorticity deposition phase are largely dependent on the bubble gas content as well as the bubble shape.

As potential extensions of the current work, the interface-sharpening technique can be applied to other two-phase simulations, such as compressible flow based on other equations of state, with a necessary adaption of the formulation. Besides, the uncertainty quantification of other shock-bubble interaction experiments, as well as other experiments of fluid dynamics phenomena such as RMI, where the initial condition (e.g. initial interface perturbations) is subject to uncertainty and believed to have a strong influence on the flow evolution, can also be conducted based on the methodology described in this work.

# Appendix A

# Stability criterion for discrete anti-diffusion equation

The relevant stability criterion for the discrete anti-diffusion equation is the *local extremum principle* [65, 50, 11], which in its strong form requires

$$\frac{1}{2}\min\left(\Delta_{i+1/2}\alpha^n, -\Delta_{i-1/2}\alpha^n, 0\right) \leq \alpha_{i+1}^{n+1} - \alpha_i^n \leq \frac{1}{2}\max\left(\Delta_{i+1/2}\alpha^n, -\Delta_{i-1/2}\alpha^n, 0\right) \quad . \tag{A.1}$$

This principle is satisfied by (2.11) under the condition

$$\Delta\tau = \frac{\Delta x^2}{2D} \quad . \tag{A.2}$$

For the proof, it is assumed that

$$\mathrm{sgn}\Delta_{i+1/2}\alpha^n = \mathrm{sgn}\Delta_{i-1/2}\alpha^n > 0 \quad .$$

Eq. (2.11) can be rewritten as

$$\alpha_{i+1/2}^n = \alpha_i^n - \frac{\Delta\tau D}{\Delta x^2}\left(C_{i+1/2}\Delta_{i+1/2}\alpha^n - C_{i-1/2}\Delta_{i-1/2}\alpha^n\right) \quad ,$$

where

$$C_{i+1/2} = \mathrm{sgn}\Delta_{i+1/2}\alpha^n mmod_{i+1/2}$$

and

$$mmod_{i+1/2} = \mathrm{minmod}\left(\frac{\Delta_{i+3/2}\alpha^n}{|\Delta_{i+1/2}\alpha^n|}, \mathrm{sgn}\Delta_{i+1/2}\alpha^n, \frac{\Delta_{i-1/2}\alpha^n}{|\Delta_{i+1/2}\alpha^n|}\right) \quad .$$

Given the above assumption, the above time-step constraint, and the properties of the *minmod* function, it can be deduced that

$$0 \leq \left(C_{i+1/2}\Delta_{i+1/2}\alpha^n - C_{i-1/2}\Delta_{i-1/2}\alpha^n\right) \leq \Delta_{i-1/2}\alpha^n$$

provided that $\Delta_{i+1/2}\alpha^n \geq \Delta_{i-1/2}\alpha^n$. For the converse case $\Delta_{i+1/2}\alpha^n \leq \Delta_{i-1/2}\alpha^n$ it can be obtained that

$$0 \leq \left(C_{i+1/2}\Delta_{i+1/2}\alpha^n - C_{i-1/2}\Delta_{i-1/2}\alpha^n\right) \leq \Delta_{i+1/2}\alpha^n \quad .$$

Thus, the local extremum principle is satisfied with respect to the upper bound.

With respect to the lower bound the principle is satisfied for the case

$$\mathrm{sgn}\Delta_{i+1/2}\alpha^n = \mathrm{sgn}\Delta_{i-1/2}\alpha^n < 0$$

following the same procedure as above. For

$$\mathrm{sgn}\Delta_{i+1/2}\alpha^n \neq \mathrm{sgn}\Delta_{i-1/2}\alpha^n \quad ,$$

it can be obtained that $C_{i+1/2} = C_{i-1/2} = 0$, and the principle is satisfied as well.

# Appendix B

# Evaluation of coefficients of truncated polynomial basis

The evaluation of the coefficients $q_\ell^k$ requires the numerical evaluation of the integrals in Eq. 4.5. The Clenshaw-Curtis (CC) quadrature [7, 19] is used in this work, with the basis functions $\psi_\ell(\xi_1, \xi_2)$ defined as tensor product of one-dimensional Chebychev polynomials. The CC approach requires the evaluation of the integrand in Eq. 4.5 at a finite number $N_a \times N_a$ of locations within the domain (abscissas) spanned by the variables $\xi_1$ and $\xi_2$. This requires the evaluation of $q^k(\xi_1, \xi_2)$ at selected values of $\xi_1$ and $\xi_2$ and thus the solution of the original bubble/shock interaction problem with different initial conditions. In the following, the collocated results are obtained by using $17 \times 17$ abscissas (in total 289 computations).

The order $P$ in Eq. 4.3 is chosen as $P = (N_a - 1)/2$ by recognizing that the CC quadrature with $N_a$ abscissas integrates exactly polynomials of order $N_a - 1$. By increasing $N_a$, the evaluation of the integrals (4.5) is more accurate and the precision of the polynomial chaos approximants 4.3 is increased. As shown in Appendix C, the choice of $N_a = 17$ and $P = 8$ leads to converged results.

Once the polynomial chaos coefficients $q_\ell^k$ are computed, the statistics of the quantity of interest $q_k$ can be studied in details. The expected value (mean), $\mathbb{E}[q^k]$, and the variance, $\mathrm{Var}[q^k]$, can simply be obtained by

$$\mathbb{E}[q^k] = \int_\Xi q^k d\xi_1 d\xi_2 \approx \sum_{\ell=0}^{P} q_\ell^k \left( \int_\Xi \psi_\ell d\xi_1 d\xi_2 \right) = q_0^k \quad , \tag{B.1}$$

$$\mathbb{E}[(q^k)^2] = \int (q^k)^2 d\xi_1 d\xi_2 \approx \sum_{\ell=0}^{P} \sum_{\jmath=0}^{P} q_\ell^k q_\jmath^k \left( \int_\Xi \psi_\ell \psi_\jmath d\xi_1 d\xi_2 \right)$$

$$= \sum_{\ell=0}^{P} C_{\ell,\ell} \left(q_\ell^k\right)^2 \quad , \tag{B.2}$$

$$\mathrm{Var}[q^k] = \mathbb{E}[(q^k)^2] - (E[q^k])^2 = \sum_{\ell=1}^{P} (q_\ell^k)^2 = \left(\mathrm{STD}[q^k]\right)^2 \quad . \tag{B.3}$$

In addition to the statistical moments of the quantities of interest, one can also evaluate the PDF by performing Monte Carlo sampling directly on Eq. 4.3. One important tool in understanding the propagation of uncertainties in a physical problem is the determination of the relative importance (and effect) of each of the input uncertainties. This can be accomplished by evaluating two additional polynomial chaos expansions for $q^k(\xi_1, \mathbb{E}[\xi_2])$ and $q^k(\mathbb{E}[\xi_1], \xi_2)$ directly form the general expression in Eq. 4.3 without requiring additional simulations.

# Appendix C

# Statistical convergence of quantities of interest

The evaluations of the integrals (4.5) is based on the use of $17 \times 17$ abscissas (289 computations). In order to verify the accuracy of the CC methods and the overall accuracy of the polynomial chaos expression (Eq. 4.3), the collocated results using $9 \times 9$ and $5 \times 5$ abscissas is also computed observing that the CC quadrature is nested [19]. The results are reported in Fig. C.1 and it can be observed that the difference between $9 \times 9$ and $17 \times 17$ remains very small for the entire time interval considered. It is worth mentioning that the computations of the standard deviation (and the variance) requires the computations of all the polynomial chaos coefficients (up to order $P$) and therefore is more sensitive to errors in the quadrature accuracy of polynomial chaos truncation order.

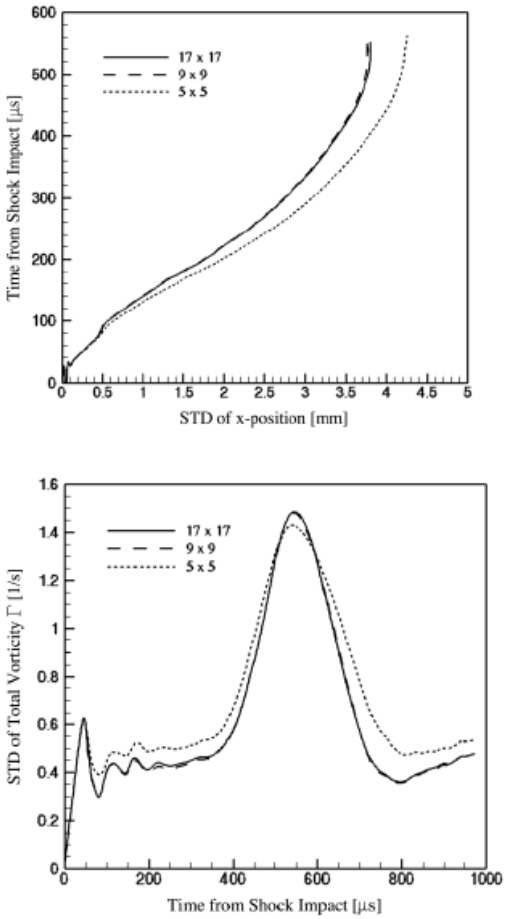


Figure C.1: Convergence of the standard deviation of the jet location (top) and the total vorticity (bottom) using different quadrature order in computing the integrals in Eq. 4.5.

# References

[1] R. Abgrall, How to prevent pressure oscillations in multicomponent flow calculations: a quasi conservative approach, J. Comput. Phys. 125 (1996) 150-160.

[2] A. Bagabir, D. Drikakis, Numerical experiments using high-resolution schemes for unsteady, inviscid, compressible flows, Comput. Methods App. Mech. Engrg. 193 (2004) 4675-4705.

[3] B. J. Balakumar, G. C. Orlicz, C. D. Tomkins, K. P. Prestridge, Simultaneous particle-image velocimetry-planar laser-induced fluorescence measurements of Richtmyer-Meshkov instability growth in a gas curtain with and without reshock, Phys. Fluids 20 (2008).

[4] D. S. Balsara, C.-W. Shu, Monotonicity preserving weighted essentially non-oscillatory schemes with increasingly high order of accuracy, J. Comput. Phys. 160 (2000) 405-452.

[5] J. W. Banks, D. W. Schwendeman, A. K. Kapila, W. D. Henshaw, A high-resolution Godunov method for compressible multi-material flow on overlapping grids, J. Comput. Phys. 223 (2007) 262-297.

[6] D. Bhaga, M. E. Weber, Bubbles in viscous-liquids: shapes, wakes and velocities, J. Fluid Mech. 105 (1981) 61-85.

[7] I. Babuska, F. Nobile, R. Tempone, A stochastic collocation method for elliptic partial differential equations with random input data, SIAM J. Numer. Anal. 45 (3) (2007) 1005-1034.

[8] J. P. Boris, D. L. Book, Flux-corrected transport. I. SHASTA, a fluid transport algorithm that works, J. Comput. Phys. 11 (1973) 38-69.

[9] N. K. Bourne, J. E. Field, Shock-induced collapse of single cavities in liquids, J. Fluid Mech. 244 (1992) 225.

[10] J. U. Brackbill, D. B. Kothe, C. Zemach, A continuum method for modeling surface tension, J. Comput. Phys. 100 (1992) 335-354.

[11] M. Breuß, T. Brox, T. Sonar, J. Weickert, Stabilized nonlinear inverse diffusion for approximating hyperbolic PDEs, Scale Space and PDE Methods in Computer Vision, Proceedings 3459 (2005) 536-547.

[12] M. Breuß, M. Welk, Staircasing in semidiscrete stabilized inverse linear diffusion algorithms, J. Comput. Appl. Math. 206 (2007) 520-533.

[13] M. Brouillette, The Richtmyer-Meshkov instability, Annu. Rev. Fluid Mech. 34 (2002) 445-68.

[14] D. A. Cassidy, J. R. Edwards, M. Tian, An investigation of interface-sharpening schemes for multi-phase mixture flows, J. Comput. Phys. 228 (2009) 5628-5649.

[15] T. Chantrasmi, A. Doostan, G. Iaccarino, Pade-Legendre approximants for uncertainty analysis with discontinuous response surfaces, J. Comput. Phys. 228 (2009) 7159.

[16] C. H. Chang, M. S. Liou, A robust and accurate approach to computing compressible multiphase flow: Stratified flow model and AUSM$^+$-up scheme, J. Comput. Phys. 228 (2009) 4012-4037.

[17] Q. -Y. Chen, D. Gottlieb, J. S. Hesthaven, Uncertainty analysis for the steady-state flows in a dual throat nozzle, J. Comput. Phys. 204 (2005) 378-398.

[18] A. Chertock, S. Karni, A. Kurganov, Interface tracking method for compressible multifluid, Math. Model. Numer. Anal. 42 (2008) 991-1019.

[19] C. W. Clenshaw, A. R. Curtis, A method for numerical integration on an automatic computer, Numerische Mathematik 2 (1960) 197.

[20] G. Compère, E. Marchandise, J. Remacle, Transient adaptivity applied to two-phase incompressible flows, J. Comput. Phys. 227 (2008) 1923-1942.

[21] G. Dimonte, C. E. Frerking, M. Schneider, B. Remington, Richtmyer-Meshkov instability with strong radiatively driven shocks, Phys. Plasmas 3 (2) (1996) 614-630.

[22] R. P. Fedkiw, T. Aslam, B. Merriman, S. Osher, A non-oscillatory Eulerian approach to interfaces in multimaterial flows (the ghost fluid method), J. Comput. Phys. 152 (1999) 457-494.

[23] G. Gilboa, N. Sochen, Y. Y. Zeevi, Forward-and-backward diffusion processes for adaptive image enhancement and denoising, IEEE Trans. Image Proc. 11 (2002) 689-703.

[24] J. Giordano, Y. Burtschell, Richtmyer-Meshkov instability induced by shock-bubble interaction: Numerical and analytical studies with experimental validation, Phys. Fluids 18 (2006) 036102.

[25] J. A. Greenough, V. Beckner, R. B. Pember, W. Y. Crutchfield, J. B. Bell, P. Colella, An adaptive multifluid interface-capturing method for compressible flow in complex geometries, AIAA Paper (1995) 95-1718.

[26] J. F. Haas, B. Sturtevant, Interaction of weak shock waves with cylindrical and spherical gas inhomogeneities, J. Fluid Mech. 181 (1987) 41-76.

[27] Harten, Ami, High resolution schemes for hyperbolic conservation laws, J. Comput. Phys. 49 (1983) 357-393.

[28] B. Hejazialhosseini, D. Rossinelli, M. Bergdorf, P. Koumoutsakos, High order finite volume methods on wavelet-adapted grids with local time-stepping on multi-core architectures for the simulation of shock-bubble interactions, J. Comput. Phys. 229 (2010) 8364-8383.

[29] M. Hemmat, A. Borhan, Buoyancy-driven motion of drops and bubbles in a periodically constricted capillary, Chem. Eng. Comm. 150 (1996) 363-384.

[30] C. W. Hirt, B. D. Nichols, Volume of fluid (VOF) method for the dynamics of free boundaries, J. Comput. Phys. 39 (1981) 201-225.

[31] J. G. Hnat, J. D. Buckmaster, Spherical cap bubbles and skirt formation, Phys. Fluids 19 (2) (1976) 182-194.

[32] X. Y. Hu, B. C. Khoo, An interface interaction method for compressible multi-fluids, J. Comput. Phys. 198 (2004) 35-64.

[33] X. Y. Hu, N. A. Adams, G. Iaccarino, On the HLLC Riemann solver for interface interaction in compressible multi-fluid flow, J. Comput. Phys. 228 (2009) 6572-6589.

[34] R. I. Issa, Solution of the implicitly discretised fluid flow equations by operator-splitting, J. Comput. Phys. 62 (1985) 40-65.

[35] J. W. Jacobs, Shock-induced mixing of a light-gas cylinder, J. Fluid Mech. 234 (1992) 629.

[36] J. W. Jacobs, The dynamics of shock accelerated light and heavy gas cylinders, Phys. Fluids A 5 (9) (1993) 2239-2247.

[37] H. Jasak, H. G. Weller, A. D. Gosman, High resolution NVD differencing scheme for arbitrarily unstructured meshes, Int. J. Num. Meth. Fluids 31 (1999) 431-449.

[38] S. Jiang, G. Ni, A second-order $\gamma$-model BGK scheme for multimaterial compressible flows, Appl. Numer. Math. 57 (2007) 597-608.

[39] E. Johnsen, T. Colonius, Implementation of WENO schemes in compressible multicomponent flow problems, J. Comput. Phys. 219 (2006) 715-732.

[40] M. A. Jones, J. W. Jacobs, A membraneless experiment for the study of Richtmyer-Meshkov instability of a shock-accelerated gas interface, Phys. Fluids 9 (10) (1993) 3078-3085.

[41] A. K. Kapila, R. Menikoff, J. B. Bdzil, S. F. Son, D. S. Stewart, Two-phase modeling of deflagration-to-detonation transition in granular materials: reduced equations, Phys. Fluids 13 (10) (2001) 3002-3024.

[42] G. E. Karniadakis, J. Glimm, Uncertainty quantification in simulation science, J. Comput. Phys. 217 (2006) 1-4.

[43] S. Kawai, H. Terashima, A high-resolution scheme for compressible multicomponent flows with shock waves, Int. J. Num. Meth. Fluids (2010) doi: 10.1002/fld.2306.

[44] S. Kokh, F. Lagoutiere, An anti-diffusive numerical scheme for the simulation of interfaces between compressible fluids by means of a five-equation model, J. Comput. Phys. 229 (2010) 2773-2809.

[45] J. J. Kreeft, B. Koren, A new formulation of Kapila's five-equation model for compressible two-fluid flow, and its numerical treatment, J. Comput. Phys. 229 (2010) 6220-6242.

[46] B. Lafaurie, C. Nardone, R. Scardovelli, S. Zaleski, G. Zanetti, Modelling merging and fragmentation in multiphase flows with SURFER, J. Comput. Phys. 113 (1994) 134-147.

[47] G. Layes, G. Jourdan, O. Le Metayer, Experimental investigation of the shock wave interaction with a spherical gas inhomogeneity, Phys. Fluids 17 (2005) 028103.

[48] G. Layes, O. Le Metayer, Quantitative numerical and experimental studies of the shock accelerated heterogeneous bubbles motion, Phys. Fluids 19 (2007) 042105.

[49] G. Layes, G. Jourdan, L. Houas, Experimental study on a plane shock wave accelerating a gas bubble, Phys. Fluids 21 (2009) 074102.

[50] P. G. Lefloch and J.-G. Liu, Jasak, Generalized monotone schemes, discrete paths of extrema, and discrete entropy conditions, Math. Comput. 68 (1999) 1025-1055.

[51] R. J. Leveque, Finite Volume Methods for Hyperbolic Problems, Cambridge University Press, 2002.

[52] E. Marchandise, P. Geuzaine, N. Chevaugeon, J. Remacle, A stabilized finite element method using a discontinuous level set approach for the computation of bubble dynamics, J. Comput. Phys. 225 (2007) 949-974.

[53] L. G. Margolin, Introduction to "An Arbitrary Lagrangian-Eulerian Computing Method for All Flow Speeds", J. Comput. Phys. 135 (1997) 198-202.

[54] A. Marquina, P. Mulet, A flux-split algorithm applied to conservative models multicomponent compressible flows, J. Comput. Phys. 185 (2003) 120-138.

[55] G. H. Miller, E. G. Puckett, A high-order Godunov method for multiple condensed phases, J. Comput. Phys. 128 (1996) 134-164.

[56] M. Muradoglu, A. D. Kayaalp, An auxiliary grid method for computations of multiphase flows in complex geometries, J. Comput. Phys. 214 (2006) 858-877.

[57] H. N. Najm, Uncertainty quantification and polynomial Chaos techniques in computational fluid dynamics, Annu. Rev. Fluid Mech. 41 (2009) 35-52.

[58] G. Ni, W. Sun, A $\gamma$-DGBGK scheme for compressible multi-fluids, Int. J. Num. Meth. Fluids (2010) doi: 10.1002/fld.2283.

[59] J. H. J. Niederhaus, J. A. Greenough, J. G. Oakley, D. Ranjan, M. H. Anderson, R. Bonazza, A computational parameter study for the three-dimensional shock-bubble interaction, J. Fluid Mech. 594 (2008) 85-124.

[60] W. Noh, P. Woodward, Lecture Notes in Physics, Springer Berlin, 1976.

[61] R. R. Nourgaliev, T. N. Dinh, T. G. Theofanous, Adaptive characteristics-based matching for compressible multifluid dynamics, J. Comput. Phys. 213 (2006) 500-529.

[62] E. Olsson, G. Kreiss, A conservative level set method for two phase flow, J. Comput. Phys. 210 (2005) 225-246.

[63] E. Olsson, G. Kreiss, S. Zahedi, A conservative level set method for two phase flow II, J. Comput. Phys. 225 (2007) 785-807.

[64] OpenFOAM, http://www.openfoam.com

[65] S. Osher, L. I. Rudin, Feature-oriented image enhancement using shock filters, SIAM J. Numer. Anal. 27 (1990) 919-940.

[66] S. Osher, R. P. Fedkiw, Level set methods: An overview and some recent results, J. Comput. Phys. 169 (2001) 463-502.

[67] J. M. Picone, J. P. Boris, Vorticity generation by shock propagation through bubbles in a gas, J. Fluid Mech. 189 (1988) 23-51.

[68] I. Pollak, A. S. Willsky, H. Krim, Image segmentation and edge enhancement with stabilized inverse diffusion equations, IEEE Trans. Image Proc. 9 (2000) 256-266.

[69] J. J. Quirk, S. Karni, On the dynamics of a shock-bubble interaction, J. Fluid Mech. 318 (1996) 129-163.

[70] D. Ranjan, Experimental investigation of the shock-induced distortion of a spherical gas inhomogeneity, Ph.D. thesis, University of Wisconsin-Madison (2008).

[71] D. Ranjan, J. H. J. Niederhaus, J. G. Oakley, M. H. Anderson, R. Bonazza, J. A. Greenough, Shock-bubble interactions: Features of divergent shock-refraction geometry observed in experiments and simulations, Phys. Fluids 20 (2008) 036101.

[72] D. Ranjan, J. Oakley, R. Bonazza, Shock-bubble interactions, Annu. Rev. Fluid Mech. 43 (2011) 117-140.

[73] J. Ray, R. Samtaney, N. J. Zabusky, Shock interactions with heavy gaseous elliptic cylinders: Two leeward-side shock competition modes and a heuristic model for interfacial circulation deposition at early times, Phys. Fluids 12 (3) (2000) 707.

[74] W. J. Rider, An adaptive Riemann solver using a two-shock approximation, Comput. Fluids 28 (1999) 741-777.

[75] W. J. Rider, D. B. Kothe, Reconstructing volume tracking, J. Comput. Phys. 141 (1998) 112-152.

[76] W. J. Rider, L. G. Margolin, Simple modifications of monotonicity-preserving limiter, J. Comput. Phys. 174 (2001) 473-488.

[77] P. J. Roache, Quantification of uncertainty in computational fluid dynamics, Annu. Rev. Fluid Mech. 29 (1997) 123-160.

[78] H. Rusche, Computational fluid dynamics of dispersed two-phase flows at high phase fractions, Ph.D. thesis, Imperial College of Science, Technology & Medicine (2002).

[79] S. K. Sambasivan, H. S. UdadyKumar, Sharp interface simulations with local mesh refinement for multi-material dynamics in strongly shocked flows, Comput. Fluids 39 (2010) 1456-1479.

[80] R. Samtaney, N. J. Zabusky, Circulation deposition on shock-accelerated planar and curved density-stratified interfaces: models and scaling laws, J. Fluid Mech. 269 (1994) 45-78.

[81] R. Samtaney, D. I. Pullin, On initial-value and self-similar solutions of the compressible Euler equations, Phys. Fluids 8 (10) (1996) 2650-2655.

[82] R. Samtaney, J. Ray, N. J. Zabusky, Baroclinic circulation generation on shock accelerated slow/fast gas interfaces, Phys. Fluids 10 (5) (1998) 1217-1230.

[83] R. Saurel, F. Petitpas, R. A. Berry, Simple and efficient relaxation methods for interfaces separating compressible fluids, cavitating flows and shocks in multiphase mixtures, J. Comput. Phys. 228 (2009) 1678-1712.

[84] R. Scardovelli, S. Zaleski, Direct numerical simulation of free-surface and interfacial flow, Annu. Rev. Fluid Mech. 31 (1999) 567-603.

[85] J. A. Sethian, P. Smereka, Level set methods for fluid interfaces, Annu. Rev. Fluid Mech. 35 (2003) 341-372.

[86] S. K. Shankar, S. Kawai, S. K. Lele, Numerical simulations of multicomponent shock accelerated flows and mixing using localized artificial diffusivity method, AIAA Paper 2010-352 (2010).

[87] S. K. Shankar, S. Kawai, S. K. Lele, Two-dimensional viscous flow simulation of a shock accelerated heavy gas cylinder, Phys. Fluids 23 (2) (2011).

[88] R. K. Shukla, C. Pantano, J. B. Freund, An interface capturing method for the simulation of multi-phase compressible flows, J. Comput. Phys. 229 (2010) 7411-7439.

[89] K. M. Shyue, A fluid-mixture type algorithm for compressible multicomponent flow with Mie-Grüneisen equation of state, J. Comput. Phys. 171 (2001) 678-707.

[90] K. M. Shyue, A wave-propagation based volume tracking method for compressible multicomponent flow in two space dimensions, J. Comput. Phys. 215 (2006) 219-244.

[91] K. K. So, X. Y. Hu, N. A. Adams, Anti-diffusion correction for sharp interface of two-phase incompressible flow, Proceedings of Open source CFD International Conference, Barcelona, Spain (2009).

[92] K. K. So, T. Chantrasmi, X. Y. Hu, J. A. S. Witteveen, C. Stemmer, G. Iaccarino, N. A. Adams, Uncertainty analysis for shock-bubble interaction, Proceedings of the 2010 Summer Program, Center for Turbulence Research, Stanford University, USA (2010).

[93] K. K. So, X. Y. Hu, N. A. Adams, Anti-diffusion method for interface steepening two-phase incompressible flow, J. Comput. Phys. 230 (2011) 5155-5177.

[94] K. K. So, T. Chantrasmi, X. Y. Hu, C. Stemmer, G. Iaccarino, N. A. Adams, Uncertainty quantification for shock-bubble interaction, Proceedings of the Sonderforschungsbereich Transregio 40 (SFB-TR 40) Summer Program 2011, Technische Universität München (TUM), Germany (2011).

[95] K. K. So, X. Y. Hu, N. A. Adams, Anti-diffusion interface sharpening technique for two-phase compressible flow simulations, 28th International Symposium on Shock Wave, Part 1 (2012) 57-62.

[96] K. K. So, X. Y. Hu, N. A. Adams, Anti-diffusion interface sharpening technique for two-phase compressible flow simulations, J. Comput. Phys. 231 (2012) 4304-4323.

[97] K. K. So, T. Chantrasmi, X. Y. Hu, C. Stemmer, G. Iaccarino, N. A. Adams, Quantification of initial condition uncertainty in shock-bubble interactions, under preparation for publication.

[98] K. K. So, X. Y. Hu, N. A. Adams, Anti-diffusion interface sharpening technique for two-phase compressible flow simulations, International Conference on Numerical Methods in Multiphase Flows, The Pennsylvania State University, USA (2012).

[99] Y. Sun, C. Beckermann, Sharp interface tracking using the phase-field equation, J. Comput. Phys. 220 (2007) 626-653.

[100] M. Sussman, P. Smereka, S. Osher, A level set approach for computing solutions to incompressible two-phase flow, J. Comput. Phys. 114 (1994) 146-159.

[101] M. Sussman, E. G. Puckett, A coupled level set and volume-of-fluid method for computing 3D and axisymmetric incompressible two-phase flows, J. Comput. Phys. 162 (2000) 301-337.

[102] M. Sussman, K. M. Smith, M. Y. Hussaini, M. Ohta, R. Zhi-Wei, A sharp interface method for incompressible two-phase flows, J. Comput. Phys. 221 (2007) 469-505.

[103] Szego, Gabor, Orthogonal Polynomials, Colloquium Publications XXIII, American Mathematical Society.

[104] H. Terashima, G. Tryggvason, A front-tracking/ghost-fluid method for fluid interfaces in compressible flows, J. Comput. Phys. 228 (2009) 4012-4037.

[105] C. Tomkins, S. Kumar, G. Orlicz, K. Prestridge, An experimental investigation of mixing mechanisms in shock-accelerated flow, An experimental investigation of mixing mechanisms in shock-accelerated flow, J. Fluid Mech. 611 (2008) 131-150.

[106] E. Toro, Riemann Solvers and Numerical Methods for Fluid Dynamics, Springer, 1997.

[107] D. J. Torres, J. U. Brackbill, The point-set method: Front-tracking without connectivity, J. Comput. Phys. 165 (2000) 620-644.

[108] G. Tryggvason, B. Bunner, A. Esmaeeli, D. Juric, N. Al-Rawahi, W. Tauber, J. Han, S. Nas, Y. J. Jan, A front-tracking method for the computations of multiphase flow, J. Comput. Phys. 169 (2001) 708-759.

[109] O. Ubbink, Numerical prediction of two fluid systems with sharp interfaces, Ph.D. thesis, Imperial College of Science, Technology & Medicine (1997).

[110] O. Ubbink, R. I. Issa, A method for capturing sharp fluid interfaces on arbitrary meshes, J. Comput. Phys. 153 (1999) 26-50.

[111] S. O. Unverdi, G. Tryggvason, A front-tracking method for viscous, incompressible, multi-fluid flows, J. Comput. Phys. 100 (1992) 25-37.

[112] B. van Leer, Towards the ultimate conservative difference scheme. II. Monotonicity and conservation combined in a second-order scheme, J. Comput. Phys. 14 (1974) 361-370.

[113] F. Xiao, A. Ikebata, An efficient method for capturing free boundaries in multi-fluid simulations, Int. J. Num. Meth. Fluids 42 (2003) 187-210.

[114] F. Xiao, Y. Honma, T. Kono, A simple algebraic interface capturing scheme using hyperbolic tangent function, Int. J. Num. Meth. Fluids 48 (2005) 1023-1040.

[115] F. Xiao, A. Ikebata, T. Hasegawa, Numerical simulations of free-interface fluids by a multi-integrated moment method, Comput. Struct. 83 (2005) 409-423.

[116] D. Xiu, J. S. Hesthaven, High-order collocation methods for differential equations with random inputs, SIAM J. Sci. Comput. 27 (3) (2005) 1118-1139.

[117] Z. Xu, C.-W. Shu, Anti-diffusive flux corrections for high order finite difference WENO schemes, J. Comput. Phys. 205 (2005) 458-485.

[118] C. Wang, C. W. Shu, An interface treating technique for compressible multi-medium flow with Runge-Kutta discontinuous Galerkin method, J. Comput. Phys. 229 (2010) 8823-8843.

[119] V. G. Weirs, T. Dupont, T. Plewa, Three-dimensional effects in shock-cylinder interactions, Phys. Fluids 20 (4) (2008).

[120] J. Yang, T. Kubota, E. E. Zukoski, Applications of shock-induced mixing to supersonic combustion, AIAA Paper 31 (5) (1993) 854.

[121] J. Yang, T. Kubota, E. E. Zukoski, A model for characterization of a vortex pair formed by shock passage over a light-gas inhomogeneity, J. Fluid Mech. 258 (1994) 217-244.

[122] N. J. Zabusky, Vortex paradigm for accelerated inhomogeneous flows: visiometrics for the Rayleigh-Taylor and Richtmyer-Meshkov environments, Annu. Rev. Fluid Mech. 31 (1999) 495.

[123] S. T. Zalesak, Fully multidimensional flux-corrected transport algorithms for fluids, J. Comput. Phys. 31 (1979) 335-362.

[124] Zhigang Zhai, Ting Si, Xisheng Luo, Jiming Yang, On the evolution of spherical gas interfaces accelerated by a planar shock wave, Phys. Fluids 23 (2011) 084104.

[125] S. Zhang, N. J. Zabusky, G. Peng, S. Gupta, Shock gaseous cylinder interactions: Dynamical validated initial conditions provide excellent agreement between experiments and numerical simulations to late-intermediate time, Phys. Fluids 16 (2004) 1203.

[126] Liyong Zou, Cangli Liu, Duewang Tan, Wenbin Huang, Xisheng Luo, On interaction of shock wave with elliptic gas cylinder, J. Vis. 13 (2010) 347.